Heft 305   Ishani Banerjee

Stochastic Model Comparison and Refinement Strategies for Gas Migration in the Subsurface

Stochastic Model Comparison and Refinement Strategies for Gas Migration in the Subsurface

Von der Fakultät Bau- und Umweltingenieurwissenschaften
der Universität Stuttgart zur Erlangung der Würde eines
Doktor-Ingenieurs (Dr.-Ing.) genehmigte Abhandlung

vorgelegt von

Ishani Banerjee

aus Kalkutta, Indien

Hauptberichter:	Prof. Dr.-Ing. Wolfgang Nowak
Mitberichter:	Dr. rer. nat. Anneli Guthke
	Prof. Dr. Kevin Mumford

Tag der mündlichen Prüfung: 29. November 2023

Institut für Wasser- und Umweltsystemmodellierung
der Universität Stuttgart
2023

Heft 305

Stochastic Model Comparison and Refinement Strategies for Gas Migration in the Subsurface

von
Dr.-Ing.
Ishani Banerjee

D93   Stochastic Model Comparison and Refinement Strategies for Gas Migration in the Subsurface

Acknowledgements

Contents

List of Figures

List of Tables

Nomenclature

Selected Acronyms

2D	2-Dimensional
BF	Bayes Factors
BME	Bayesian Model Evidence
BMS	Bayesian Model Selection
IP	Invasion Percolation
Macro-IP	Macroscopic Invasion Percolation
MC	Monte Carlo
MFP	Method of Forced Probabilities

Symbols

(X_c, Z_c)	Centroid position of gas cluster in 2D space	[m,m]
$(\sigma_{xx}{}^2, \sigma_{zz}{}^2)$	Variance of gas cluster in 2D space	[m^2,m^2]
α	P_e- to $-P_t$ ratio	[-]
$\boldsymbol{\omega}_k$	Random events from parameter space U_k	
$\boldsymbol{\theta}_k$	Uncertain parameters from parameter space U_k	

g	Acceleration due to gravity	[m/s^2]
λ	Pore-size distribution index	[-]
$\mathbf{u}_k$	Random parameter vector from U_k	
$\mathbf{y_0}$	Observation data	
$\mathcal{M}$	Ratio of dynamic viscosities of displacing fluid to that of displaced fluid	[-]
$\mathcal{R}$	Random number from the standard uniform distribution on the interval [0,1], generated using MATLAB *combRecursive* generator	
$\mathcal{U}$	Random number from the standard uniform distribution on the interval [0,1], generated using MATLAB *Threefry* generator	
$\mathscr{M}_{sp}$	Spatial moments of $(s+p)^{th}$ order	[m^{s+p}]
μ_g	Dynamic viscosity of gas phase	[Pa $-$ s]
ϕ	Porosity of sand	[-]
ρ	Density	[kg/m^3]
σ	Gaussian kernel width (standard deviation) for convolution	
Bo	Bond number	[-]
c	Cell selection weighting factor for Model 4	
Ca	Capillary number	[-]
J	Jaccard coefficient	[-]
J_d	Diffused Jaccard coefficient	[-]
M_k	k^{th} model out of N_m competing models	

n_{blocks}	number of blocks invaded per model loop counter	
n_{ev}	Number of atomic events	
n_{MC}	Ensemble size	
nb	Number of blocks invaded per step of Model 3	
$p(.\,|\,.)$	Conditional probability density function of a random variable	
P_c	Capillary pressure	[cm of H_2O]
P_d	Macroscopic displacement pressure	[cm of H_2O]
P_e	Local entry pressure of a block	[cm of H_2O]
P_t	Terminal pressure	[cm of H_2O]
P_w	Hydrostatic pressure	[cm of H_2O]
Q_{crit}	Critical flow rate	[m^3/s]
Q_{exp}	Volume of gas in experiment	[m^3/s]
r_c	Characteristic radius of gas channels	[m]
S_e	effective wetting phase saturation	[-]
S_g	Gas saturation	[-]
T_e	Invasion threshold	[cm of H_2O]
T_t	Terminal threshold	[cm of H_2O]
$T_{e,asc}$	List of invasion threshold values in ascending order	[cm of H_2O]
$T_{e,cum}$	Cumulative sum of $T_{e,asc}$ values	[cm of H_2O]
t_{end}	Time of completion of experiment	[s]

t_{exp}	Time step in between the capture of two successive experimental images	[s]
U_k	Parameter space of model-k	
V_{block}	Volume of discretized model block	[m³]
V_{exp}	Volume of gas in experiment	[m³]
V_{model}	Volume of gas in model	[m³]
z	Height from top of the experimental acrylic cell	[m]

Abstract

Gas migration in the subsurface, a multiphase flow in a porous-medium system, is a problem of environmental concern and is also relevant for subsurface gas storage in the context of the energy transition. It is essential to know and understand the flow paths of these gases in the subsurface for efficient monitoring, remediation or storage operations. On the one hand, laboratory gas-injection experiments help gain insights into the involved processes of these systems. On the other hand, numerical models help test the mechanisms observed and inferred from the experiments and then make useful predictions for real-world engineering applications.

Both continuum and stochastic modelling techniques are used to simulate multiphase flow in porous media. In this thesis, I use a stochastic discrete growth model: the macroscopic Invasion Percolation (IP) model. IP models have the advantages of simplicity and computational inexpensiveness over complex continuum models. Local pore-scale changes dominantly affect the flow processes of gas flow in water-saturated porous media. IP models are especially favourable for these multi-scale systems because using continuum models to simulate them can be extremely computationally difficult.

Despite offering a computationally inexpensive way to simulate multiphase flow in porous media, only very few studies have compared their IP model results to actual laboratory experimental image data. One reason might be the fact that IP models lack a notion of experimental time but only have an integer counter for simulation steps that imply a time order. The few existing experiments-to-model comparison studies have used perceptual similarity or spatial moments as comparison measures. On the one hand, perceptual comparison between the model and experimental images is tedious and non-objective. On the other hand, comparing spatial moments of the model and experimental images can lead to misleading results because of the loss of information from the data. In this thesis, an objective and quantitative comparison method is

developed and tested that overcomes the limitations of these traditional approaches. The first step involves volume-based time-matching between real-time experimental data and IP-model outputs. This is followed by using the *(Diffused) Jaccard coefficient* to evaluate the quality of the fit. The fit between the images from the models and experiments can be checked across various scales by varying the extent of blurring in the images.

Numerical model predictions for sparsely known systems (like the gas flow systems) suffer from high conceptual uncertainties. In literature, numerous versions of IP models, differing in their underlying hypotheses, have been used for simulating gas flow in porous media. Besides, the gas-injection experiments belong to continuous, transitional, or discontinuous gas flow regimes, depending on the gas flow rate and the porous medium's nature. Literature suggests that IP models are well suited for the discontinuous gas flow regime; other flow regimes have not been explored. Using the abovementioned method, in this thesis, four macroscopic IP model versions are compared against data from nine gas-injection experiments in transitional and continuous gas flow regimes. This model inter-comparison helps assess the potential of these models in these unexplored regimes and identify the sources of model conceptual uncertainties.

Alternatively, with a focus on parameter uncertainty, Bayesian Model Selection is a standard statistical procedure for systematically and objectively comparing different model hypotheses by computing the Bayesian Model Evidence (BME) against test data. BME is the likelihood of a model producing the observed data, given the prior distribution of its parameters. Computing BME can be challenging: exact analytical solutions require strong assumptions; mathematical approximations (information criteria) are often strongly biased; assumption-free numerical methods (like Monte Carlo) are computationally impossible for large data sets. In this thesis, a BME-computation method is developed to use BME as a ranking criterion for such infeasible scenarios: The *Method of Forced Probabilities* for extensive data sets and Markov-Chain models. In this method, the direction of evaluation is swapped: instead of comparing thousands of model runs on random model realizations with the observed data, the model is forced to reproduce the data in each time step, and the individual probabilities of the model following these exact transitions are recorded. This is a fast, accurate and exact method for calculating BME for IP models which exhibit the Markov chain property and for complete "atomic" data.

The analysis results obtained using the methods and tools developed in this thesis help identify the strengths and weaknesses of the investigated IP model concepts. This further aids model development and refinement efforts for predicting gas migration in the subsurface. Also, the gained insights foster improved experimental methods. These tools and methods are not limited to gas flow systems in porous media but can be extended to any system involving raster outputs.

Zusammenfassung

Ausbreitung von Gasen im Untergrund, eine Mehrphasenströmung in einem porösen Medium, ist relevant sowohl bei Umweltproblemen und für energierelevante Gasspeicherung in Untergrund. Für eine effiziente Überwachung, Sanierung oder Speicherung ist es wichtig, die Ausbereitungspfade dieser Gase im Untergrund zu kennen und zu verstehen. Einerseits helfen Laborexperimente zur Gasinjektion dabei, Einblicke in die beteiligten Prozesse in diesen Systemen zu gewinnen. Andererseits helfen numerische Modelle dabei, die beobachteten und aus den Experimenten abgeleiteten Mechanismen zu testen und anschließend nützliche Prognosen für reale technische Anwendungen zu erstellen.

Sowohl Kontinuums- als auch stochastische Modellierungstechniken werden verwendet, um die entsprechenden Mehrphasenströmungen in porösen Medien zu simulieren. In dieser Arbeit verwende ich ein stochastisches diskretes Wachstumsmodell: das makroskopische Invasions-Perkolationsmodell (IP). IP-Modelle haben gegenüber komplexen Kontinuumsmodellen den Vorteil, dass sie einfach und rechentechnisch wenig aufwändig sind. Lokale Veränderungen auf der Porenskala dominieren die Strömungsprozesse beim Gasausbreitung in wassergesättigten porösen Medien. IP-Modelle eignen sich besonders vorteilhaft für diese mehrskaligen Systeme, da die Simulation mit Kontinuumsmodellen extrem rechentechnisch schwierig sein kann.

Obwohl IP-Modelle eine rechentechnisch effiziente Möglichkeit bieten, die Mehrphasenströmung in porösen Medien zu simulieren, haben nur sehr wenige Forschungsarbeiten die Ergebnisse ihrer IP-Modelle mit den tatsächlichen experimentellen Bilddaten im Labor verglichen. Ein Grund dafür könnte die Tatsache sein, dass IP-Modelle keine Vorstellung von experimenteller Zeit haben, sondern nur einen ganzzahligen Zähler für Simulationsschritte, der eine zeitliche Reihenfolge impliziert. Die wenigen existierenden Studien zum Vergleich zwischen Experimenten und Modellen haben lediglich

eine subjektive Ähnlichkeit oder räumliche Momente als Vergleichsmaßstab verwendet. Einerseits ist der subjektive Vergleich zwischen dem Modell und den experimentellen Bildern mühsam und nicht objektiv. Andererseits kann der Vergleich der räumlichen Momente des Modells und der experimentellen Bilder zu irreführenden Ergebnissen führen, da Informationen aus den Daten verloren gehen. In dieser Arbeit wird eine objektive und quantitative Vergleichsmethode entwickelt und getestet, die die Grenzen dieser traditionellen Ansätze überwindet. Der erste Schritt besteht in einem volumenbasierten Zeitabgleich zwischen experimentellen Echtzeitdaten und den Ergebnissen des IP-Modells. Anschließend wird der *(Diffused) Jaccard coefficient* verwendet, um die Qualität der Anpassung zu bewerten. Die Übereinstimmung zwischen den Bildern der Modelle und der Experimente kann auf verschiedenen Größenmaßstäben überprüft werden, indem das Ausmaß der Unschärfe in den Bildern variiert wird.

Numerische Modellvorhersagen für nur unzulänglich bekannte Systeme (wie die Gastransportprobleme) leiden untergroßen konzeptionellen Unsicherheiten. In der Literatur werden Zahlreiche Versionen von IP-Modellen, die sich in ihren zugrundeliegenden Hypothesen unterscheiden, für die Simulation von Gas-strömungen in porösen Medien verwendet. Außerdem gehören die Gasinjektionsexperimente je nach Gasflussrate und Beschaffenheit des porösen Mediums zu kontinuierlichen, Übergangs- oder diskontinuierlichen Gasflussregimen. Aus der Literatur geht hervor, dass IP-Modelle für das diskontinuierliche Gasflussregime gut geeignet sind; andere Flussregime wurden nicht erforscht. Mithilfe der oben genannten Methode vergleicht die vorliegende Arbeit vier makroskopische IP-Modellversionen mit Daten aus neun Gasinjektionsexperimenten im Übergangsbereich und im kontinuierlichen Gasflussregime. Dieser Modellvergleich hilft, das Potenzial dieser Modelle in diesen unerforschten Regimen zu erkunden und die Quellen der konzeptionellen Unsicherheiten der Modelle zu identifizieren.

Alternativ dazu ist die Bayes'sche Modellwahl ein statistisches Standardverfahren für den systematischen und objektiven Vergleich verschiedener Modellhypothesen durch die Berechnung der Bayes'schen Modellevidenz (BME) anhand von Messdaten, wobei der Schwerpunkt auf der Parameterunsicherheit liegt. BME ist die Wahrscheinlichkeit, dass ein Modell die beobachteten Daten hervorbringt, wenn man die A-Priori Verteilung seiner Parameter berücksichtigt. Die Berechnung der BME kann eine Herausforderung sein: Exakte analytische Lösungen erfordern starke Annahmen; mathematische Näherungen (Informationskriterien) sind oft stark fehlerbehaftet; annahmefreie numerische Methoden (wie Monte Carlo) sind für große Datensätze rechnerisch unmöglich. In

dieser Arbeit wird eine BME-Berechnungsmethode entwickelt, um BME als Ranking-Kriterium für solche bisher unmöglichen Szenarien zu verwenden: Die *Methode der erzwungenen Wahrscheinlichkeiten*, für umfangreiche Datensätze und Markov-Chain-Modelle. Bei dieser Methode wird die Richtung der Berechnung vertauscht: Anstatt Tausende von Modellläufen auf zufälligen Modellrealisierungen mit den beobachteten Daten zu vergleichen, wird das Modell gezwungen, die Daten in jedem Zeitschritt zu reproduzieren, und die individuellen Wahrscheinlichkeiten des Modells nach diesen exakten Übergängen werden aufgezeichnet. Dies ist eine schnelle, genaue und exakte Methode zur Berechnung der BME für IP-Modelle, die die Eigenschaft einer Markov-Kette aufweisen, und für vollständige atomare Daten.

Die mit den in dieser Arbeit entwickelten Methoden und Werkzeugen erzielten Analyseergebnisse helfen, die Stärken und Schwächen der untersuchten IP-Modellkonzepte zu identifizieren. Dies hilft bei der Entwicklung und Verfeinerung von Modellen für die Gasmigration im Untergrund weiter. Außerdem tragen die gewonnenen Erkenntnisse zur Verbesserung experimenteller Methoden bei. Diese Werkzeuge und Methoden sind nicht auf Gasflusssysteme in porösen Medien beschränkt, sondern können auf jedes System mit Rasterdaten erweitert werden.

1 Introduction*

1.1 Background and Motivation

Gas migration in the subsurface is a phenomenon of environmental concern for several reasons. Gas migration from leaky oil and gas wells can reduce shallow groundwater quality. Further, stray gas in the subsurface can cause safety concerns due to the release of combustible gas and greenhouse gas emissions into the atmosphere [Vengosh et al., 2013, 2014]. A similar safety concern also exists for methane gas emissions from peatlands [Nisbet et al., 2016]. Another risk arises from the radioactive decay of the nuclide ^{226}Ra from the ^{238}U decay chain, which generates radioactive, carcinogenic radon (Rn) gas [Petermann et al., 2021]. ^{226}Ra is present in mostly all mineral and organic material and, therefore, Rn is constantly produced in rock and soil [Petermann et al., 2021]. Factors like soil grain size distribution or soil moisture can facilitate the release of Rn gas into the pore space and can eventually be emitted from the soil [Petermann et al., 2021]. Radioactive radon gas seepage from surrounding soils into building basements is a human carcinogen [Petermann and Bossew, 2021]. For subsurface carbon dioxide storage, gas migration through cap-rock fractures can contaminate shallow aquifers [Sakaki et al., 2013] and decrease the storage efficiency. Similar is the concern for geological storage of hydrogen [Woods and Norris, 2016, Reitenbach et al., 2015]. In the remediation of volatile organic compounds (VOCs) and non-aqueous phase liquids (NAPLs) in the subsurface, methods like in-situ air-sparging [Brooks et al., 1999] or thermal remediation [Hegele and Mumford, 2014] require an understanding of gas migration behaviour for efficient capture and removal of contaminants.

For the example applications mentioned above, knowledge of gas flow mechanisms in the subsurface is necessary to establish monitoring or investigative networks. The

---

*This chapter contains text fragments from my publications Banerjee et al. [2021], Banerjee et al. [2023] and Banerjee et al.

knowledge of probable flow paths of gas and the degree of contact between gas and water in the subsurface is essential for all these applications. However, here lies the challenge: *How does one observe detailed gas migration processes in the subsurface?* It is possible to dig and probe at a few locations in the field, but excavating the entire domain is unfeasible.

However, laboratory experiments can be conducted to gain insights into the processes associated with gas flow in the subsurface by mimicking the actual site characteristics but under controlled conditions. Numerical models are essential tools to encode and test hypotheses about the mechanisms at work that are observed and inferred from the experiments, and then provide further information about these subsurface systems and make useful predictions for such real-world engineering applications.

1.1.1 Immiscible Gas Flow in Saturated Porous Media

Gas flow in saturated subsurface environments is governed by *multiphase* flow physics in porous media. As these can be almost arbitrarily complex, some terminology is needed to specify the considered system. A phase is defined as matter with homogeneous chemical composition and physical states. Under normal conditions, solid, liquid and gaseous phases exist. The porous medium is the solid phase with pores, and these pores can be filled entirely or partially by a liquid phase, gaseous phase, or both. In the saturated subsurface, the soil is the porous medium, and its pore space is initially occupied by water (liquid phase). A gas phase flowing through this system can be miscible (e.g. carbon dioxide) or immiscible (e.g. methane) in the water phase. For simplicity, I consider gas flow in water-saturated soil as immiscible multiphase flow.

Several regimes of immiscible multiphase flow in porous media with different interface (between the fluids) patterns exist. Lenormand et al. [1988] investigated the interplay between *capillary* and *viscous* forces for immiscible fluids of different viscosity ratios. For such flows, Lenormand et al. [1988] used capillary numbers Ca (the ratio of viscous forces to capillary forces) and mobility ratio $\mathcal{M}$ (the ratio of the dynamic viscosities of displacing fluid to that of the displaced fluid) to describe the interplay between them. Experiments and simulations from Lenormand et al. [1988] identified three types of displacement fronts for this flow: stable displacement (no fingering), viscous fingering, and capillary fingering. A stable displacement front or a front with non-looping branched

fingers (viscous fingering) is observed when the viscous forces dominate (high Capillary numbers). The former happens when the displacing fluid is more viscous than the displaced fluid, and the latter is observed vice versa. Capillary fingering occurs in the dominance of capillary forces (low capillary numbers), where the displacement front spreads as looping fingers [Lenormand et al., 1988].

For vertical flows and when the density difference between the phases is high, like in a gas-water system, the effect of gravitational forces cannot be ignored. Thus, immiscible gas flow in a water-saturated porous medium is governed by the interplay between capillary, viscous *and gravitational* forces [Ewing and Berkowitz, 1998, Morrow, 1979, Løvoll et al., 2005, Van De Ven and Mumford, 2019]. The fluid interface can be stabilized or destabilized in the presence of gravitational or buoyant forces [Glass et al., 2000, Ewing and Berkowitz, 1998, Frette et al., 1992, Glass and Yarrington, 1996, Birovljev et al., 1991, Meakin et al., 1992, Van De Ven and Mumford, 2019], often described by the dimensionless Bond number Bo (the ratio of gravitational forces to capillary forces). For example, when a low-density fluid displaces a high-density fluid from the top, or a high-density fluid displaces a low-density fluid from the bottom in a vertical setup, buoyant forces stabilize the interface ($Bo > 0$) [Ewing and Berkowitz, 1998]. In the other scenarios, destabilization of the interface occurs ($Bo < 0$), and gravity fingering is observed [Glass and Nicholl, 1996]. Gas injection experiments in water-saturated porous media confirm that different displacement fronts are seen under different laboratory conditions [Ji et al., 1993, Brooks et al., 1999, Selker et al., 2006, Stöhr and Khalili, 2006, Geistlinger et al., 2006, Mumford et al., 2009].

Laboratory data on gas flow in water-saturated porous media can help us visualize and identify the involved gas flow processes in a controlled manner. The experimental data used in this thesis work are a series of gas-injection experiments in homogeneous water-saturated sand conducted in quasi-2-dimensional thin acrylic glass cells from Van De Ven and Mumford [2019]. The experimental data is obtained as a time-series of 2-dimensional images showing the gas evolution. By varying the gas injection rate, the experimental data spans various gas flow regimes (with different gas-flow patterns), which is detailed in Section 2.1.

1.1.2 Numerical Models: Focusing on Invasion Percolation Models

Numerical models from *continuum* and *stochastic rule-based* modelling approaches are used to describe such multiphase flows in porous media systems. On the one hand, continuum models are a near-accurate representation of the physical, real-world system, but they are complex, time-consuming and computationally intensive. On the other hand, stochastic rule-based discrete growth models are a simplified representation of reality based on many assumptions. They are simple, fast and computationally cheap. Amongst multiple stochastic rule-based models (e.g., Diffusion limited aggregation (DLA) [Paterson, 1984, Witten and Sander, 1983], Invasion-percolation (IP) [Wilkinson and Willemsen, 1983], anti-DLA [Meakin and Deutch, 1986]), this work focuses on various versions of (Stochastic) Invasion Percolation (IP) models at the macroscopic scale because their simplicity makes them a good candidate for stochastic analysis.

The *stochastic* analysis of models, facilitated by the IP approach, is important because gas flow processes in the subsurface are highly affected by small-scale variations in porous media. At scales larger than pore-scale, with experiments and numerical models, it is impossible to capture such minor scale effects on the gas flow. This leads to high uncertainty in the numerical model predictions. Stochastic analysis of these systems can help address their high uncertainty appropriately. Owing to their low computational effort, IP-type models are excellent candidates for such analysis.

IP models are 2-dimensional or 3-dimensional discrete growth models where a phase invades another phase-occupied porous network based on physics-based rules. These models can be built at different scales:

- pore scale, where the network simulates the exact arrangement of pore-space in a solid.

- macroscopic scale, where the network consists of an arrangement of upscaled pore-network blocks.

Hereafter, I will use the term "IP-type models" to refer to the entire class of IP model variations.

Moreover, Invasion Percolation (IP) models with a representation of gravity forces have been used for the upward migration of a low-density fluid (like gas) displacing a high-density fluid (like water) in a porous medium [Frette et al., 1992]. Many studies have used IP-type models with variations to model different types of gas flow systems in the porous media [e.g., Wilkinson, 1984, Wagner et al., 1997, Glass et al., 2001, Ewing and Berkowitz, 2001, Mumford et al., 2010, 2015, Trevisan et al., 2017, to name a few].

All numerical models have underlying assumptions and, therefore, need to be compared to actual experimental or field data to evaluate them. While IP models have the advantages like simplicity and low computational cost, they are challenging to calibrate, test or validate for the two reasons listed in Section 1.1.4.

1.1.3 Addressing Conceptual Uncertainty in Numerical Models

As highlighted in Section 1.1, gas flow in saturated subsurface is a sparsely known system. It is problematic to accurately capture the complex processes of gas flow in porous media, which occur at many different spatial scales. Due to this lack of knowledge, numerical model predictions suffer from high uncertainties in terms of both the parameters and model states. In IP-type models, the assumptions made for the simplified description of the complex gas-flow processes further increase the model's conceptual uncertainty. Also, the experimental measurements and methods are not error-free and, therefore, uncertain. The Bayesian inference framework allows one to tackle such model uncertainty aptly. *Bayesian Model Selection* (BMS) is a standard, often used, statistical procedure for systematic and objective comparison of different model hypotheses, wherein a prior belief in the model's accuracy is combined with its ability to reproduce a common data-set [Schöniger et al., 2014]. It requires the evaluation of Bayesian Model Evidence (BME), which is the likelihood of a model producing the observed data, given the prior distribution of its parameters.

Exact, fast analytical solutions for BME require strong assumptions that are hardly met in realistic settings [Schöniger et al., 2014]. So, other techniques involving mathematical approximations and numerical methods have been developed, but they all have limitations of their own [Höge et al., 2018]. Mathematical approximations (commonly known as Information Criteria (IC)) are based on different assumptions and/or asymptotics and are strongly biased in real-world applications. These criteria have been shown

to yield misleading model ranking results in real applications if their assumptions are violated [Poeter and Anderson, 2005, Ye et al., 2008, 2010b,a, Tsai and Li, 2008, 2010, Singh et al., 2010, Morales-Casique et al., 2010, Foglia et al., 2013].

Using *numerical methods* [Gideon, 1978] to compute BME avoids such assumptions but requires high computational effort. Numerical approximations that are commonly used for highly complex models are Monte Carlo (MC) methods with various sampling strategies [Schöniger et al., 2014, Kloek and van Dijk, 1978, Zellner and Rossi, 1984]. MC methods generally require large ensembles, the size of which is limited by the *available computational resources*. For high-dimensional problems (i.e. with many uncertain parameters), the so-called curse of dimensionality kicks in, requiring exponentially many model evaluations (massive ensembles) [Snyder et al., 2008, Bengtsson et al., 2008].

1.1.4 Challenges in Evaluating IP Models

Challenge 1: There is no time parameter in IP models.

There is no time parameter in IP-type models but only a model loop counter. This unawareness of the model towards time makes it hard to compare the models to real-time experimental or field data. Also, the missing time parameter makes it challenging to use IP-type models along with other models like reactive transport models, which are essential for subsurface carbon dioxide storage application [Oldenburg et al., 2016].

The time problem of IP-type models is traditionally handled in one of the following ways:

- The experimental image and the model output image are compared at characteristic/specific time points, like breakthrough time [Birovljev et al., 1991, Glass et al., 2001, Mumford et al., 2015, Trevisan et al., 2017].

- When an IP-type model is used in combination with a continuum model for transport (heat or mass), that transport controls the time scale, and the continuum model's time steps are used to compare to the real-time experimental data [Mumford et al., 2010, Molnar et al., 2019].

Challenge 2: Metrics for quantitative comparison of IP-type models to actual experimental or field data are lacking.

Various authors have presented many IP-type models [e.g., Wilkinson and Willemsen, 1983, Wilkinson, 1984, Kueper and McWhorter, 1992, Wagner et al., 1997, Berkowitz and Ewing, 1998, Glass et al., 2001, Tsimpanogiannis and Yortsos, 2004]. However, few studies have compared their models to actual (field or experimental) data. In the few studies of model-to-experimental data comparison, the comparison has been made

- either based on perceptual similarities, like the visible shape of gas clusters, channels or pools [Glass et al., 2001, Mumford et al., 2010, Trevisan et al., 2017]

- or by comparing spatial moments, which are aggregated statistical measures [Mumford et al., 2015].

A *perceptual* comparison is subjective, very time-consuming for large data sets due to its manual character, and may be deceitful due to a lack of objectivity. When comparing spatial *moments*, there is a loss of information from the data due to the aggregation of detailed images to just a few summary statistics. Also, when using several moments, it is unclear how to combine them into a unique metric.

The lack of studies that have compared their IP-type models to actual data is even more concerning because, despite several variations of IP-type models exist in the literature for simulating multiphase flow in porous media, their potential to be used for different applications remains vastly unexplored.

1.1.5 Challenges in Inter-Comparison of Models

A real-world system can be represented by many *competing conceptual models*. These models differ in their underlying hypotheses, which need to be tested against real-world observation data for their accuracy in representing the featured real-world system. Such comparisons can not only rank the models based on the accuracy of their predictions but also help identify the competing models' sensitive parameters and sources of conceptual uncertainty. This information can be used for refining these models. Moreover, this information might benefit experimentalists in designing their experiments.

Multiple variations of IP-type models exist in the literature, and experimental data from different gas flow regimes are available. Thus, the inter-comparison of these model versions is possible and highly valuable. As discussed in Section 1.1.4, it is difficult to calibrate test or validate IP-type models with real experimental or field data. These challenges (**Challenge 1** and **Challenge 2** from Section 1.1.4) *prohibit the inter-comparison* of IP-type model versions using available experimental data, despite the importance of such model inter-comparison studies.

Alternatively, as mentioned in Section 1.1.3, BMS is an efficient tool for inter-comparison of competing models. Recall that BME-computation methods have limitations of their own. Out of the different methods, MC-based numerical methods to compute BME, are bias-free but computationally expensive, especially for high-dimensional problems. Additionally, for highly accurate or informative data sets, the overlap between predictive distributions and observed data may be so small, that MC methods may not result in a meaningful BME value (> 0) at all. Hence, computation of BME is a challenge for extensive data sets, e.g., highly resolved in space/time like experimental movies or images in time. Thus, despite the efficacy of the BMS concept in model inter-comparisons for systems with high uncertainties, the computation of BME for IP-type models and extensive experimental data sets is practically infeasible.

Challenge 3: Evaluation of BME for high dimensional problems and extensive data sets is practically infeasible.

1.2 Goals and Approach

1.2.1 Goals and Scope

The primary goal of my thesis is to advance the understanding of gas migration behaviour in the subsurface through the stochastic analysis of the system using experimental data, numerical modelling, and systematic inter-comparison of models.

As previously discussed, simple rule-based models are well suited for stochastic analysis: hence, I pick existing macroscopic variations of IP models and generate new re-combinations for my study to match the scale of the experimental data. From the challenges identified above, it is clear that these models have not been tested to their

full abilities. With the contributions of my thesis, I intend to overcome the challenges associated with testing these macroscopic IP models. This will advance modelling capabilities for such models, especially for gas flow systems in saturated porous media.

In particular, I develop analysis tools for assessing the performance of the models under study. The findings obtained using these tools can aid the modellers in refining these models. Further, I conduct model inter-comparisons to rank their performance and identify model-specific sensitive parameters for predicting gas flow in water-saturated sand. Also, through my analysis, I aim to address and reduce the uncertainties associated with gas flow systems in porous media.

1.2.2 Research Questions and Contributions

First, looking back at **Challenge 1** identified in Section 1.1, IP-type models do not have a notion of experimental time but only have an integer counter for simulation steps that imply a time order. Besides, the current frameworks for comparing IP-type models to experimental or field data are neither systematic nor objective and, most importantly, not quantitative (see **Challenge 2**, Section 1.1.4). Thus, the **first objective** of my thesis is to answer the following question:

RQ1: *How to appropriately compare time-ignorant macroscopic IP models to time-dependent experimental image data?*

Second, gas flow in saturated porous media can belong to different flow regimes (with varied gas-flow patterns) depending on the flow rate and the porous medium's nature [Geistlinger et al., 2006]. I will further detail this in Section 2.1 of Chapter 2. Numerous variations of IP-type models have emerged that can be used for simulating gas flow in water-saturated porous media. However, the few studies where IP-type models were compared to experimental data have focused on a particular regime of gas flow. The **second objective** of this thesis is, therefore, to test the performance of competing macroscopic IP-type model versions on a range of gas-injection experiments belonging to different previously unexplored gas-flow regimes. For this purpose, it is necessary to overcome the **Challenges 1 and 2** outlined in Section 1.1.4, which leads to the

research question:

RQ2: *Using the comparison approach developed in research question 1 on the different macroscopic IP model versions, how to determine which model version is better at describing which of these gas-flow regime experiments? Can specific deficits and recommendations be derived?*

Third, looking at **Challenge 3**, from Section 1.1.5, it is practically infeasible to compute BME for massive data sets and use the standard statistical procedure of Bayesian model selection to compare IP-type models in the presence of large and detailed experimental data sets. This brings us to the **third objective** and research question of this research:

RQ3: *How can we efficiently compute Bayesian Model Evidence for extremely large data sets like highly space-time resolved image data, knowing that all existing computational algorithms would be computationally infeasible? If yes, can we pinpoint very detailed strengths and weaknesses of the models?*

Together, the answers to these three research questions pose an attempt to close the elicited gaps above and shall foster increasing IP modelling capacities for gas migration in water-saturated porous media and address the often neglected different levels of uncertainty that prevent their widespread usage.

1.2.3 Approach and Outline

To answer RQ1, I first develop a volume-based time matching method between the model output and the experimental data. Then, I transfer the so-called Jaccard coefficient metric from image processing to assess the quality of fit between time-matched model images and experimental images. I introduce a diffused version of the Jaccard coefficient for matching across various scales of pixel clarity. I demonstrate the method by comparing a particular macroscopic IP model to data from one experiment of Van

De Ven and Mumford [2019]. Also, I test the performance of my comparison method against the traditional approaches mentioned in Section 2.4.

To answer RQ2, I use the above comparison method to test and rank the performance of four macroscopic IP models with data from nine experiments [Van De Ven and Mumford, 2019] that belong to different gas flow regimes. These experiments belong to a flow regime where IP models have not been tested before. Some of these models are new re-combinations of existing model ideas. I run this comparison of the competing models under varying amounts of pixel diffusion and derive conclusions on the models' skills and deficits for possible future model improvements. Further, I also calibrate some model parameters in this comparison study to understand and discuss their impact on the models' performance.

Finally, **to answer RQ3**, I develop the Method of Forced Probabilities for BME computation. In this method, the direction of evaluation of BME is swapped: instead of comparing thousands of forward model runs on random parameter realizations with the experimental movies, I force the models to reproduce the data in each time step and record the individual probabilities of the model following these exact transitions. MFP is applicable for Markov-chain models and data showing all "atomic" events, where "atomic" will be defined in Chapter 5. I use a particular IP model version, synthetic data, and high-quality data from a real experiment of Van De Ven and Mumford [2019] to illustrate and test the method. As this BME-based model comparison is much stricter than the Jaccard coefficient metric, additional recommendations for model refinement are derived.

Thesis Outline

To begin, in Chapter 2, I state the fundamentals of gas-water (multiphase) flow in porous media, specifically required to understand the macroscopic IP models and the gas-injection experiments used in this study. Also, I discuss the state of the art of macroscopic IP models, experiments, and existing comparison methods of the IP-type models to experimental data. Further, I introduce the mathematical concepts and formulations of the Bayesian model selection framework. Then, in the next three chapters, I present and discuss my contributions as answers to the research questions delineated above.

- In Chapter 3, I address **RQ1** and provide the details of the comparison method developed for IP-type models and gas-injection experiments in porous media.

- To address **RQ2**, in Chapter 4, I describe the comparison of four different macroscopic IP models with data from nine gas-injection experiments, using the comparison method described in Chapter 3.

- I discuss in Chapter 5 my newly developed method devised to compute BME for the problem of interest, i.e., having massive data sets, thus addressing **RQ3**.

Finally, I provide a broad set of conclusions deduced from the answers to the aforementioned RQs and discuss the potential for future research in Chapter 6.

2 State of the Art: Models, Experimental Data and Methods*

The interactions of capillary forces, viscous forces, and gravitational forces result in different gas flow regimes. The conception of these flow regimes is crucial to understand the modelling concepts and the experimental data used in this study. Thus, to begin, I introduce these gas flow regimes and discuss the resulting flow patterns in Section 2.1. Then, in Section 2.2, I briefly describe the experimental data sets used for this study. I list and delineate the macroscopic IP models used in this study in Section 2.3. To facilitate the comprehension of my contributions, I discuss the existing methods to compare IP-type models using experimental data in Section 2.4 and the mathematical formulations of Bayesian Model Evidence in Section 2.5.

2.1 Gas Flow Regimes

Lenormand et al. [1988] described immiscible multiphase flow regimes based on capillary numbers (Ca) and viscosity ratios ($\mathcal{M}$). Further, for gas-water type fluids, additionally, gravitational forces need to be taken into consideration (see Chapter 1, Section 1.1.1). Berkowitz and Ewing [1998] extended the flow regime diagram of Lenormand et al. [1988] (see Figure 2.1**a**) in Ca-$\mathcal{M}$ space, along a third dimension to create the Ca-$\mathcal{M}$-Bo diagram (see Figure 2.1**b**). The systems of my interest in this study are of upward gas migration in water-saturated soils. It is a gravity-destabilized flow domain ($Bo < 0$) (marked by the red arrow in Figure 2.1**b**).

---

*This chapter contains text fragments from my publications Banerjee et al. [2021], Banerjee et al. [2023], Banerjee et al. and some figures from Banerjee et al..
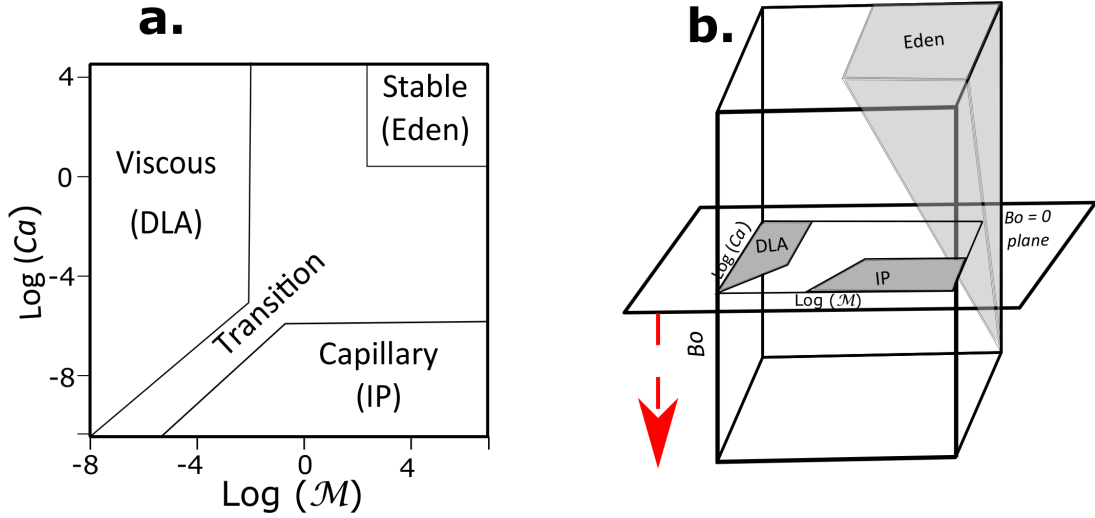
Figure 2.1: Immiscible flow regime diagrams. The figure **a** is redrawn using Figure 8 of Lenormand et al. [1988] (Copyright Cambridge University Press, reproduced with permission) as a guide, where immiscible multiphase flow regimes, along with suitable modelling techniques, were distinguished based on Ca and $\mathcal{M}$ values. DLA (Diffusion Limited Aggregation), IP (Invasion Percolation), and Eden are different discrete growth models. The figure **b** is redrawn using Figure 10 of Berkowitz and Ewing [1998] (Copyright Kluwer Academic Publishers, reproduced with permission) as a guide, who conceptually extended the diagram **a** along a third dimension containing the Bo values. The red arrow depicts the $Bo < 0$ domain.

For upward gas migration in water-saturated soils, in a given porous medium, at low gas injection rates, the viscous effects are less relevant. Therefore, the flow is controlled by a combination of capillary forces (capillary fingering regime) and gravitational forces. Upon increasing the injection rates, the control shifts to a combination of viscous forces (viscous fingering regime near the injection source) and gravitational forces [Selker et al., 2006, Van De Ven and Mumford, 2019]. Therefore, three gas flow regimes are observed [Ji et al., 1993]. These are:

- The **Continuous/Coherent** flow, where the gas phase flows as a continuous phase.

- The **Discontinuous/Incoherent/Bubbly** flow, which involves gas flow as discrete gas bubbles or clusters. During the flow, these gas bubbles or clusters of-

ten undergo fragmentation (splitting of gas bubbles or clusters) and coalescence (merging of disconnected gas bubbles or clusters) events.

- The **Transitional** flow, where gas-flow behaviour exhibits characteristics of both continuous and discontinuous flow.

The *transition of gas flow* from one regime to another depends on the grain size of the porous medium and on the rate of gas flow [Geistlinger et al., 2006]. As a result of the balance of forces, the gas-flow regime tends to be discontinuous at low gas-flow rates and in coarser porous media moving towards the continuous regime as the flow rate increases or for finer porous medium [Geistlinger et al., 2006]. Geistlinger et al. [2006] defined a critical flow rate Q_{crit} [m^3/s] below which discontinuous gas flow occurs:

$$Q_{crit} = \frac{\pi \Delta \rho g r_c^4}{8 \mu_g},$$
(2.1)

where $\Delta \rho$ denotes the difference in densities between gas and water [kg/m^3], g denotes acceleration due to gravity [m/s^2], r_c denotes the characteristic radius of gas channels through which flow occurs [m] and μ_g denotes the dynamic viscosity of the gas phase [Pa $-$ s]. Besides using the critical flow rate, the gas flow regimes can be classified using the ratio of Bond number to Capillary number (Bo/Ca) [Van De Ven and Mumford, 2019], which are reported for the experiments used in this study.

2.2 Experiments

It is notoriously difficult to obtain direct measurements in the subsurface to observe the behaviour of the phases because even minimally-invasive methods distort the medium that shall be investigated. So, *indirect measurements* using laboratory experiments under varied controlled conditions in a representative porous medium are often used as an alternative for which the distortion can at least be described or even be quantified to a certain extent. Non-invasive imaging methods like optical imaging using UV or visible light, dual-energy gamma radiation, X-ray microtomography, and magnetic resonance imaging are a few popular choices for such laboratory experiments [Oostrom et al., 2007, Werth et al., 2010].

In this thesis, I use data from *imaging experiments* using visible light, specifically the experimental data sets from the study of Van De Ven and Mumford [2019] (see Table 2.1 for details). A general description of the experimental set-up and procedure is presented in this section based on Van De Ven and Mumford [2019] to aid the understanding of the contributions of this thesis.

In these experiments, gas (air) is injected at various flow rates in a water-saturated, homogeneous, sand (0.7mm average grain size)-filled thin acrylic cell of dimensions 25cm×25cm×1cm (see Figure 2.2 for a schematic of the cell). A continuous wet packing procedure was used to ensure that the resulting sand distribution was homogeneous and free of trapped gas [Mumford et al., 2009, Hegele and Mumford, 2014, Van De Ven and Mumford, 2018]. After packing the cell fully, the top of the cell was sealed, to prevent re-arrangement of soil grains. After that, the cell was placed in front of a light source. Then, gas was injected at some point in the cell with a syringe pump at a constant flow rate (see injection rates in Table 2.1). To conduct the experimental triplicate at 10ml/min (10-A, 10-B, 10-C), 100ml/min (100-A, 100-B, 100-C) and at 250ml/min (250-A, 250-B, 250-C), the sand was washed and repacked with the same procedure to obtain a homogeneous packing after each experiment. Nevertheless, with a new arrangement of all grains and the inherent instability of gas migration in certain flow regimes, each experimental outcome is unique.

A camera captures the light transmission images of gas movement and resulting gas presence within the cell at a designated time rate, either until the gas reaches the top of the cell or until the memory of the camera is exhausted. In the experiments used in my thesis, images are collected at the rate of 30 frames per second until the completion of the experiment. The obtained images were then converted to grey-scale images and thereafter processed to detect gas presence or to obtain gas-saturation images [Niemet and Selker, 2001]. This experimental technique is called the *Light Transmission Method* [Tidwell and Glass, 1994] (see Figure 2.2). The details of the image processing technique as well as the technique for processing the images to obtain gas-saturation data, are discussed in Appendix A. In this thesis, to retain simplicity, I will use a time-series of the processed gas presence/absence type binary images or experimental movies.

To obtain the binary images, individual pixel intensity values of the raw images are averaged over a block size of 1mm×1mm. Then, optical density values are computed per block, and a detection limit of 0.02 was set [Van De Ven and Mumford, 2019]. Optical
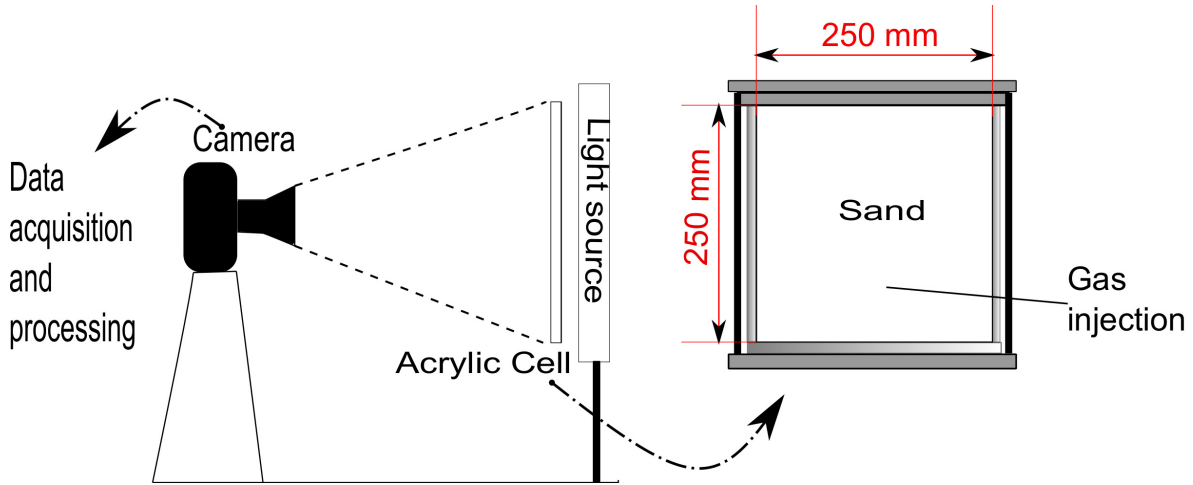
Figure 2.2: Schematic of experimental setup. The Light Transmission Method schematic is redrawn using Figure 1 of Tidwell and Glass [1994] as a guide, and the sketch for the acrylic cell is redrawn using Figure 1 of Van De Ven and Mumford [2018] as a guide.

density is defined as the negative logarithm transform of the ratio of the transmitted to incident light intensity [Kechavarzi et al., 2000]. Wherever the block intensity exceeds the detection limit, gas is considered to be present.

From these binary image data obtained using the optical density values, the difference in gas-invasion patterns for different gas injection rates in the same homogeneous porous medium is observed. At a low injection rate of 0.1 ml/min, gas flows with fragmentation and coalescence behaviour (see Figure 2.3) as seen in discontinuous gas flow regimes (see Section 2.1) [Van De Ven and Mumford, 2019]. For higher injection rates (100ml/min, 250ml/min), we see more branching effects and the development of multiple coherent fingers of gas (see Figure 2.3) across the domain (continuous flow regime). With increasing gas flow rate, viscous forces dominate the injection zone, making the gas flow radial around the injection point [Selker et al., 2006, Van De Ven and Mumford, 2019]. However, once the gas propagates further away from the injection point, gravitational forces overcome the viscous forces [Van De Ven et al., 2020]. Hence, the upward movement of gas is observed as multiple fingers (referred to as gravity fingering in Glass and Nicholl [1996]). The experimental triplicate at 10 ml/min belongs to the transitional gas flow regime (see Section 2.1).

Table 2.1 contains a summary of the experiments used in this study taken from Van De Ven and Mumford [2019]. It contains the experiment number, gas-injection rate,

porosity of sand, total duration of the experiment, Bo/Ca, and gas flow regime of the corresponding experiment. The porosity of a porous medium is defined as the ratio of the volume of pore space to the total volume of the porous medium.

Experiment Nr.	Injection rate [ml/min]	Porosity	Duration [s]	Bo/Ca	Gas flow regime
0.1-A	0.1	0.366	330	-1.61×10^4	Discontinuous
10-A	10	0.375	8.6	-1.61×10^2	Transitional
10-B	10	0.360	9.4	-1.61×10^2	Transitional
10-C	10	0.369	9.4	-1.61×10^2	Transitional
100-A	100	0.370	6.3	-1.61×10^1	Continuous
100-B	100	0.365	5.2	-1.61×10^1	Continuous
100-C	100	0.360	4.8	-1.61×10^1	Continuous
250-A	250	0.366	4.4	-6.45×10^0	Continuous
250-B	250	0.379	6	-6.45×10^0	Continuous
250-C	250	0.364	6.4	-6.45×10^0	Continuous

Table 2.1: Summary of experiments used in this study based on Table 1 from Van De Ven and Mumford [2019]. The experiments were conducted by the group of Dr. Kevin Mumford at Queen's University, Canada. The duration of the experiments may slightly differ from the ones reported in Van De Ven and Mumford [2019] due to rounding up during data processing.

2.3 Models

Immiscible flow in porous media, where each pore arrangement is not known, can be simulated primarily by using two modelling techniques, i.e. so-called continuum or stochastical modelling. I will focus on macroscopic stochastic versions of Invasion Percolation models (Section 2.3.2) and describe four versions used in this study (Sections 2.3.3 — 2.3.6).

2.3.1 Classification of Modelling Approaches

Continuum Modelling Technique
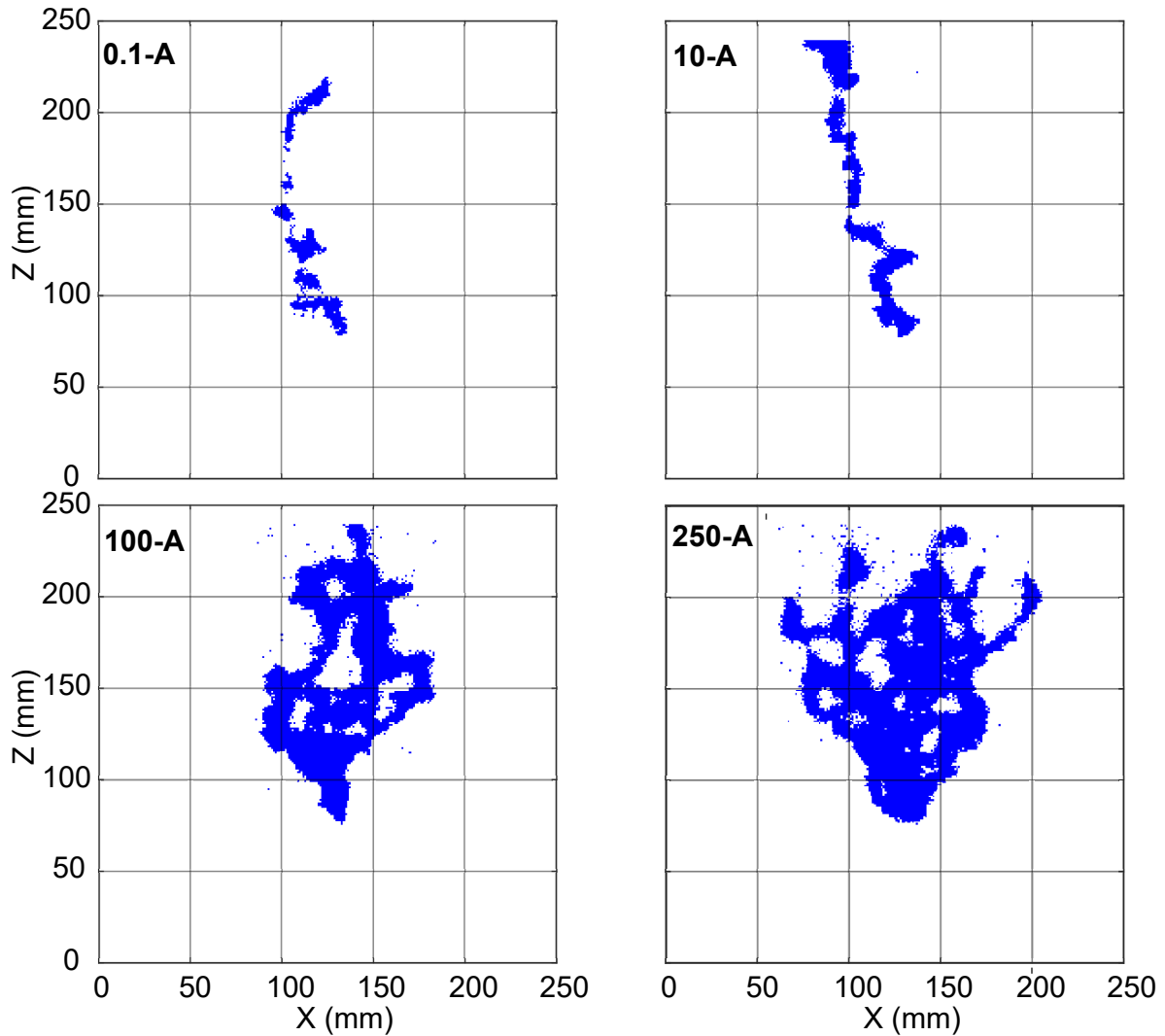
Figure 2.3: A sample of four binary experimental images at the final time for experiments 0.1A, 10A, 100A, and 250A.

Continuum models are Darcy-law [Holden, 2005] based fluid transport models defined at the scale of a representative elementary volume (REV). A REV is the smallest model unit at which individual pore-level geometrical details are smoothed out. Thus, averaged values of parameters describing the physical processes can be used. These models are highly complex with a large number of parameters and can be coupled to different physical and chemical processes for a near-accurate representation of the physical, real-world system. They involve solving partial differential equations with desired spatial and temporal discretizations. Additionally, to address the description of multiphase flow in porous media, relative permeability of phases and capillary pressure-

saturation curves are used. Owing to their complexity, these models are non-linear and computationally expensive.

Moreover, gas migration processes are highly influenced by perturbations at the pore scale. On the one hand, to incorporate pore-scale heterogeneities correctly, a finer mesh discretization is required for these models. On the other hand, this further increases the computation time. Coarser mesh discretizations are subjected to artefacts of numerical dispersion that smooth out the pore-scale heterogeneities [Glass et al., 2001]. The different length scales involved in the processes of gas migration in the porous medium make the use of continuum models difficult [Glass et al., 2001]. This reduces the prediction capability of such models for gas migration processes because they are highly influenced by pore-scale perturbations.

Stochastic Modelling Techniques

Stochastic modelling techniques involve the use of simple discrete growth models (see Section 1.1.2), which capture the essential physics of the processes and generate flow patterns without solving differential equations. Thus, these models have low computational effort. Both laboratory experiments and numerical model formulations of a real-world system are not free from uncertainties. While laboratory experiments can have uncertainty associated with measurements or processing techniques, numerical models can suffer from conceptual and parameter uncertainty, affecting their prediction quality. A stochastic analysis of real-world systems helps to address these uncertainties appropriately. *Discrete growth models* are ideal candidates for such analysis. Out of many discrete growth models, I focus specifically on Invasion Percolation (IP) models.

2.3.2 Invasion Percolation Models

Invasion Percolation (IP) models are (stochastic) discrete growth models often used for simulating displacement of immiscible fluids through porous media in the capillary fingering regime [Lenormand et al., 1988]. The term Invasion Percolation was first coined by Wilkinson and Willemsen [1983] for a pore-scale model, which incorporated phase accessibility rules to standard Percolation models of Broadbent and Hammersley [1957] to assure connectivity within a phase.

General Implementation Procedure

Many IP model versions with variations in the underlying rules have been developed to match the behaviour of specific fluids in specific porous media under specific conditions [e.g., Ewing and Berkowitz, 1998, 2001, Birovljev et al., 1991, Kueper and McWhorter, 1992, Frette et al., 1992, Ioannidis et al., 1996, Glass et al., 2001, Mumford et al., 2015, Trevisan et al., 2017, to name a few]. However, all of them have the following typical conceptual and numerical implementation:

1. At first, a pore network of blocks/nodes is generated with a given connectivity by assigning each pore an invasion/entry threshold selected from some distribution. This network can be 2D (2-dimensional) or 3D (3-dimensional).

2. Initially, all the blocks are occupied by the defending fluid, which is the fluid that initially exists in the domain. Then, the invading phase is injected at some point in the network. For example, in this thesis, *water* is the *defending* fluid, and *gas* is the *invading* fluid.

3. Pores with connection to the invaded pore are evaluated for their entry thresholds, and, based on some criterion (mostly minimum entry threshold), one of the connected blocks is invaded.

For my thesis work, the defending phase, *water*, is the wetting phase and the invading phase, *gas*, is the non-wetting phase. In a multiphase system, the solid porous matrix prefers to be in contact with one fluid phase more than the other. This preferred phase is the wetting phase, which thus flows through the smaller pores of the matrix. The non-wetting phase favours the larger pores of the solid matrix for flow.

IP models also need to incorporate buoyancy effects to simulate gas invasion in water-saturated porous media. Several studies have therefore used IP models with gravitational/buoyant force effects to model gas-water flow systems or fluid systems with significant density-difference in porous media [e.g., Frette et al., 1992, Birovljev et al., 1991, Meakin et al., 1992, Ioannidis et al., 1996, Held and Illangasekare, 1995, Glass and Yarrington, 1996, Tsimpanogiannis and Yortsos, 2004, Cavanagh and Haszeldine, 2014, Trevisan et al., 2017].

Macroscopic Invasion Percolation (IP) Model

The pore-scale IP models described above must be upscaled to use them for large engineering applications: like subsurface contaminant remediation, oil extraction, geologic

gas storage etc.; i.e., any scale larger than the pore-scale. Studies [like Kueper and McWhorter, 1992, Ewing and Gupta, 1993, Ioannidis et al., 1996] abstracted processes from the pore-scale IP model to then use them at the larger scales of their problems. Macroscopic IP models conceptualize the porous medium as a group of internally homogeneous isotropic blocks consisting of sub-networks of pores instead of individual pores as in pore-scale IP models [as of Wilkinson and Willemsen, 1983]. Macroscopic IP models are a reasonable choice for scales greater than or equal to the experimental data used in this study.

Model Versions Used in This Study

I use four versions of the macroscopic IP model:

1. The Near-Pore Macro-Modified Invasion Percolation (NP-MMIP) model of Glass et al. [2001] without viscous modifications.

2. The Macro-IP model involving a rule for re-invasion of water [Glass and Yarrington, 2003, Mumford et al., 2015].

3. A combination of the Macro-IP model with a rule that allows for more than one invasion block per step (including the original viscous modification as in Glass et al. [2001]).

4. A combination of the Macro-IP model and modified stochastic selection rule of the Stochastic Selection and Invasion (SSI) model of Ewing and Berkowitz [1998] adapted from Mumford et al. [2015].

All four model versions are coded using MATLAB. Also, they are at the same scale, adopt a 2D grid description of the porous medium in accordance with the experimental data, and share some similarities. Figure 2.4 shows the conceptual building of the four model versions used in this study.

To facilitate the understanding of the models, first, I describe the model version (I call it **Model 1**) based on the NP-MMIP of Glass et al. [2001] (Section 2.3.3). Model 1 does not include the modifications for viscous effects from the NP-MMIP model of Glass et al. [2001]. Then, in Section 2.3.4, I introduce **Model 2**, which has additional rules of re-invasion of water at the macroscopic scale, same as in Glass and Yarrington [2003], Mumford et al. [2015] (see Figure 2.4). I combine Model 2 and a rule for producing thicker fingers from the viscous modification of NP-MMIP model of Glass et al. [2001]
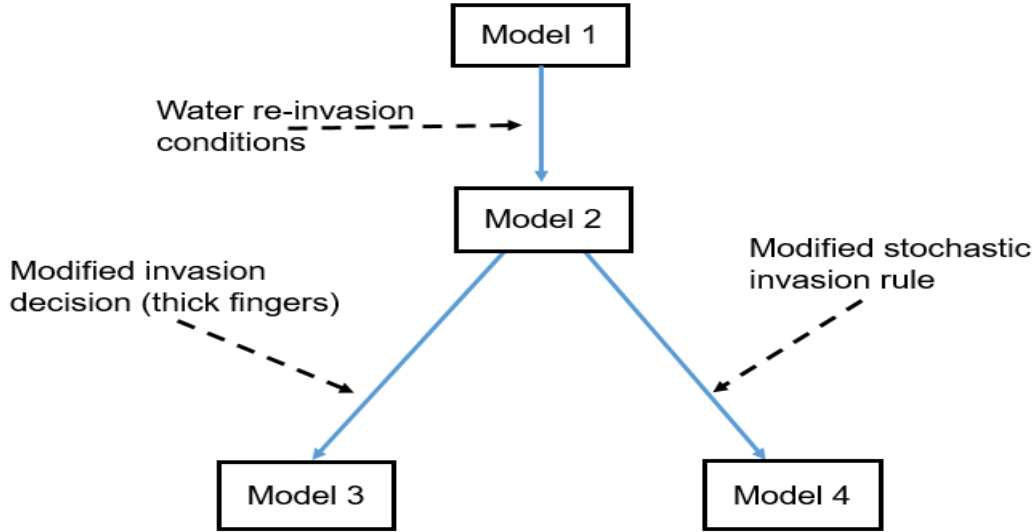
Figure 2.4: Flowchart illustrating the building process of the competing model versions used in this thesis.

to produce **Model 3** (Section 2.3.5), to resemble the experimental outcomes (see Figure 2.4). Finally, I describe the fourth model version: **Model 4**, in Section 2.3.6, which is built by combining Model 2 and a modified rule for stochastic invasion from Ewing and Berkowitz [1998] (see Figure 2.4). Model 4 is adapted from Mumford et al. [2015]. All the model versions used here generate binary images (gas-presence/gas-absence) as output.

2.3.3 Model 1

In this model, the gas is placed at the injection block (position of the gas injection needle in the experiment), and the invasion thresholds (T_e) [cm of H_2O] of the neighbouring blocks are calculated:

$$T_e = P_e + P_w, \tag{2.2}$$

where P_e is the local entry pressure of the block [cm of H_2O], and P_w is the pressure of the water phase [cm of H_2O]. P_e is the specific value of capillary pressure (P_c) required by gas to percolate a water-occupied block. Capillary pressure (P_c) is the difference in

pressure across the interface of two immiscible phases in pore space. P_w incorporates the buoyant effects and is calculated assuming hydrostatic conditions:

$$P_w = \rho_w g z \qquad (2.3)$$

Here, ρ_w is the density of water [kg/m^3], g is the acceleration due to gravity [m/s^2], and z is the height [m] from the top of the acrylic glass cell. At each model step, the neighbouring block with the minimum invasion threshold (T_e) is invaded by gas.

The P_e field of a porous medium depends on the pore-scale arrangement of the solid and its interaction with the fluids. A precise measurement of the P_e field at the scale of the experiments (block size of 1mm x 1mm) in this thesis is practically impossible. Therefore, it is typical to use random P_e fields, i.e. a randomly generated value per block. Since P_e is a point on the capillary pressure (P_c)–saturation (S) curve, the model randomly samples the P_e values that it assigns individually to all model blocks, using the Brooks-Corey $P_c - S$ relationship [Brooks and Corey, 1964] for the material of interest (homogeneous sand of 0.7mm average grain size):

$$S_e = \left(\frac{P_c}{P_d}\right)^{-\lambda}, \qquad (2.4)$$

where S_e is the effective wetting phase saturation. The saturation of a fluid phase is a dimensionless quantity defined as the percentage of pore space occupied by that fluid phase. P_c is the capillary pressure [cm of H_2O] and P_d is the macroscopic displacement pressure [cm of H_2O]. P_d is the capillary pressure of the largest pore-throat that the gas phase needs to overcome to invade the porous medium [Gerhard and Kueper, 2003]. λ is the pore-size distribution index. The value of λ varies typically between 1-4 and can be up to 7 for very uniform sands. The model samples the P_e values from the inverse of the cumulative distribution function of P_c (using Equation 2.4):

$$P_c = P_d \mathcal{U}^{-\frac{1}{\lambda}} \qquad (2.5)$$

Here, $\mathcal{U}$ is a random number from the standard uniform distribution on the interval $[0, 1]$. This sampling method is called the Inverse Transform sampling method, which

has been used in the works of Glass et al. [2001], Mumford et al. [2015], Banerjee et al. [2021]. The P_e values thus assigned to the blocks are not spatially correlated, but this extension could be achieved via geostatistical simulation.

2.3.4 Model 2

Model 2 has the same setup and follows the rules for invasion of gas specified for Model 1 (Section 2.3.3). This means it follows Equations 2.2 — 2.5 and also obeys the rule of invading the neighbouring block with the minimum T_e. Furthermore, it has a rule for re-invasion of water into the gas-occupied blocks to simulate the fragmentation and mobilization events observed for discontinuous gas flow (see Section 2.1) [Glass and Yarrington, 2003, Mumford et al., 2015]. This rule is an upscaled version of the re-invasion rule of the pore-scale model of Wagner et al. [1997].

In Wagner et al. [1997], the re-invasion of water (causing fragmentation and mobilization) into the gas-filled pores is realized by a withdrawal pressure threshold. At the scale of the Macro-IP model, the threshold for re-invasion, also known as the terminal threshold (T_t) [cm of H_2O], is calculated as the summation of the terminal pressure (P_t) [cm of H_2O] and the hydrostatic pressure (P_w).

$$T_t = P_t + P_w \tag{2.6}$$

Before defining P_t, some more domain terms must be defined. When a non-wetting phase invades a wetting-phase-occupied porous medium, the process is called drainage. The reverse process is called imbibition. The $P_c - S$ curves associated with these processes differ for any particular porous medium. This behaviour is called capillary pressure hysteresis. The terminal pressure (P_t) is the minimum capillary pressure attainable by a non-wetting phase cluster undergoing imbibition [Gerhard and Kueper, 2003]. P_t is calculated using the P_e- to $-P_t$ ratio (α) obtained from the characteristic drainage and imbibition curves for the porous medium of interest, which takes capillary-pressure hysteresis into account [Gerhard and Kueper, 2003, Mumford et al., 2009]. The same α value is assigned to each block, which is reasonable for uniform sands like the one used in this thesis [Mumford et al., 2015].

$$P_t = \alpha P_e \tag{2.7}$$

Water re-invades a gas-occupied block if:

$$T_{t,g} > T_{e,w}, \tag{2.8}$$

where g and w stand for gas- and water-occupied blocks, respectively [Mumford et al., 2015]. Thus, in a gas cluster when the maximum $T_{t,g}$ value is greater than the minimum $T_{e,w}$ value of its neighbouring water-occupied blocks, water re-invades the gas-occupied block with the maximum $T_{t,g}$ value. The model assumes that it completely expels the gas when water re-invades a gas-occupied block. As a result, the expelled gas occupies the block with the minimum $T_{e,w}$ value. If the re-invasion of water occurs in blocks on the periphery of the gas cluster, mobilization occurs. If the re-invasion causes a disconnection in the gas cluster, fragmentation occurs. In any model step, a gas cluster is allowed to grow, i.e. the number of gas-invaded blocks is more than in the previous step, only when connected to the gas cluster containing the injection point to ensure mass balance. Thus, for gas clusters disconnected from the injection point, only the re-arrangement of blocks is possible.

2.3.5 Model 3

Model 3 includes an invasion rule of Glass et al. [2001] to the Model 2 implementation. In this regard, the model formulation follows the rules specified by the Equations 2.2 — 2.8. The difference is that multiple neighbouring blocks (nb) are invaded instead of one block per step. This means that not only the easiest-to-invade block is invaded, but the nb easiest ones among all candidate blocks. This weakens the influence of T_e and hence resembles a reduced dominance of capillary effects in favour of viscosity effects. The number of blocks to invade is chosen by observing the gas fingers from the experimental data.

Please note that, in this implementation, the number of blocks invaded is chosen dynamically until the number of blocks specified at the beginning of the simulation is available for invasion. For example, in a model run specified to invade, say, $nb = 10$

blocks per step, initially, when the number of available neighbours is < 10, all the available ones are invaded. Ten neighbouring blocks are invaded only when the gas cluster around the injection point is big enough to have ≥ 10 neighbouring blocks. After each event of an invasion of multiple blocks, re-invasion of water resulting in fragmentation or mobilization of the gas cluster is carried out exactly as described in Model 2. This means that the simulation of the fragmentation and mobilization event in Model 3 does not involve gas invasion of multiple water-occupied neighbouring blocks.

2.3.6 Model 4

Model 4 is implemented following the formulations specified by Equations $2.2 - 2.8$. Model 2 selects the neighbouring block with a minimum invasion threshold (T_e) for invasion. In contrast, in Model 4, the neighbouring block is chosen using a modified rule for stochastic selection from the Stochastic Selection and Invasion (SSI) model of Ewing and Berkowitz [1998]. This rule allows gas to invade not strictly only the block with the minimum invasion threshold (T_e) but also less easy-to-invade blocks based on a partially randomized choice. The difference between Model 3 and Model 4 is that Model 3 diminishes the influence of T_e deterministically for many blocks per step, while Model 4 achieves the same stochastically for a single block per step.

The stochastic selection rule of the original SSI model accounted for viscous effects (instabilities and randomness brought into the system by the fluids' interaction with a porous medium) and was originally applied to dense non-aqueous phase liquid (DNAPL) migration [Ewing and Berkowitz, 1998]. Viscous effects cannot be ignored for gas flow at high injection rates. This stochastic selection rule has been modified to be applicable for gas invasion in water-saturated sand [Mumford et al., 2015] instead of the DNAPL invasion of the original work. In the modified stochastic selection rule of the SSI model, the decision of gas invasion is still proportional to the T_e values of the neighbouring blocks but is slightly modified using an additional parameter: c, called the cell selection weighting factor [Ewing and Berkowitz, 1998].

In the modified rule for stochastic selection:

1. The list of T_e values of the neighbouring blocks (n) of the gas cluster are arranged

in an ascending order $T_{e,asc}$ and the cumulative sum $T_{e,cum}$ is evaluated:

$$T_{e,cum}[i] = \sum_{j=1}^{j=i} T_{e,asc}[j]; i = 1, 2, 3, \ldots, n \qquad (2.9)$$

2. Then the first block (value of i) where the rule specified by Equation 2.10 is found true is invaded by the gas:

$$T_{e,cum}[i] > \mathcal{R}^c \sum_{j=1}^{j=n} T_e[j] \qquad (2.10)$$

Here, $\mathcal{R}$ is a uniformly distributed random number between $[0, 1]$ and c is the cell selection weighting factor [Ewing and Berkowitz, 1998]. Please note that although $\mathcal{R}$ and $\mathcal{U}$ from Equation 2.5 are from the same distribution, their seed numbers and generator types are different. Hence I use different symbols here.

In the stochastic selection rule, c controls the strength of randomness, and its value lies in the range of $(0, \infty)$. When $c \to \infty$, the value of $\mathcal{R}^c \to 0$ for almost all values of $\mathcal{R}$. In this limit, the first block on the list of $T_{e,asc}$ (block with the lowest T_e value) will be invaded deterministically by gas. The resulting lightning-bolt-like gas finger is the same as the gas finger generated by Model 2. In fact, for $c \to \infty$, Model 4 becomes identical to Model 2. However, the lower the c value, the higher the RHS of Equation 2.10, which ensures that the higher $T_e[j]$ are picked more often; this generates gas fingers that are not moving strictly upward, but have a wider spatial distribution. Please note that the re-invasion of water events that result in fragmentation or mobilization of gas clusters are carried out exactly as in Model 2, i.e. without any stochastic modification.

Table 2.2 summarizes the model parameter values used in this thesis. The conceptual difference in the model versions is illustrated using a schematic in Figure 2.5. Figure 2.5**b** displays a gas invasion event in Model 1, which gives rise to a lightning-bolt-like gas finger. The fragmentation of the gas cluster owing to water re-invasion, as per Model 2, is shown in Figure 2.5**c**. Figure 2.5**d** shows the gas invasion of three blocks (three most favoured blocks according to T_e values) in the injection cluster following a fragmentation event, according to Model 3. Figure 2.5**e** displays the invasion of a

Table 2.2: Model parameter values used in this thesis.

Parameters [Units]	Symbols	Values
Common for models 1-4		
Density of water [kg/m^3]	ρ_w	1000
Acceleration due to gravity [m/s^2]	g	9.82
Average $P_t - P_e$ ratio [-]	α	0.6 Mumford et al. [2009]
Displacement pressure [cm of H_2O]	P_d	8.66 Schroth et al. [1996]
Pore-Size distribution index [-]	λ	5.57 Schroth et al. [1996]
Model domain size [mm^2]	$X - Z$	250×250
Block discretization [mm^2]	$x - z$	1×1
Model 3 specific		
Number of blocks to invade	nb	$\{1, 2, ...10, 15, 20\}$ for experiments at 10ml/min
		$\{1, 2, ...20, 25, 30, 35, 40, 50\}$ for experiments at 100ml/min and 250ml/min
Model 4 specific		
Cell selection weighting factor	c	$\{5, 10, 15, 200, 500\}$

randomly chosen neighbouring block (not the most favourable block according to the T_e values) following a fragmentation event according to Model 4.

2.4 Existing Methods of Comparison

After discussing the models and experiments used in this study, I present and discuss existing methods for comparing IP-type models to experimental data via imaging methods, i.e., perceptual comparison and spatial moments comparison, see Section 1.1.4.
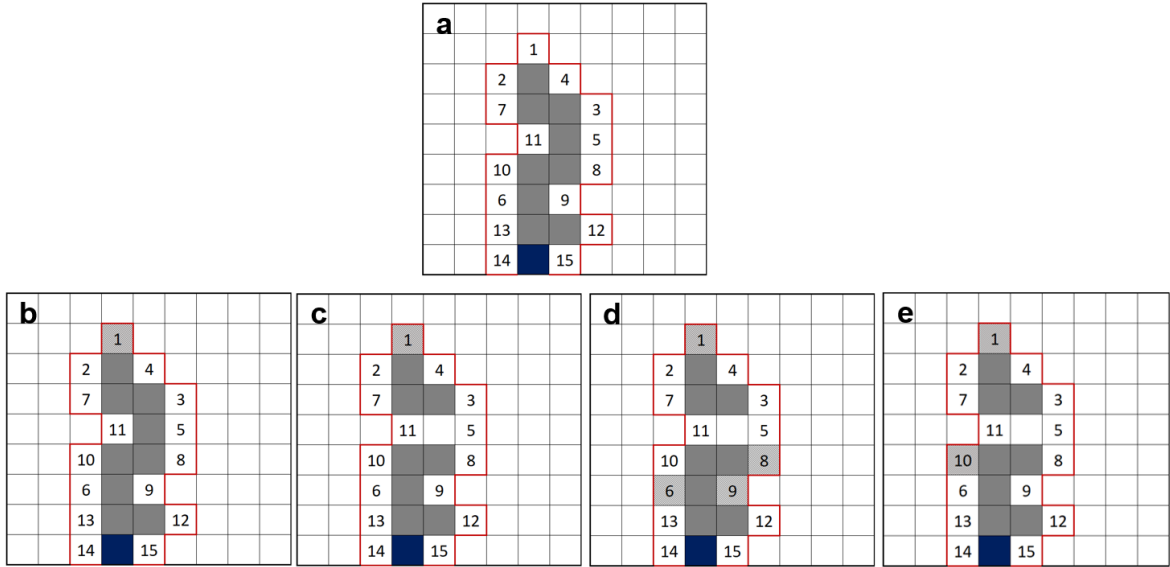
Figure 2.5: Illustration of the conceptual difference between the four model versions: **a** is an initial state of gas occupation in the domain; **b** displays gas filling in the next step according to Model 1; **c** displays fragmentation of gas cluster in the next step according to Model 2; **d** displays a fragmentation event followed by an invasion event with $nb = 3$ according to Model 3; **e** displays a fragmentation event followed by an invasion event according to Model 4. The numbers denote the increasing order of preference of gas invasion for the neighbouring blocks in the next step based only on T_e values. Light grey cells are the blocks chosen by the respective model version, and the blue block is the injection site.

2.4.1 Perceptual Comparison

Perceptual comparison is the method of visually comparing experimental data and model outputs for similarities. For example, Birovljev et al. [1991] compared the width of the fronts between the two phases from their experiments and IP simulations. In the work of Glass et al. [2001], the length of the gas clusters, pool height, as well as saturation distribution images from injection experiments and IP model results were perceptually compared. Trevisan et al. [2017] compared the experimental image against a combination of model realizations, indicating the probabilities of gas position. Molnar et al. [2019] visually compared the structure of gas fingers from their Macro-IP simulations to the experiments of Hegele and Mumford [2014].

This method's primary advantage is that no pixel-based information is lost from the highly resolved data because the images are visually compared on a pixel-to-pixel basis.

Also, multiple global attributes of an image (width of a finger, tortuosity, and so on) from simulation and experiment can be compared simultaneously. A valuable (but immeasurable) strength of the method is that it intuitively applies the user's expert knowledge to the judgement. However, the method of perceptual comparison is non-quantitative. Although it includes no computational effort, with the increase in the number of images to compare visually, the task may require an enormous effort from the user. Thus, it can become time-consuming, cumbersome, and non-objective.

Consider a situation where a user compares the breakthrough image (image when the invading phase has percolated across the entire defending phase saturated porous medium) from the experiment and an IP type model (e.g., Macro-IP) visually. Initially, the user compares only two images. Now, since IP-type models rely on stochastic simulation, the user runs 1,000 T_e realizations for the model to determine the near-accurate T_e field as in the experiment. The number of images to compare increases from two to 1,001. Next, for this Macro-IP model, the user wishes to calibrate model parameters like the saturation of the defending phase and porosity, and so decides to use saturation values and porosity values from 0 to 1 in increments of 0.1 excluding 0 and 1. Thus, for each entry pressure field for the model, the user runs the model 18 times to fit these two parameters. Now, the user has to compare 1.8×10^4 model images to 1 experimental image. The user is further interested in comparing various versions of the IP model (say four different versions as in this thesis), including the calibration of the two parameters mentioned above for each model version. Now, the user visually compares 7.2×10^4 model images against one experimental image. Worse still, the user intends to visually inspect all images from the time of injection until the breakthrough. One can realize: the effort of comparison amplifies extremely. In short, perceptual comparison can be too tedious and subjective for stochastic analysis and also where the experimental data is spatially and temporally intensive.

2.4.2 Comparison of Spatial Moments

Spatial moment methods have often been used to quantitatively describe both experimental data and numerical simulation output for multiphase flow in porous media [e.g., Essaid and Hess, 1993, Kueper and Gerhard, 1995, Jawitz et al., 2003, Pantazidou and Liu, 2008, Trevisan et al., 2015, González-Nicolás et al., 2017, to name just a few]. This

method was used to compare Macro-IP models and gas-injection experiments in the work of Mumford et al. [2015]. In a 2D water-saturated porous medium invaded by a gas phase, the method involves the calculation of zeroth ($\mathscr{M}_{00}$), first ($\mathscr{M}_{10}, \mathscr{M}_{01}$) and second moments ($\mathscr{M}_{20}, \mathscr{M}_{02}$) to describe the spatial distribution of the gas:

$$\mathscr{M}_{sp} = \int_{z=-\infty}^{\infty} \int_{x=-\infty}^{\infty} \phi \rho_g S_g\left(x, z\right) x^s z^p dx dz \tag{2.11}$$

Here, ϕ is the porosity, ρ_g is the density of the gas [kg/m³], S_g is the gas saturation value, x and z are horizontal and vertical dimensions [mm] in the 2D space. These moments represent the gas's mass, position and spread, respectively. Further, the centroid position of gas (X_c, Z_c) and its spatial extent as variance ($\sigma_{xx}^2, \sigma_{zz}^2$) are calculated from these moments:

$$X_c = \frac{\mathscr{M}_{10}}{\mathscr{M}_{00}} \qquad \sigma_{xx}^2 = \frac{\mathscr{M}_{20}}{\mathscr{M}_{00}} - X_c^2$$
$$Z_c = \frac{\mathscr{M}_{01}}{\mathscr{M}_{00}} \qquad \sigma_{zz}^2 = \frac{\mathscr{M}_{02}}{\mathscr{M}_{00}} - Z_c^2 \tag{2.12}$$

Theoretically, the spatial moments of experimental gas saturation data should be reproducible by the model simulation output. At least, the idea of matching spatial or temporal moments is a key concept in upscaling theories in heterogeneous porous media.

The method of spatial moments comparison is quantitative and objective. Also, it requires less time and human effort than the perceptual comparison method. This method's main disadvantage is the loss of information from the data (for images: pixel information) by the aggregation of a handful of summary statistics before comparison. This loss of information spoils chances for improved process understanding.

Also, in 2D space, one typically evaluates five spatial moment values, which individually comment on the quality of fit. However, there exists no standard method to combine the information from all of them in one unique metric to identify the best-fit realization. One reason for this is the difference in magnitude of the different spatial moment values. Moreover, for any arbitrary choice of combination of the spatial moment values,

the conclusions obtained would be ambiguous. For example, any combined-moment metric would produce the best possible value even for an exact mirrored copy of the experimental image (same first and second moments). When interested in predicting preferential flow pathways of a phase, identifying a mirrored image as the most realistic model output might be completely misleading. Due to this reason, the comparison of spatial moments does not enable any unique decision between competing models or in the calibration of models. In Section 3.3.2, I will further show how the loss of information of pixel data in the moments method can yield misleading results with the help of a case-study.

2.5 Bayesian Model Evidence

In Section 1.1.5, I presented the Bayesian Model Selection and highlighted the challenges of computing the Bayesian Model Evidence (BME). Here, I present the conventional mathematical formulation of BME, its computation using simple Monte Carlo (MC) integration, and Bayes factors. I use these definitions and equations in Chapter 5 to introduce, illustrate and test the Method of forced Probabilities for BME computation.

For N_m competing models $M_k, k = 1...N_m$ and observation data $\mathbf{y_0}$, the BME value BME_k of any model M_k can be evaluated as (Bayesian integral from Kass and Raftery [1995]):

$$
\begin{aligned}
BME_k &= p\left(\mathbf{y_0} \mid M_k\right) \\
&= \int_{U_k} p\left(\mathbf{y_0} \mid \mathbf{u_k}, M_k\right) \cdot p\left(\mathbf{u_k} \mid M_k\right) d\mathbf{u_k} \\
&\equiv I_k,
\end{aligned}
\tag{2.13}
$$

where U_k denotes the model's parameter space, and $\mathbf{u}_k$ represents a random parameter vector with prior distribution $p(\mathbf{u}_k \mid M_k)$, and $p\left(\mathbf{y}_0 \mid \mathbf{u}_k, M_k\right)$ is the probability or likelihood of the parameter set $\mathbf{u}_k$ of the model M_k to have generated the observed data set $\mathbf{y}_0$.

The integral I_k over the entire parameter space is computationally expensive and can become infeasible (with no meaningful BME value) in the cases discussed in Section 1.1.5. A review of methods to determine BME can be found in Schöniger et al. [2014].

To facilitate the introduction of the proposed method for computing BME in Chapter 5, I present here the approach of simple (or: brute-force) MC integration [Hammersley, 1960] of Eq. 2.13. The integrand is evaluated at randomly chosen points $(\mathbf{u}_{k,r})$ of the parameter space U_k, which are drawn from their prior distribution $p(\mathbf{u}_k \mid M_k)$. The mean of the evaluated likelihoods provides the approximate value of the integral (referred to as $\hat{I}_k$):

$$\hat{I}_k = \frac{1}{N} \sum_{r=1}^{N} p\left(\mathbf{y_0} \mid M_k, \mathbf{u}_{k,r}\right) \approx I_k, \tag{2.14}$$

with N being the number of MC realizations (ensemble size). To re-stress the problem: in applications with many precise data, the summands in this equation are (close to) zero with a probability very close to one, such that convergence can be prohibitively slow.

To rank models against each other, one can directly compare their BME values (the larger, the better) or their negative logarithmic BME values (the smaller, the better). Alternatively, one computes so-called Bayes factors (BF) [Kass and Raftery, 1995] for two models: $k = 1$ and $k = 2$:

$$\mathrm{BF}_{\frac{k=2}{k=1}} = \frac{BME_{k=2}}{BME_{k=1}}, \tag{2.15}$$

with a scale for interpretation provided by, e.g., Jeffreys [1961]. A BF value larger than one favours model 2 over 1, and the order of magnitude decides the statistical significance.

3 Model-to-Experiment Comparison method*

To fulfil the first research objective of this thesis, I develop a method of comparison between IP-type models and data. The first hurdle to overcome in this process is the absence of the time parameter in IP-type models. One needs to know *which* images of the experimental time-series and the model iterations to compare with each other. Thus, I suggest performing a volume-based time-matching (Section 3.1) between the experiments and the IP-type models as a first step. Then, in Section 3.2, I introduce the metric of comparison: the Jaccard coefficient and its diffused version. I apply my method to compare Model 2 (Section 2.3.4) with experimental data of gas injection at a rate of 0.1 ml/min (Experiment 0.1-A from Table 2.1). Further, I compare the performance of my method against the standard method of comparison by matching spatial moments (Section 2.4.2). In Section 3.3, I enlist the steps and present and discuss the results from this demonstration of my method. I summarize the results of the study and the conclusions obtained in Section 3.4.

3.1 Volume-Based Time Matching for IP-type Models

I use Equation 3.1 and Equation 3.2 to compute the gas volume in the experiment and the model, respectively.

$$V_{exp}(t = \Delta t \times n_t) = \sum_{n_t=1}^{n_t=N} Q_{exp} \times \Delta t \times n_t; \qquad n_t \in \mathbb{N}, n_t = 1, 2, 3, 4....N \qquad (3.1)$$

---

*This chapter contains text fragments and figures from my publication Banerjee et al. [2021]

Here, Q_{exp} is the rate of injection of gas in the experiment [m^3/s] and Δt is the time step in between the capture of two successive images [s] in the experiment.

$$V_{model}(\ell) = \sum_{\ell=1}^{\ell=L_{top}} n_{blocks} \times \phi \times S_g \times V_{block}; \qquad \ell = 1, 2, 3, ... L_{top} \qquad (3.2)$$

Here, $n_{blocks}(\ell)$ is the number of blocks invaded per loop counter ℓ in the Model 2 described in Section 2.3.4, L_{top} is the model loop counter when the gas reaches the top of the domain, and V_{block} is the volume of each discretized block of Model 2 (see Table 2.2). The porosity ϕ of the sand used in the experiment is assumed to be uniform, and S_g is the gas saturation value assigned to the entire gas cluster.

After that, for all the time-wise elements in the V_{exp} and V_{model} data vectors, the Euclidean distance is computed. Based on this distance value, each element of the V_{exp} vector gets a nearest neighbouring element (minimum Euclidean distance) in the V_{model} vector. For all those nearest-neighbour pairs, I assign the experimental time t to the corresponding model loop counter ℓ. One may now compare the respective time-matched images based on my proposed (*Diffused*) *Jaccard coefficient* (Section 3.2). In my specific implementation, I use the MATLAB inbuilt function *knnsearch* with the *exhaustive* search algorithm to efficiently conduct the nearest neighbour search.

The model loop counter may increase without an increase in volume because of a fragmentation process. A fragmentation process refers to a combination of an imbibition (of water) step and an invasion (of gas) step. This process does not add gas to the system but is actually a re-arrangement of the gas-occupied blocks (see Section 2.3.4). In such a situation, all these model loop counters will match the same single experimental time (because each experimental image by definition shows an increase in volume due to the fixed gas injection rate Q_{exp}). I recommend assigning the experimental time to the last matching model loop counter in that case because this model state represents the completed processes at the matched volume.

3.2 Proposed Metric of Comparison: (Diffused) Jaccard Coefficient

To quantify the similarity between experimental and simulated images, I compute the Jaccard coefficient (J) [Tan et al., 2005]. This metric is widely used in the context of object identification or image recognition. Per set theory, it is defined as the size of the intersection between two sets, A and B, divided by the size of the union of these sets.

$$J(A, B) = \frac{|A \cap B|}{|A \cup B|} \tag{3.3}$$

The Jaccard coefficient ranges between zero and one, with zero meaning no similarity and one meaning complete similarity. To understand how I compute the Jaccard coefficient for binary (black/white) images, consider Figure 3.1 (top row) as a schematic illustration of the intersection between the binary-colour coded (coloured block = 1, white block = 0) data sets *experimental image* (Figure 3.1a) and *model image* (Figure 3.1b). The intersected blocks ($|A \cap B|$) are colored purple (Figure 3.1c). I count the number of purple blocks and divide by the total number of coloured blocks ($|A \cup B|$) in the images of Figure 3.1a and 3.1b without double counting the pixels that agree to be coloured in both of them (purple blocks of Figure 3.1c), to compute the Jaccard coefficient. One can automate this to be calculated for a time-series of images.

A pixel-by-pixel comparison would reject even a perfect model in a scenario where the point of gas injection in the experiment is not precisely known, leading to an offset between the experiment and the model. In many real-world applications, this offset would be of no concern; on the contrary, one would wish to identify such a perfect model run. Thus to identify such "perfect" model runs, I blur the images from both the experiment and the model before computing the Jaccard coefficient. Since the blurring produces non-binary values, I use a slightly adapted implementation of the Jaccard coefficient for sets $A = \{a_i : a \in \mathbb{R}, i = 1, 2, ...n\}$ and $B = \{b_i : b \in \mathbb{R}, i = 1, 2, ...n\}$, which is also known as the Ruzicka similarity coefficient [Deza and Deza, 2016]:

$$J_d(A, B) = \frac{\sum_i^n \min(a_i, b_i)}{\sum_i^n \max(a_i, b_i)} \tag{3.4}$$

I call this metric J_d the *Diffused Jaccard coefficient* and illustrate its evaluation in the bottom row of Figure 3.1.
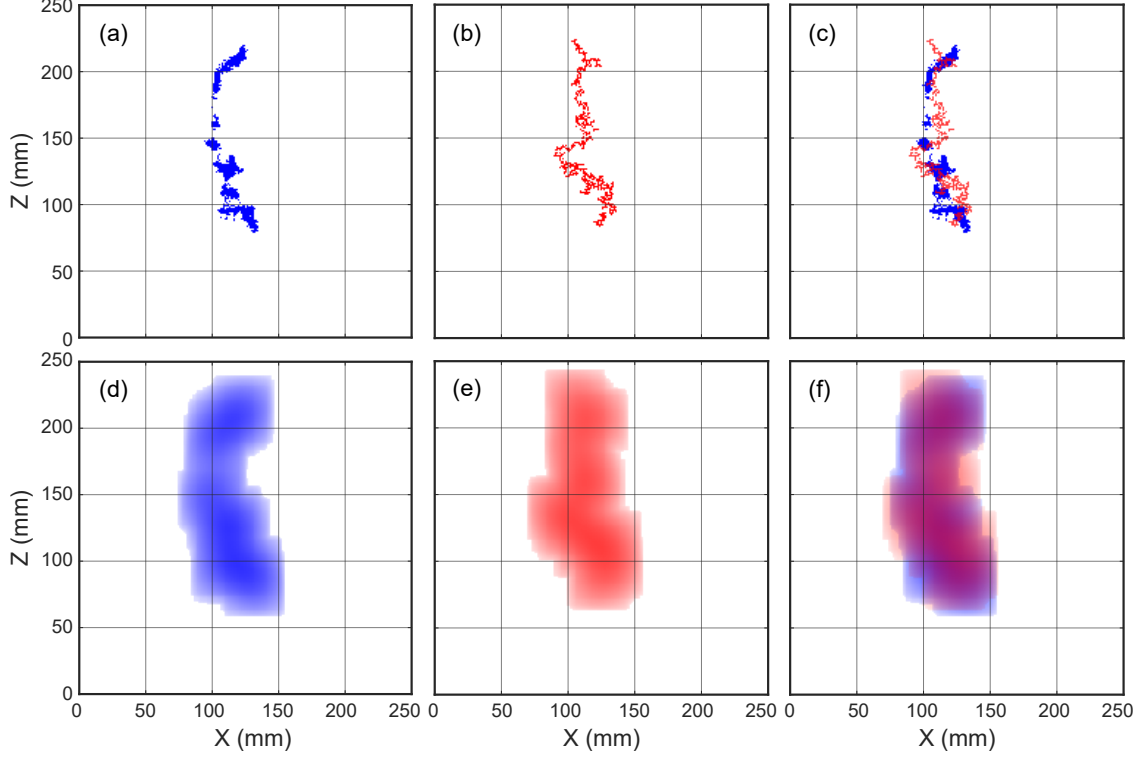

Figure 3.1: Visualization of intersection evaluated in the (Diffused) Jaccard coefficient through exemplary images. (a) Image from experiment 0.1-A at the end of the experiment ; (b) Corresponding time-matched Model 2 realization; (c) intersection of images (purple) evaluated by Jaccard coefficient (here: $J = 0.12$); (d) and (e) corresponding blurred experimental and model images (4% domain size blur radius); (f) intersection of blurred images (purple) evaluated by Diffused Jaccard coefficient (here: $J_d = 0.54$).

To blur the images, I use the 2D-Gaussian blur function:

$$G(x, z) = \frac{1}{2\pi\sigma^2} e^{-\frac{x^2 + z^2}{2\sigma^2}} \tag{3.5}$$

Mathematically, the blurred images are produced by convolution with a Gaussian kernel of specified width (standard deviation σ). Hence, the blurring radius is increased or decreased by altering the σ value in Equation 3.5. I use the kernel size relative to the original domain size as a unit for the images' blur radius. The blurring results in non-binary images (see Figures 3.1d - 3.1f) with values between 0 and 1. These represent a

spatial tolerance in matching and do not refer to intermediate gas saturation values.

3.3 Method Demonstration: Case-Study

In this section, I present a demonstration of my comparison method (Sections 3.1 and 3.2) using the data from experiment 0.1-A, i.e. from the experiment conducted at a gas-injection rate of 0.1ml/min and Model 2 (Section 2.3.4).

The parameter values from Table 2.2 are used for Model 2. I run the model 1,000 times, each run differing in the random spatial arrangement of the P_e values, thus also differing in the spatial arrangement of P_t values. These model runs represent the uncertainty in these parameter values, which are impossible to determine with experimentation. For each of these 1,000 model runs, the simulation ends when the gas reaches any block on the top of the model domain.

Additionally, in this case-study, I assume a constant gas saturation value (S_g) of 0.2, based on Van De Ven et al. [2020], for all the gas clusters [Mumford et al., 2015]. This approach may not be an accurate representation of reality. However, this assumption helps to retain the model's simplicity and hence reduces its computational cost, and this assumption does not affect the discussion of my comparison method.

3.3.1 Steps of the Model-Experiment-Comparison

First, I conduct the experiment-to-model time matching (discussed in Section 3.1) using Equations 3.1 and 3.2. The model simulation starts from the time gas first percolates into the water-saturated sand in the experiment. Then, I compute the Jaccard coefficient between the time-series of experimental images and the corresponding model images across all the model realizations. Also, I compute the Diffused Jaccard coefficient using radii of blurring ranging from 0% to 50% of the domain size in steps of 1% by changing the standard deviation value (see Equation 3.5).

For comparing my method to the existing method of spatial moments, I calculate the difference between centroid and variance values (Section 2.4.2) of the final experimental image and of the corresponding time-matched model output images. I normalize this

difference by the centroid and variance values of the experimental image and then identify the minimum of the normalized differences of each of the centroid and variance values in the X - Z axes. Comparing zeroth moments M_{00} is unnecessary because the time matching is based on volume matching, so M_{00} is always accurate.

Additional to the model images, I also translate an experimental image in the X - Z space to compare with the original experimental image. This facilitates additional discussions for my method. On this image, too, I calculate the Jaccard coefficient, the Diffused Jaccard coefficient and the spatial moments.

I segregate the discussion of the results of this case-study into two separate sections, for ease of understanding. In Section 3.3.2, I discuss results based on the experimental image at the end of the experiment and corresponding time-matched images of all model realizations. In Section 3.3.3, I focus on using the proposed metric on the time-series of the time-matched images from the experiment and model.

3.3.2 Results from Comparison Based on Final Experimental Image

One can compute the (Diffused) Jaccard coefficient for any of the time-matched images of the experimental data time-series. Here, I begin the discussion by picking the experimental image at the end of the experiment (at $t_{end} = 330$s) and the corresponding time-matched model image per model realization for clarity. The quality-of-fit (no matter if assessed perceptually, by spatial moments or by the proposed metric) varies significantly across the 1,000 model realizations. For example, the values for J vary between 0.003 and 0.17, and those of J_d vary between 0.01 and 0.79. Therefore, I select a set of model realizations for discussion that show a reasonable agreement with the experimental image. I will motivate the choice of individual realizations further below.

Spatial Moments Can Be Misleading

First, I compare the spatial moments of seven arbitrary (time-matched) images to the final experimental image (Figure 3.2). By comparing the height of the grey bars (model realizations) against the height of the solid dark blue bars (experimental data) in Figure 3.2, one can see that none of the six model realizations clearly outperforms the others in all spatial moments; rather, performance varies significantly across the four measures.

Indeed, I have chosen four of the realizations (numbers 3, 4, 5, and 6) to exactly match X_c, Z_c, σ_{xx}^2 and σ_{zz}^2, respectively (see Figure 3.2). Recall that all of the time-matched realizations by definition match the zeroth moment, which is equivalent to the volume in the domain. Table 3.1 lists the characteristics of the seven realizations chosen for detailed analysis and discussion here.
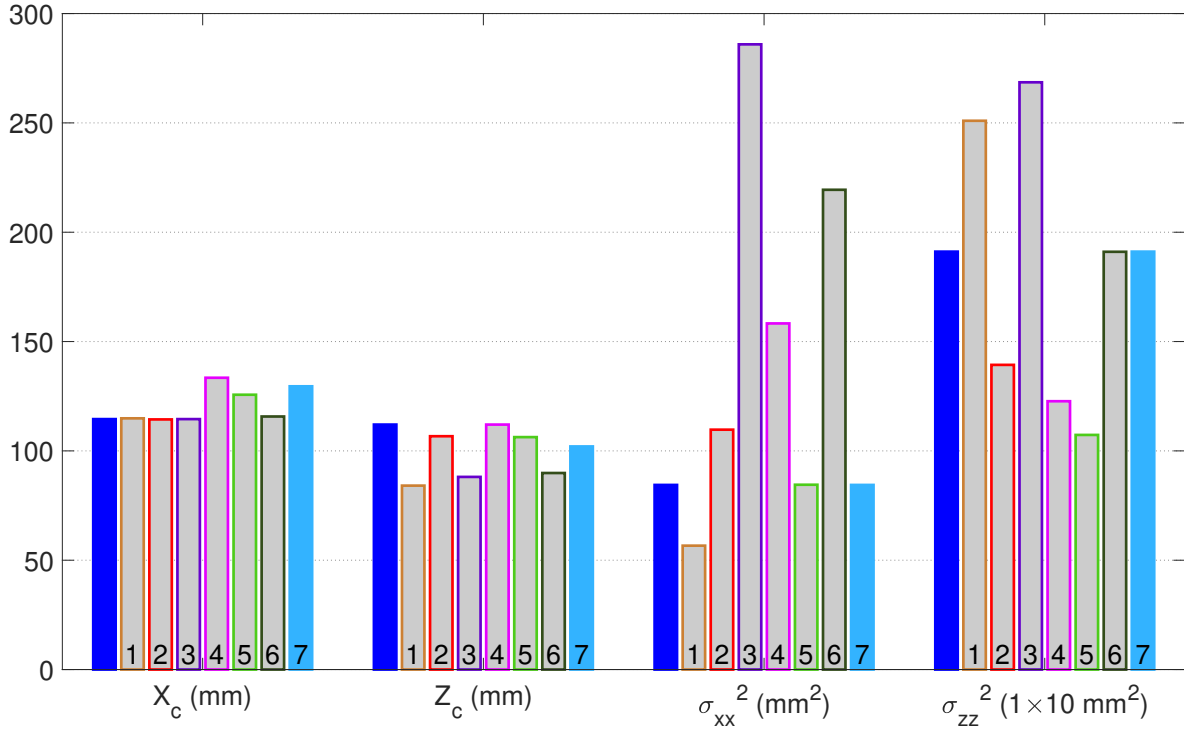

Figure 3.2: Bar chart of spatial moments in X-Z space (computed using Equation 2.12) for experimental image and its shifted copy (solid blue bars) and model realizations (grey bars) as listed in Table 3.1; numbers in the bars denote respective realization number.

The final model images of these realizations are visually displayed in Figure 3.3. Realization 7 in Figure 3.3h might look familiar to the reader – it is, in fact, the original experimental image, but translated 15 mm to the right and 10 mm upwards in X-Z space. This realization represents a typical situation where the actual injection point is not precisely known. Consistently, this realization meets the second spatial moments (spread) in X and Z but fails in reproducing the exact position of the gas (first moments). Hence, if one relied on a spatial moments comparison, one might fail in identifying this realization as an (almost) perfect fit. In real applications, identification of this realization as the true one is essential because it would deduce that the model used is, in fact, correct, but only the injection point is assumed at the wrong position.

Table 3.1: Characteristics of the seven realizations selected for detailed analysis along with their ranking obtained from their Jaccard coefficient (J) and Diffused Jaccard coefficient (J_d) values at 4 % of domain size blur radius. The individual spatial moment values for the realizations can be read from Figure 3.2. The values for J are provided in Figure 3.3, and those for J_d are provided in Figure 3.6.

Realization Number	Description	Rank by J	Rank by J_d
1	Model realization with maximum Jaccard coefficient value for final image	1	2
2	Model realization with the fastest increase of diffused Jaccard coefficient with an increase in blurring radius	2	1
3	Model realization with the minimum normalized difference to the experimental centroid in X direction for final image	6	4
4	Model realization with the minimum normalized difference to the experimental centroid in Z direction for final image	4	7
5	Model realization with the minimum normalized difference to the experimental variance in X direction for final image	5	6
6	Model realization with the minimum normalized difference to the experimental variance in Z direction for final image	3	3
7	Experimental image translated in X-Z space ("shifted copy of experimental image")	7	5

One cannot afford to *not* detect a perfect model realization. Therefore, I strongly recommend using the proposed (Diffused) Jaccard coefficient as a metric of comparison, as discussed in the following sections.

Jaccard Coefficient Yields More Conclusive Ranking

Realization 1 is chosen as the realization that has scored the best Jaccard coefficient (see Table 3.1). When assessed through the eyes of spatial moments, this realization does not look especially convincing (the grey bar for Realization 1 is of the same height as the solid dark blue experimental bar for X_c, but shorter for Z_c and σ_{xx}^2 and taller for σ_{zz}^2 in Figure 3.2). However, from Figure 3.3b, one can see that, perceptually, it does
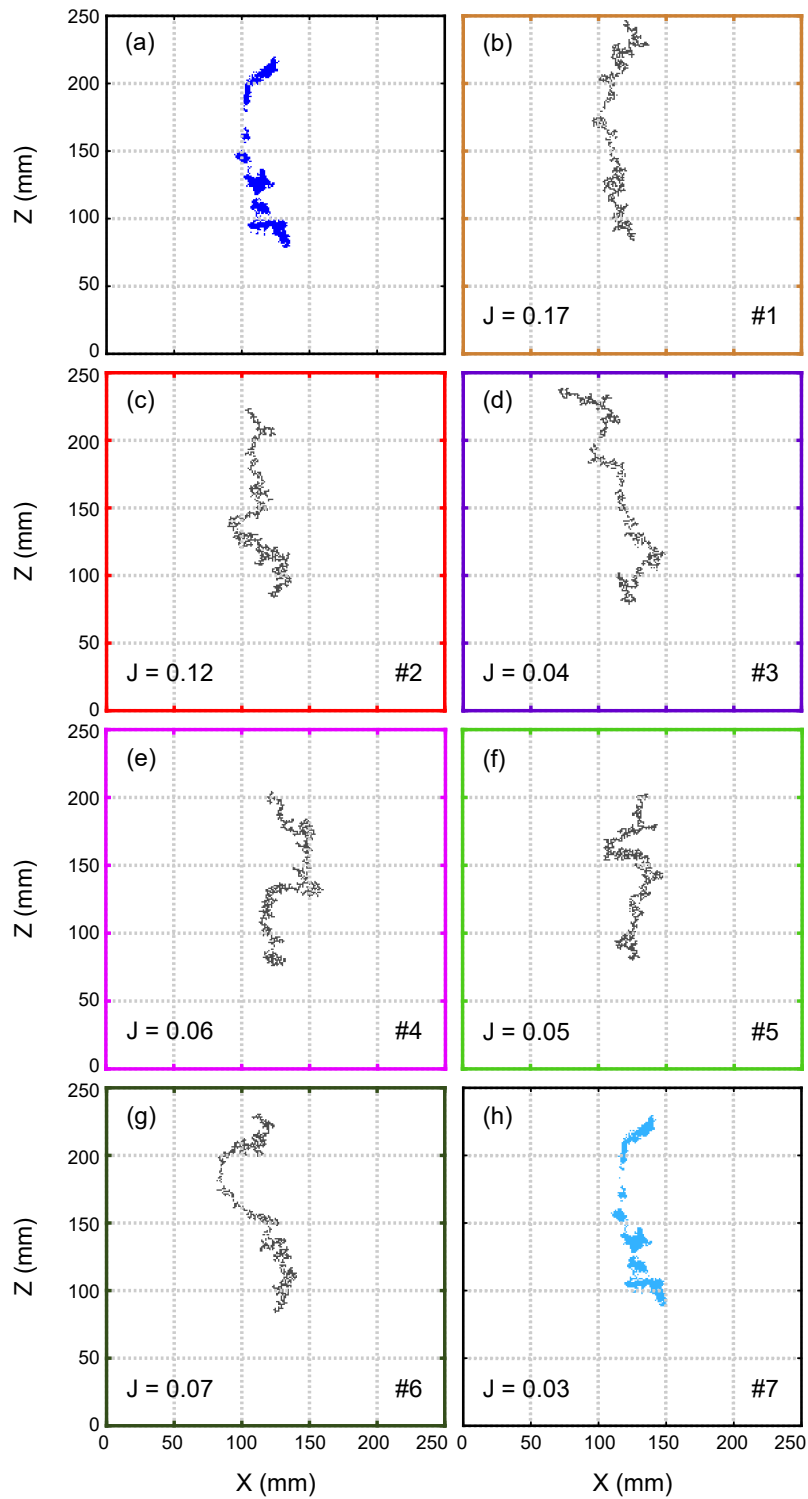
Figure 3.3: Images at the end of the experiment as a basis for perceptual comparison. (a) Final experimental image; (b - g) time-matched model realizations and (h) shifted copy of the experimental image as listed in Table 3.1, with box colours and numbers in figures representing the respective realization.

achieve a good fit, which confirms that comparison on a pixel-to-pixel basis as done with the Jaccard coefficient yields more conclusive results than the spatially-aggregated moments' method. I observe that the gas finger of Realization 1 with the highest J value extends farther to the top than the original experimental image (Figure 3.3a). This is not a systematic result, but this particular randomized entry pressure field yielded the highest pixel-by-pixel agreement with the experimental image. Suppose the distance of the gas finger to the top of the glass cell was of particular interest to the modeller. In that case, one could modify the Jaccard coefficient calculation such that it only compares, e.g., the blocks of the outer gas finger boundary.

Realizations 3 – 6 (Figure 3.3d to 3.3g) have a poor perceptual fit to the experimental image, and this is reflected in their Jaccard coefficient values. However, a combination of spatial moments of these realizations cannot lead us to this conclusion. For example, in Figure 3.2, compared to the height of the experimental dark blue bars, the height of Realization 3 grey bars vary slightly for the Z_c value but highly for σ_{xx}^2 and σ_{zz}^2 values. Simultaneously, the height of Realization 5 grey bars vary slightly for X_c and Z_c values but highly for the σ_{zz}^2 value. Thus, when one compares the height of the grey bars for Realizations 3 - 6 to the height of the dark blue experimental bars in Figure 3.2, it is not possible to identify any pattern in their variations. In contrast, the Jaccard coefficient provides a single value and a clear, precise ranking of the realizations.

Yet, observe that Realization 7 has a very low J value of 0.03, although it is just a translation of the original experimental image. Therefore, I recommend using the diffused version of the Jaccard coefficient (J_d) (see next Section).

Diffused Jaccard Coefficient Provides Most Insightful Ranking

I have already schematically illustrated the evaluation of the Diffused Jaccard coefficient with Figure 3.1 in Section 3.2. In fact, the experimental image shown in Figure 3.1 corresponds to the final experimental image (Figure 3.3a), and the shown model realization corresponds to Realization 2 (Figure 3.3c) from Table 3.1. When the images are blurred as in Figure 3.1d and 3.1e (here, with 4% domain size blurring), their similarity (using J_d) is compared on a scale larger than that of the individual pixels.

Figure 3.4 summarizes the performance of the seven realizations of Table 3.1 as a function of the Gaussian blur radius varied from a detailed pixel level of 0% of the

domain size (non-diffused Jaccard coefficient value) to a very summarized level of 50% of the domain size.
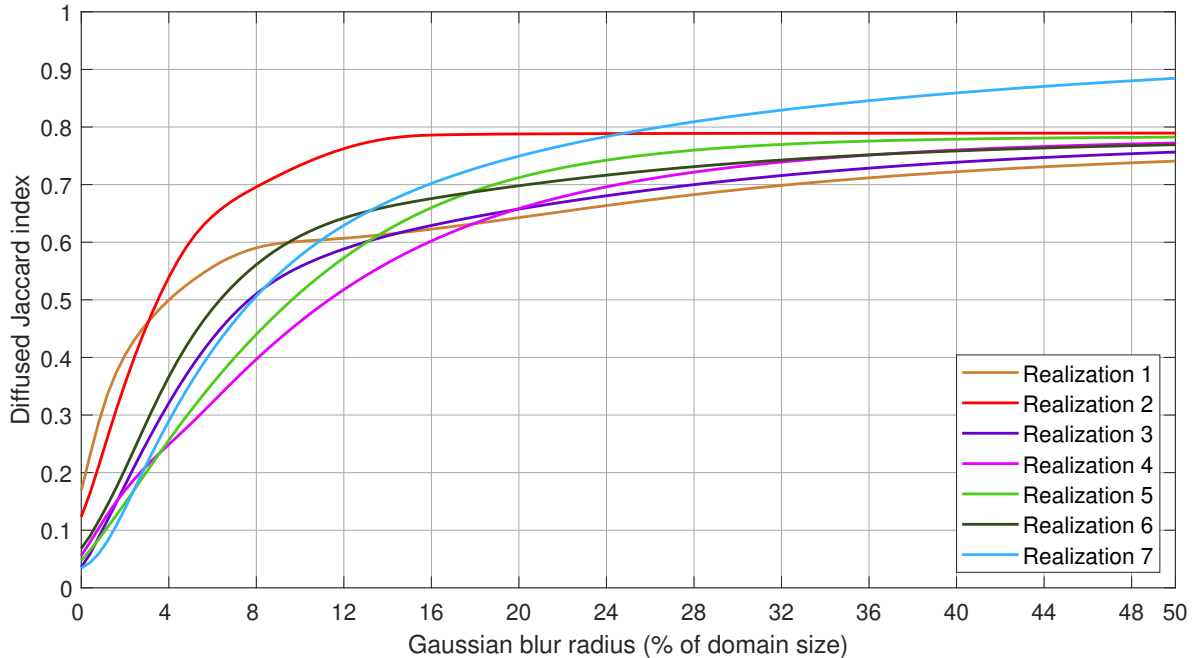

Figure 3.4: Diffused Jaccard coefficient as a function of Gaussian blur radius for the realizations listed in Table 3.1

In Figure 3.4, upon increasing the blurring radius, the J_d values for the shifted copy of the experimental image (Realization 7) keep increasing and go up to 0.9 (cyan blue plot line). Thus, the problem with using the Jaccard coefficient mentioned in the previous section for realization 7 is resolved using the Diffused Jaccard coefficient. So, for cases like the shifted copy of the experimental image, while spatial moments lead to inconclusive results and the non-diffused Jaccard coefficient evaluates it as a poor fit, the use of the Diffused Jaccard coefficient is a safer choice. Also, I picked Realization 2 (see Table 3.1) for having the steepest increase of J_d values upon increasing blur radius in Figure 3.4 and it is observed to be a good perceptual match to the experimental image (see Figure 3.3c). Recall that Figure 3.1 shows the intersection of Realization 2 with the experimental image in a blurred and non-blurred state. Indeed both realizations look very similar "in nature", although the pixel-by-pixel comparison would not see that because they differ slightly in position and tortuosity.

Further, note that in Figure 3.4, the J_d values of realizations 3 - 6 do not improve as fast as those of Realizations 1 and 2 with increased blurring. This slower rate of increase

implies that the Diffused Jaccard metric does not favour perceptually different realizations as much as it favours realizations with small offsets to the original experimental image. To further demonstrate that blurring does not favour all realizations equally, I show seven arbitrary model realizations at a blur radius of 4% of the domain size in Figure 3.5. At this blur radius, the value of J_d amongst the $1,000$ model realization images varies between 0.05 and 0.54. From Figure 3.5, it is evident that blurring does fade out the information in the pixels; however, for a given blur radius, differences between good and bad realizations are revealed reliably.
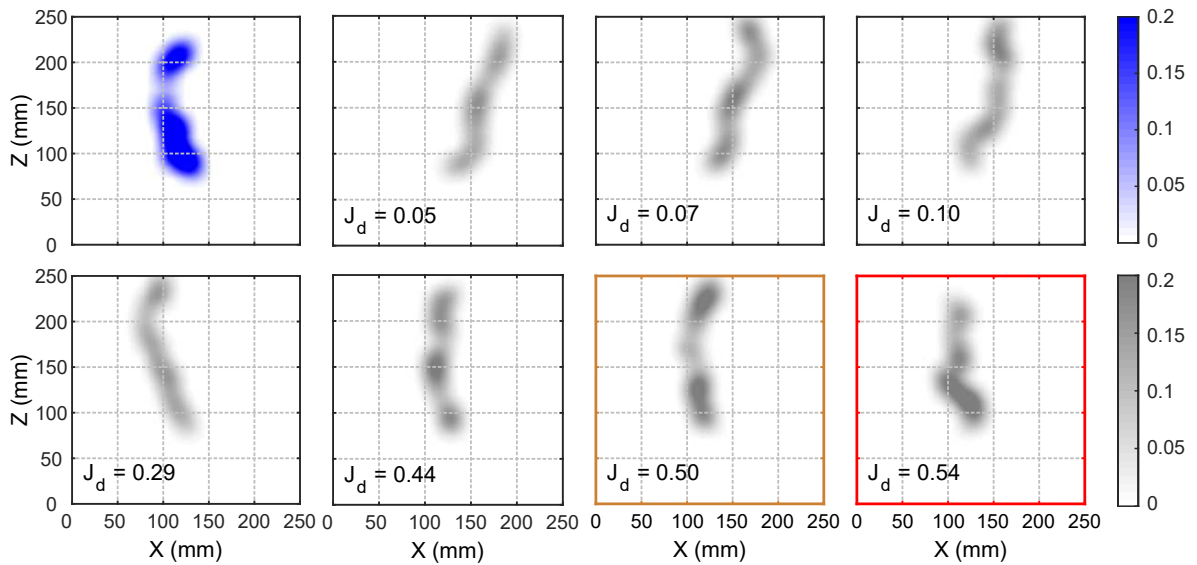
Figure 3.5: A set of arbitrarily selected model realizations along with the experimental image to present the range of the Diffused Jaccard coefficient J_d at 4% of the domain size blur radius; the model realizations in mustard yellow box and red box are Realization 1 and Realization 2 from Table 3.1, respectively.

To investigate to what extent one can blur the images for a meaningful comparison, I show the selected seven realizations from Table 3.1 along with the experimental image at different blur radii in Figure 3.6. It is evident from this figure that the images lose more and more pixel details with increasing blur radius. Note that, at blur radius values of 20% and 40% of domain size, the images from the experiment and Realizations 1 - 7 look almost the same. This explains why the J_d values of the different realizations do not improve significantly after approximately 20% of domain size blur radius in Figure 3.4. Thus, the upper limit of the blur radius would depend on the application for which the experiments and modelling are done. However, in general, it seems safe to say that any radius of blurring exceeding 50% of the domain size is questionable.
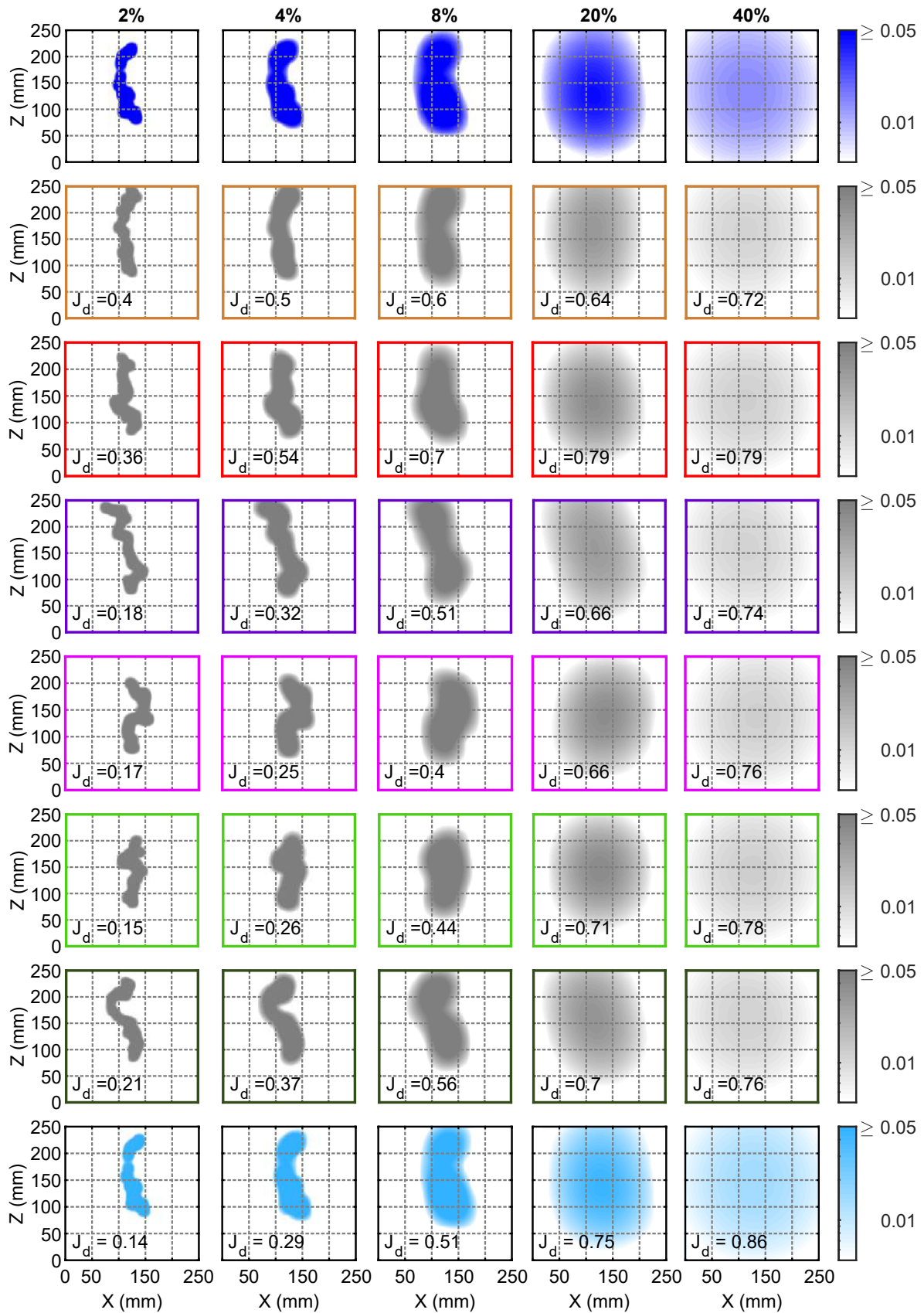
Figure 3.6: Experimental image and corresponding realization images (from top row to bottom row: Realizations 1 – 7 of Table 3.1) with blur radius values of $2\%, 4\%, 8\%, 20\%$ and 40% of the domain size in logarithmic color-scale. Box colours represent respective realizations; cyan blue pixels are used for the shifted copy of the experimental image (Realization 7).

3.3.3 Results from Comparison Based On Experimental Time-Series

This section explores the possibility of computing the (Diffused) Jaccard coefficient for the time-series of time-matched images. Figure 3.7 summarizes the achieved diffused Jaccard values J_d of the six model realizations of Table 3.1 as a function of experimental time at a blur radius of 4% of the domain size. This plot helps evaluate the model performance over the entire process of evolution of the gas finger instead of only assessing the final gas finger at the end of the experiment. I refrain from computing the spatial moments over time because that would yield four time-series per model realization; without a standardised procedure to combine them into a single meaningful measure for model realization ranking. Remember that Realization 7 is just the final experimental image shifted in space, so I leave out its temporal evolution here.
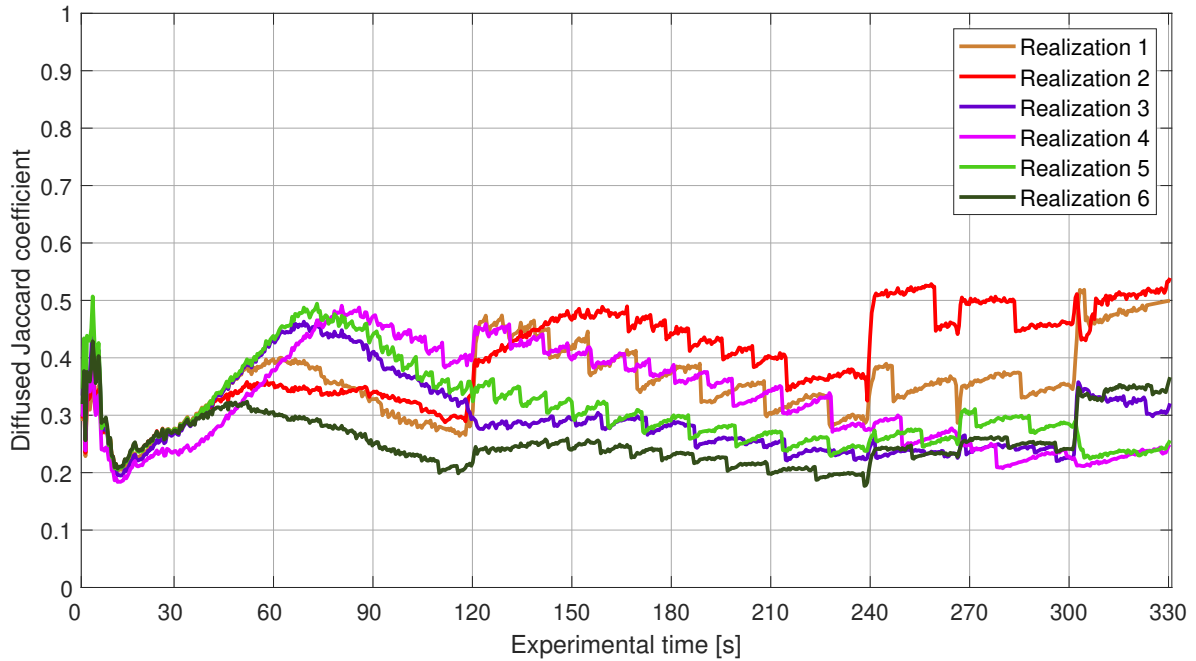
Figure 3.7: Diffused Jaccard coefficient (J_d) over all time-matched images with a blur radius of 4% of the domain size, for model Realizations 1 – 6 from Table 3.1.

All the time-series plotted in Figure 3.7 show some common trends. As examples, I pick two instances of time for further investigation. First, the value of J_d for all realizations drops at a time of around 15s. Second, all the realizations show an abrupt increase at around 240s.
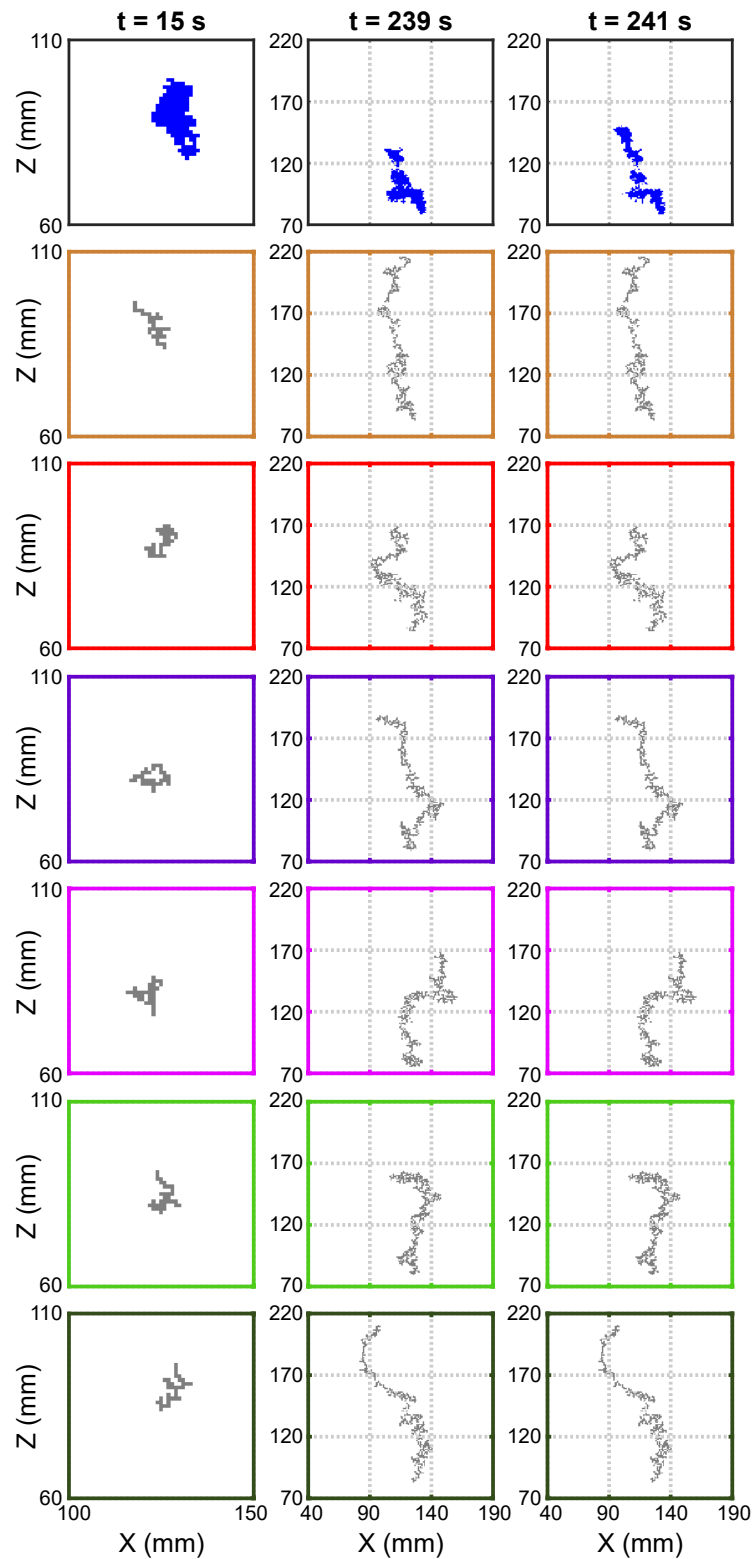
Figure 3.8: Zoomed images at specific times per column (axis limits are different for each column). From top row to bottom row: experimental images and images of model realization 1 – 6 from Table 3.1; box colours represent respective realizations.

When zooming into the gas cluster at 15s (column 1 of Figure 3.8), observe that the experiment's gas cluster has far more gas-occupied blocks than the corresponding model realizations. This is why, even upon blurring, the J_d value decreases. The smaller number of gas-occupied blocks in the model images can be due to an overestimation in the gas saturation value used for volume-based time matching (Section 3.1). Alternatively, the higher number of gas-occupied blocks in the experimental image can be due to noisy pixels wrongly identified as gas-occupied pixels.

To investigate the abrupt rise in the J_d value at around 240s, I zoom into the gas finger images at time 239s and 241s in the second and third column of Figure 3.8, respectively. At both times, when I compare the experimental finger to the model fingers, perceptually, they are different. But note that the experimental image (dark blue gas finger) at 239s, with more gas accumulated towards the bottom, is much shorter in height than at 241s. The model tends to expand towards the top, as is seen in all the model realization images of columns 2 and 3 of Figure 3.8. So, when the gas finger in the experimental image at 241s suddenly moves up, the J_d value increases abruptly for all the model realizations. Note here that the increase in J_d value at around 240s is not the same across all model realizations in Figure 3.7. Realization 2 (third row, red box in Figure 3.8) has the closest resemblance to the experimental image at 241s. Accordingly, the maximum increase in J_d value is seen for Realization 2 (red plot line) in Figure 3.7.

On the one hand, looking at the temporal evolution of J_d for specific realizations could help us improve the model structure (identify "wrong decisions", common errors to all realizations, and so on). On the other hand, the experimental team can use this temporal evolution of J_d as a diagnostic tool to detect unexpected or exceptional behaviour in the experimental data set. Such behaviour detection could help them identify and resolve problems with experimental setup conditions or data-processing techniques.

3.4 Summary and Conclusions

The proposed volume-based time-matching method enables comparing of IP-type models with no sense of real-world time to real-time experimental data. Perceptual comparison takes into account the expert intuition about the quality-of-fit, but it becomes an

impossible task for a large number of realizations (and potentially even timesteps) that one would like to investigate. To avoid subjective and tedious perceptual comparison of images, I propose to compute the Jaccard coefficient as a quantitative, automated and therefore objective metric for comparison.

From the case-study results, it is evident that spatial moments are hard to aggregate into a single meaningful measure; they are inconclusive and can even be misleading. They would be a poor choice for time-series evaluations. The Jaccard coefficient quantifies pixel-by-pixel agreement and is hence close to a "measure of perception", but it evaluates the perfect-but-shifted model realization only as mediocre. The Diffused Jaccard coefficient solves this problem: with increasing blur radius, this shifted model realization image emerges as the best one.

The blur radius can be visualized as a switch that helps the user control the extent of details to be retained in the images. So, the most meaningful blur radius for a specific application has to be decided by the user; it can reflect the intended purpose of identification. For example, suppose the user wants to know the radius of a gas contamination zone in the subsurface to protect the groundwater table. In that case, the images can have a relatively high blur radius. I recommend to try increasing blur radii to observe such effects as shown here synthetically with the translated experimental image and then decide its value. Also, I recommend always reporting Diffused Jaccard coefficient values together with their blur radius (with an appropriate unit; in the case-study I used the percentage of the domain size) for transparency.

4 Model Selection of Competing Models*

Traditional IP-type models, at any scale, do not incorporate viscous effects and have, therefore, not been tested before in gas flow regimes other than discontinuous flow (slow injection of gas). That means model testing for the transitional and continuous gas flow regimes (Section 2.1) remains an open question. This is because, at higher gas-injection rates, ignoring viscous effects near the gas injection point as in traditional IP models is not a valid assumption (see Section 2.2). However, the addition of several rules to IP models makes them potential candidates for transitional or continuous flow regimes. For example, modifications of macroscopic-IP models, such as presented in Model 3 (Section 2.3.5) and Model 4 (Section 2.3.6), are capable of simulating the mentioned viscous effects.

Many IP-type models exist, but very few of them have been compared to actual data (Section 1.1.2) due to challenges discussed in Sections 1.1.4 — 1.1.5. In Chapter 3, I presented a quantitative comparison method between IP-type models and laboratory gas-injection data and tested it using an experiment from the discontinuous flow regime. In this chapter, I use this method to assess the performance of the four macroscopic-IP models (Sections 2.3.3 — 2.3.6) in the continuous and transitional flow regimes (experimental triplicate at 10 ml/min, 100 ml/min, and 250 ml/min, from Section 2.2), which helps derive the direction for further model refinement.

The final-time images for the nine experiments used in this study are shown in Figure 4.1. Note, for experimental triplicates at an injection rate of 10ml/min (first row of Figure 4.1), the gas finger of 10-B moves towards the side of the domain, instead of being centrally aligned like in 10-A and 10-C. Also, for experiment 100-A (second row

---

*This chapter contains text fragments and figures from Banerjee et al.

of Figure 4.1), the multiple gas fingers are quite spread out, but those in 100-C merge to produce thicker fingers along the way (second row of Figure 4.1). These differences in the images support the uniqueness of each experimental outcome owing to the re-packing of the sand (see Section 2.2).

Globally, this requires answering $RQ2$ posed in the introduction of this dissertation (Section 1.2.2):

"Using the comparison approach developed in research question 1 on the different macroscopic IP model versions, how to determine which model version is better at describing which of these gas-flow regime experiments? Can specific deficits and recommendations be derived?"

In this chapter, I expand $RQ2$ into the following sub-research questions:

1. Can any of these four models be used for simulating gas flow in the continuous or transitional flow regimes?

2. If yes, which ones are more suitable?

3. What can one learn from the comparison of more or less successful model strategies and their remaining weaknesses to derive recommendations for future modelling efforts?

I begin by discussing the implementation of the comparison method (from Chapter 3) for the inter-comparison of the models in Section 4.1. As metrics for ranking the models, I use both the Jaccard and Diffused Jaccard coefficients. Note from Section 3.2 that a value for the blur radius has to be chosen to compute the Diffused Jaccard coefficient. Here, I choose three different levels of blurring (three blur-radii), which are discussed in Section 4.2. I report the results from this implementation and provide insights about the models' performance and their parameters in Section 4.3. Finally, I summarize the conclusions of this study in Section 4.4.

4.1 Steps of Model Comparison Study

I present an overview of the model-comparison setup in Figure 4.2.
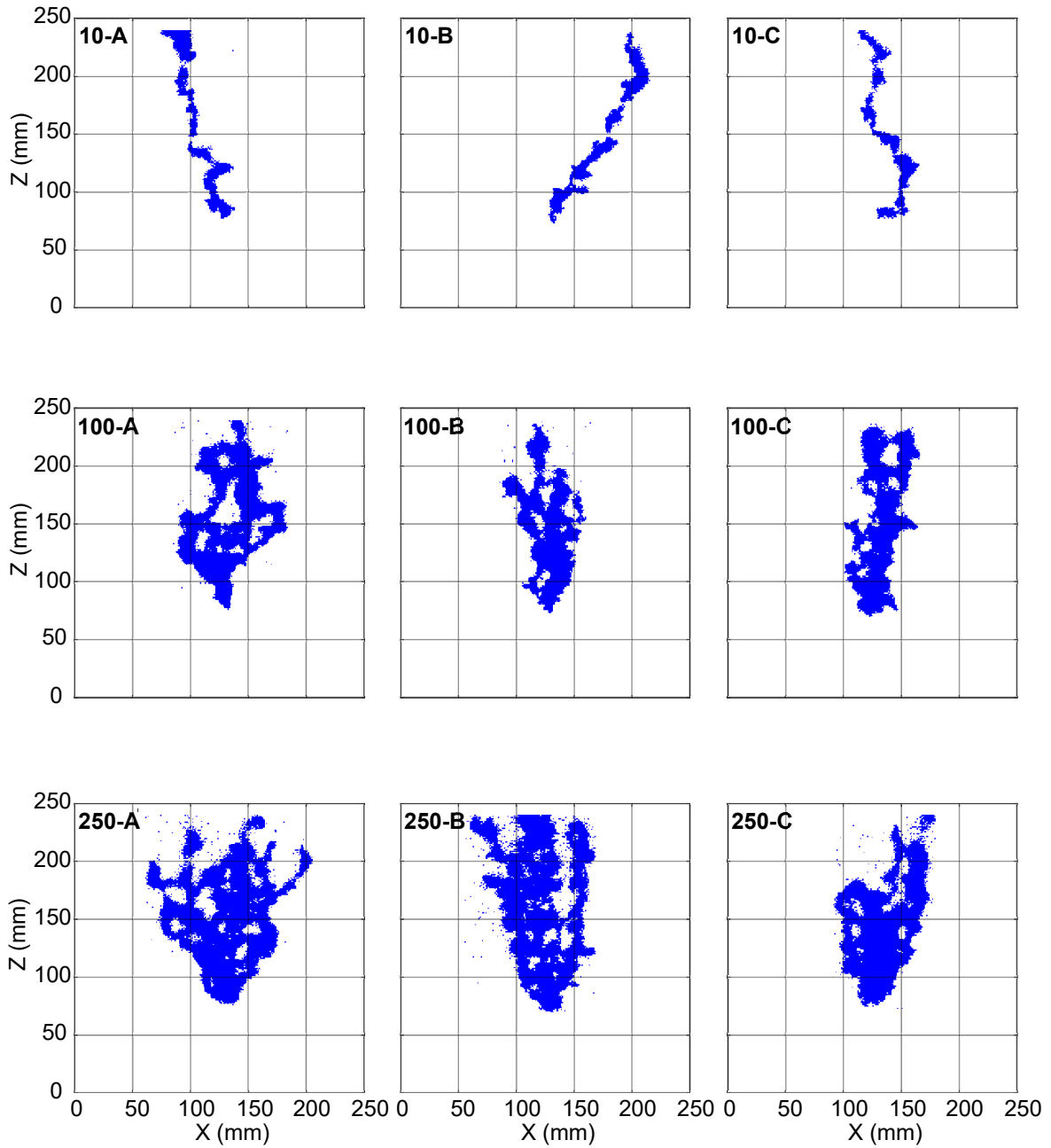
Figure 4.1: Final time binary experimental images for experiments 10-A, 10-B, 10-C, 100-A, 100-B, 100-C, 250-A, 250-B, 250-C. These gas presence/absence images are not free from pixel noise. Zones of the images where too many noisy pixels aggregate have been cleaned prior to use in this study.

In step ②, I run the four models over several (500) invasion threshold (T_e) realizations for all four models of Sections 2.3.3-2.3.6 (including the sub-versions discussed below)
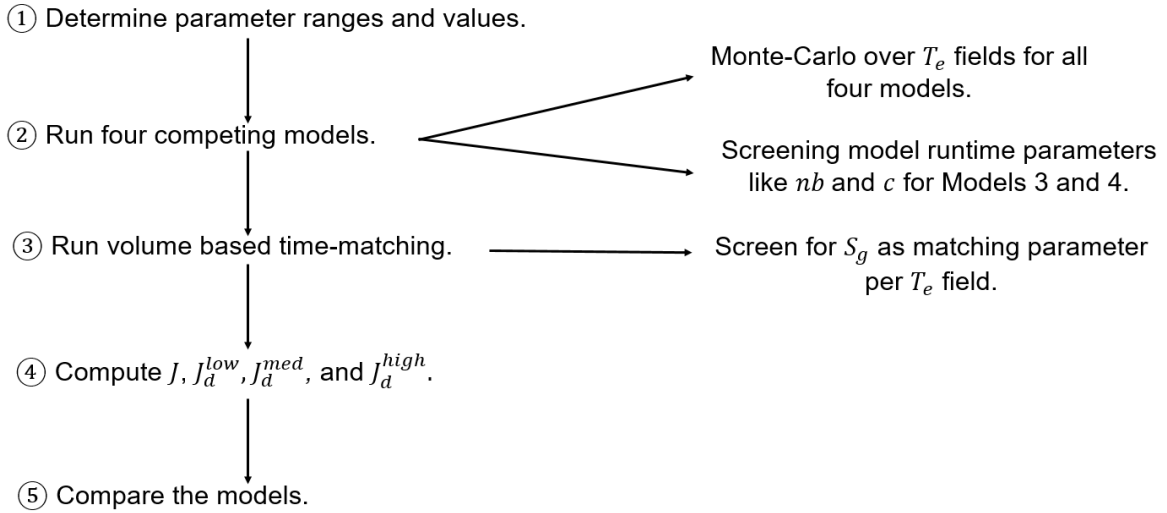
① Determine parameter ranges and values.

② Run four competing models.

Monte-Carlo over T_e fields for all
four models.

Screening model runtime parameters
like nb and c for Models 3 and 4.

③ Run volume based time-matching. ⟶ Screen for S_g as matching parameter
per T_e field.

④ Compute J, J_d^{low}, J_d^{med}, and J_d^{high}.

⑤ Compare the models.

Figure 4.2: Flow chart listing the steps of the model-comparison setup.

to appropriately account for the uncertainty involved with the entry threshold (T_e) fields.

Prior to this, step ① requires some parameter specifications. I run Model 3 (Section 2.3.5) for varying numbers of blocks to invade (nb) at each step, creating many sub-versions of this model to test the best-fitting value. At injection rates of 100ml/min and 250ml/min, I expect a higher number of blocks to perform well because a high volume of gas is injected into the system. I set the range of nb by visual inspection. For the experiments at injection rate of 10ml/min, nb takes the values $\{2, 3, 4, ...10, 15, 20\}$. I assign values of $\{2, 3, 4, ...20, 25, 30, 35, 40, 50\}$ to nb for the triplicate experiments at injection rates of 100ml/min and 250ml/min. Please note that larger nb values (> 50 blocks per step) would lead to inflated circular shapes instead of multiple gas fingers, and hence $nb = 50$ was set as the upper limit.

Further, I run Model 4 (Section 2.3.6) for some representative c values: $\{5, 10, 15, 200, 500\}$, creating five sub-versions of this model to test the best-fitting value. I assume that, while the transitional flow regime (10ml/min) would prefer higher c values (200 or 500), the continuous flow regime (100ml/min and 250ml/min) would prefer low c values, because low c values allow the gas to spread more laterally instead of strictly moving upwards. Please also note here that I ran the simulations for $c < 5$ values as well. But this did not lead to systematic improvements or more insightful results, so I excluded them from further analysis due to their very long runtime. Further, in this study, I do

not aim to formally optimize the c value for specific model variants with an extensive search over the feasible parameter space.

In step ③, I run the time matching procedure (Section 3.1) for all the model versions and sub-versions mentioned above. Additionally, to calibrate gas saturation values assigned per block of the model domain within the time matching, I conduct the time-matching by varying the S_g values in Equation 3.2 in the range of $0.02 - 0.44$ (in accordance with experimentally observed gas saturation values of Van De Ven et al. [2020]).

In step ④, I compute the Jaccard coefficient (J), and the Diffused Jaccard coefficient values (J_d^{low}, J_d^{med}, and J_d^{high}) at three levels of blurring (see Section 4.2) to assess the quality of fit between the experimental images and the corresponding-time matched model images. Per T_e field realization, I want the model to choose its most suitable saturation value based on the maximum metric value. Also, these metrics are used for comparing the performance of the competing model versions.

4.2 Blur-radii for Diffused Jaccard Coefficient

I choose three different blur-radii for evaluating the Diffused Jaccard coefficients.

1. **Low blur:** I choose this blur radius such that images from the experiments (see, Figure 4.1) lose the sharpness of the pixels but do not lose their identity, i.e. the different blurred experimental images look different. This corresponds to any application where one forgives errors in individual pixel values but insists on a close match in shape (Low blur row of images in Figure 4.3). The chosen value of σ for this blurring is 1.2% of the domain size, i.e. image width. The Diffused Jaccard coefficient calculated using this blur radius is denoted as *Diffused Jaccard coefficient (low)* (J_d^{low}) in this study.

2. **Medium blur:** I choose this blur radius such that images from the experimental triplicate at any injection rate (each row of Figure 4.1) look similar, but that the images across different injection rates look different. This corresponds to applications where it is sufficient to identify diversion by flow-inhibiting structures and the overall direction of the growing finger (Medium blur row of images in

Figure 4.3). The chosen value of σ for this blurring is 4% of the domain size. Please note that it is not entirely attainable, e.g., when a finger, like in experiment 10-B, favours a particular direction of flow, no amount of blurring can make it look like fingers from 10-A or 10-C where the flow is clearly in the centre of the cell. The Diffused Jaccard coefficient calculated using this blur radius is denoted as *Diffused Jaccard coefficient (med)* (J_d^{med}) in this study.

3. **High blur:** I choose this blur radius such that images from all the experiments (Figure 4.1) lose the individual details in finger structure and start looking similar. This corresponds to any application where one is interested only in the macroscopic direction of the gas finger and in no further details (High blur row of images in Figure 4.3). The chosen value of σ for this blurring is 8% of the domain size. Please note again that the images from all experiments cannot look the same with any meaningful blur radius. The higher flow rates have multiple fingers and more gas in the system and can thus handle more blurring than the lower injection rate experiments that generate a single finger. The Diffused Jaccard coefficient calculated using this blur radius is denoted as *Diffused Jaccard coefficient (high)* (J_d^{high}) in this study.

In Figure 4.3, I show the resulting images of the experiments 10-A, 100-A, and 250-A, with and without the blurring. The other blurred experimental images are in Appendix B.

4.3 Results and Discussion

Note that, in this discussion, I use the term "metric" to address the Jaccard coefficient, Diffused Jaccard coefficient (low), Diffused Jaccard coefficient (med), and Diffused Jaccard coefficient (high) altogether. In Section 4.3.1, I comment on the ranking of the models. I further support the deductions from the metric-based ranking by visual evidence in Section 4.3.2. In Section 4.3.3, I discuss the importance of the random entry threshold fields as model input. Then, I discuss the results from calibrating the gas-saturation parameter in the models in Section 4.3.4.
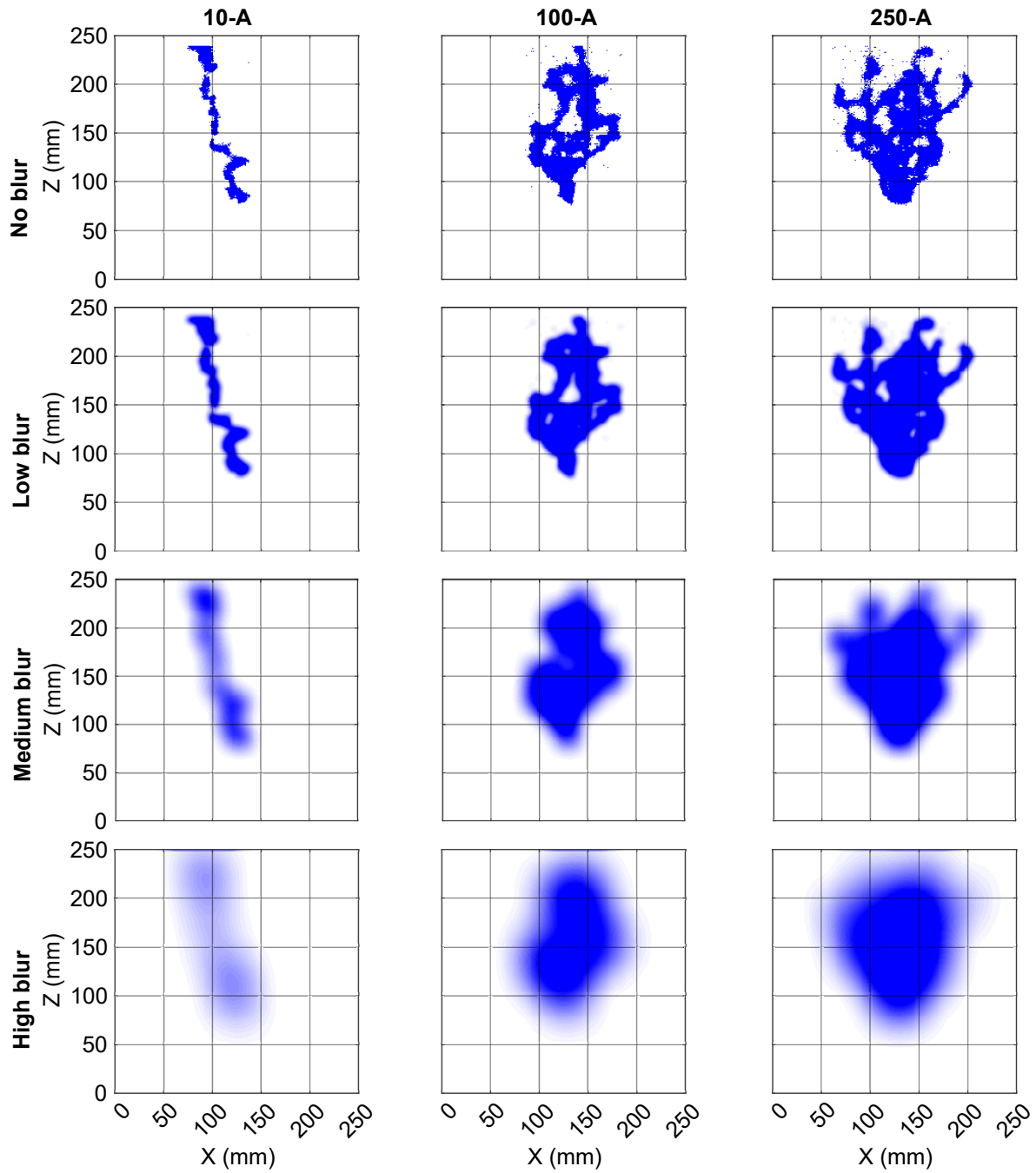
Figure 4.3: Final experimental image of the experiments 10-A, 100-A and 250-A. Row 2-4 contains the blurred version of the images of Row 1 for the three different blur-radii.

4.3.1 Overall Ranking of Models

I begin the discussion by commenting on the overall ranking of the competing models based on the maximum metric value out of the 500 Te field runs. The table specified by Figure 4.4 shows that, for all metric values and across most experiments, Model 1 and Model 2 rank poorly compared to Model 3 and Model 4. This is entirely expected for the experiments of the continuous flow domain (with injection rates 100 ml/min and 250 ml/min) because Model 1 and Model 2 do not include rules incorporating the gas-fingering behaviour (viscous effects, multiple fingers etc.) at these injection rates.

Injection rate	10 ml/min				100ml/min				250ml/min				
Models	1	2	3	4	1	2	3	4	1	2	3	4	
A	0.207	0.187	0.297	0.225	0.110	0.106	0.446	0.381	0.083	0.080	0.439	0.422	Jaccard coefficient
B	0.135	0.129	0.168	0.178	0.142	0.137	0.494	0.392	0.090	0.086	0.535	0.408	
C	0.141	0.138	0.185	0.161	0.144	0.137	0.486	0.366	0.107	0.103	0.417	0.423	
A	0.338	0.325	0.473	0.372	0.133	0.130	0.541	0.453	0.096	0.092	0.521	0.496	Diffused Jaccard coefficient (low)
B	0.234	0.227	0.308	0.278	0.201	0.191	0.612	0.488	0.109	0.098	0.644	0.491	
C	0.265	0.260	0.320	0.271	0.173	0.169	0.620	0.474	0.134	0.130	0.490	0.491	
A	0.493	0.474	0.713	0.628	0.164	0.154	0.670	0.604	0.112	0.104	0.605	0.605	Diffused Jaccard coefficient (med)
B	0.384	0.364	0.490	0.471	0.238	0.218	0.747	0.615	0.122	0.110	0.758	0.623	
C	0.463	0.449	0.539	0.478	0.203	0.188	0.784	0.578	0.148	0.142	0.572	0.610	
A	0.527	0.501	0.821	0.700	0.175	0.158	0.758	0.753	0.120	0.107	0.674	0.700	Diffused Jaccard coefficient (high)
B	0.458	0.422	0.639	0.617	0.244	0.218	0.827	0.715	0.122	0.110	0.842	0.705	
C	0.584	0.551	0.725	0.709	0.216	0.194	0.873	0.663	0.152	0.145	0.652	0.633	

(Left axis: Triplicate Experiments. Right colour scale: better (green) → worse (yellow).)

Figure 4.4: Table containing the maximum metric value for each model version out of the 500 Te field runs and for the best gas-saturation (S_g) value (see Section 4.3.4). For Model 3 and Model 4, the metric corresponds to the respective best parameter value (see Table 4.1). The green colour represents good model performance, and the yellow colour represents poor model performance.

In the transitional flow domain (10 ml/min experiments), gas flow behaviour already shows characteristics of the continuous flow regime [Van De Ven and Mumford, 2019], where capillary forces do not entirely dominate over the viscous forces (Section 2.1). Recall from Sections 2.3.3 and 2.3.4 that Models 1 and 2 do not account for viscous effects and are completely formulated to be operated in the slow gas flow regime (discontinuous flow). Therefore, the contrast in performance between Models (1,2) and (3,4)

is higher for higher injection-rate experiments. Accordingly, the difference in metric values is higher for 100ml/min and 250ml/min in the table specified by Figure 4.4. On that account, I do not recommend the use of Model 1 and Model 2 for the entire transitional and continuous flow regime. Overall, in my study, Model 3 emerges as the best-performing model for most experiments and metrics, always (and often closely) followed by Model 4.

The blurring of the images does not change the overall ranking of the models across all investigated scales of interest. That means: the difference in the model outputs occurs (e.g. finger width, finger direction etc.) even on larger scales. I discuss the effect of blurring further when I discuss the models' relative performance across all 500 T_e field realizations (see Section 4.3.1).

What about the Parameter Values of Models 3 and 4?

Models 3 and 4 have additional parameter values nb and c, respectively, that have been tested on a range of values (see Section 4.1). In Table 4.1, I report the parameter values corresponding to the best-performing metric values of Figure 4.4, i.e. again for the best-performing T_e field per model.

As anticipated in Section 4.1, at injection rates of 100 ml/min and 250 ml/min, Model 3 performs best with a higher number of blocks of invasion (see columns of 100 ml/min and 250 ml/min in Table 4.1). For Model 4, the best performing c values for injection rates of 100 ml/min and 250 ml/min are indeed the smallest on the list: $c = 5$ (see columns of 100 ml/min and 250 ml/min in Table 4.1), as already predicted in Section 4.1.

Observe that, for the injection rate of 10 ml/min, the best c values of Model 4 also correspond to the ones contributing to more inner randomness, i.e. the ones that assist in the radial spreading of the gas. This is unexpected at first sight: at an injection rate of 10ml/min, viscous effects exist but are not predominant, i.e. one observes less radial spreading in the experiments (top row of Figure 4.1). I have observed similar behaviour in one of my works [Banerjee et al., 2023], which will be discussed in Section 5.5.2, where the experimental data belonged to the discontinuous gas flow regime.

Table 4.1: Table containing the values of the best respective parameter value for Models 3 and 4 for the best-performing gas-saturation (S_g) value (see Section 4.3.4), i.e., number of blocks (nb) for Model 3 and c values for Model 4. The evaluation is based on Jaccard coefficient (J), Diffused Jaccard coefficient (low) (J_d^{low}), Diffused Jaccard coefficient (med) (J_d^{med}), and Diffused Jaccard coefficient (high) (J_d^{high}).

	Injection rate	10 ml/min		100 ml/min		250 ml/min		
	Models	3	4	3	4	3	4	
	Parameters	nb	c	nb	c	nb	c	
	A	8	10	50	5	50	5	
	B	3	15	40	5	50	5	J
	C	5	5	30	5	50	5	
	A	8	10	40	5	50	5	
	B	3	15	35	5	50	5	J_d^{low}
	C	5	5	30	5	50	5	
Experiment Triplicate	A	6	15	40	5	50	5	
	B	3	5	35	5	50	5	J_d^{med}
	C	3	200	30	5	40	5	
	A	5	15	40	5	50	5	
	B	4	5	35	5	50	5	J_d^{high}
	C	3	10	30	5	40	5	

Two opposing arguments are relevant to understand these surprisingly low c values at 10 ml/min. On the one hand, the higher c values (200 or 500) for a given invasion threshold are almost deterministic in their choice of the gas path. When these c values meet the entry threshold (T_e) field closest to the actual experiment conditions, the model can accurately produce the gas path with the highest similarity to the observed experimental gas finger. But for any threshold field with poor resemblance to the actual experimental conditions, models with these high c values produce poor-fitting gas fingers. On the other hand, models with lower c values are more flexible in their choice of a gas path for a given invasion threshold field (T_e). Combining the two arguments, these best-performing low c values indicate that, in the absence of a good fit of the structure of the T_e field to the experimental porous medium, the more flexible models fare well.

Relative Performance of the Models across 500 Runs.

Until now, I have discussed the model performance based on the overall maximum metric value out of the 500 runs. To analyse the relative performance of the model versions and sub-versions (with varying parameters, see Section 4.1) across 500 runs per metric value, I inspect the percentage of ranks obtained by each of them. I present a few plots to aid the discussion in Figs. 4.5 and 4.6. Please note that these rankings are relative among the models (and model sub-versions) per individual experiment, and it thus does not indicate whether any of these models are the best fit for the experiments used in this study.

Observe from the rank-plots of experiments 10-A, 10-B, and 250-A using the Jaccard coefficient (Figure 4.5, top row, and Figure 4.6 top), that the Models 1 and 2 rank mediocre to poor amongst all the model versions (including sub-versions of Model 3 and 4). Further, notice that the best model according to the overall maximum metric value (Model 3, see table specified by Figure 4.4) does not consistently rank well for all the 500 T_e fields (This becomes visible by the presence of red colour in the bars of the Model 3 sub-versions in Figure 4.5 and 4.6). This indicates that the T_e field is an essential input for these models, which will be further discussed in Section 4.3.3.

Also, notice that Model 4 with larger c values representing more systematic behaviour (relying primarily on the T_e field) ranks the best for 10-A (e.g., see bars 4c200 or 4c500 of the top row, left plot in Figure 4.5), and those with c values representing somewhat directionless randomness to partially overrule the T_e field, rank better for 10-B (e.g., see bars 4c5 or 4c10 of the top row, right plot in Figure 4.5). In the experimental results of 10-B, the gas finger moves towards the right boundary of the domain, indicating the significant influence of the T_e field in this experiment compared to 10-A where the gas moves through the centre of the domain (see Figure 4.1). The probability of a random T_e field leading to a good match with that of experiment 10-B is extremely low. To overcome this large uncertainty in the T_e field in the models, the more flexible models (with more randomness at lower c values) perform better. In an overall conclusion, the T_e field matters for all models investigated here.

For higher injection rates, Model 4 with different c values ranks the best for some realizations and worst for others (e.g., the red-blue bars from the top plot in Figure 4.6). This confirms that these models have gas finger patterns resembling the experimental
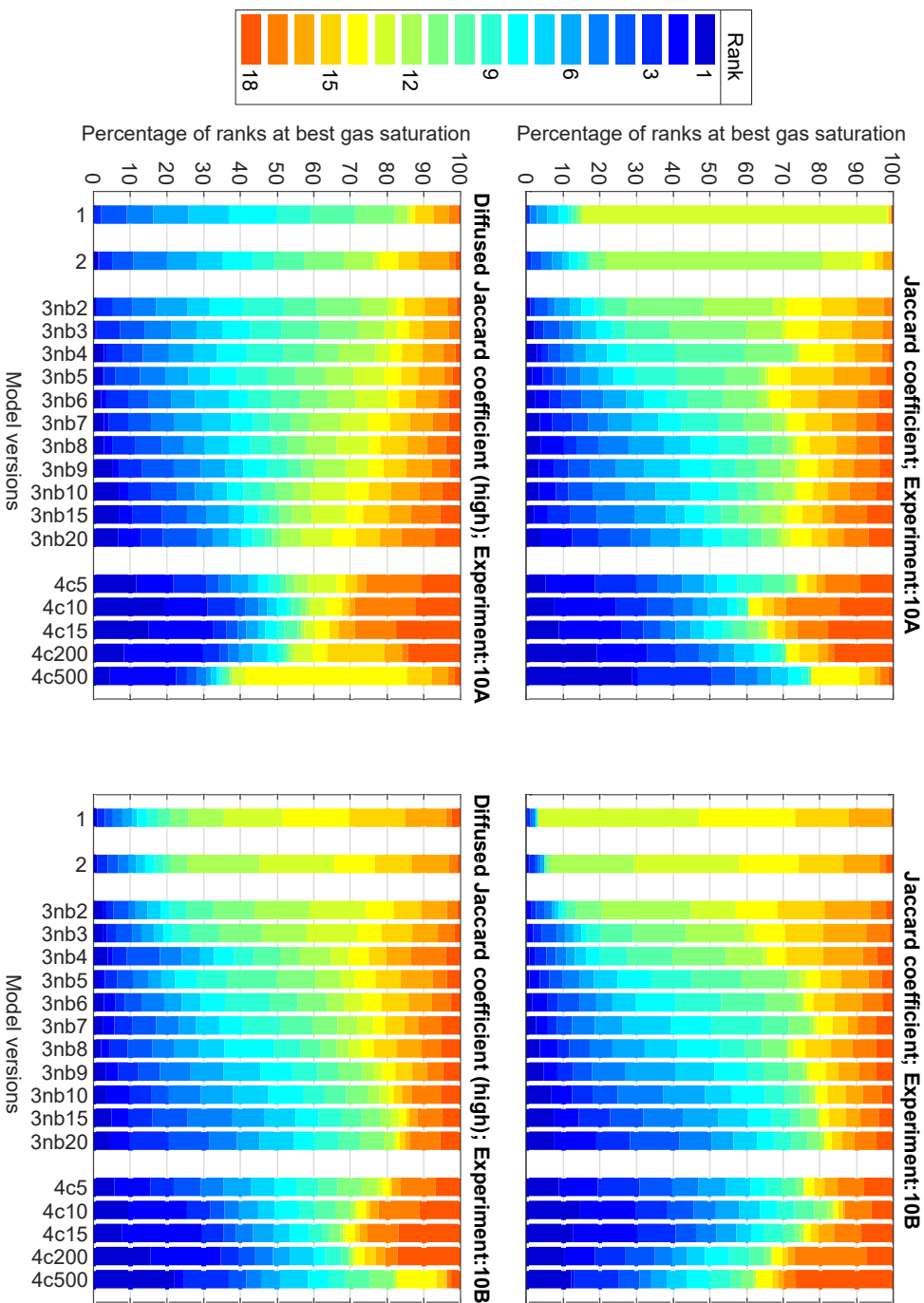
Figure 4.5: Bar plot of the percentage of relative ranks obtained by each model version out of the 500 runs for the best-performing gas-saturation value for the corresponding run. The plots are for experiment numbers 10-A and 10-B, and the corresponding metric used for ranking is mentioned in the title of the subplots. Labels 1 and 2 correspond to Models 1 and 2 of this study. The label 3nb2, 3nb3... stands for Model 3 with $nb = 2, 3, ...$ invaded blocks and the label 4c5, 4c10,... stands for Model 4 with $c = 5, 10, ...$ respectively.
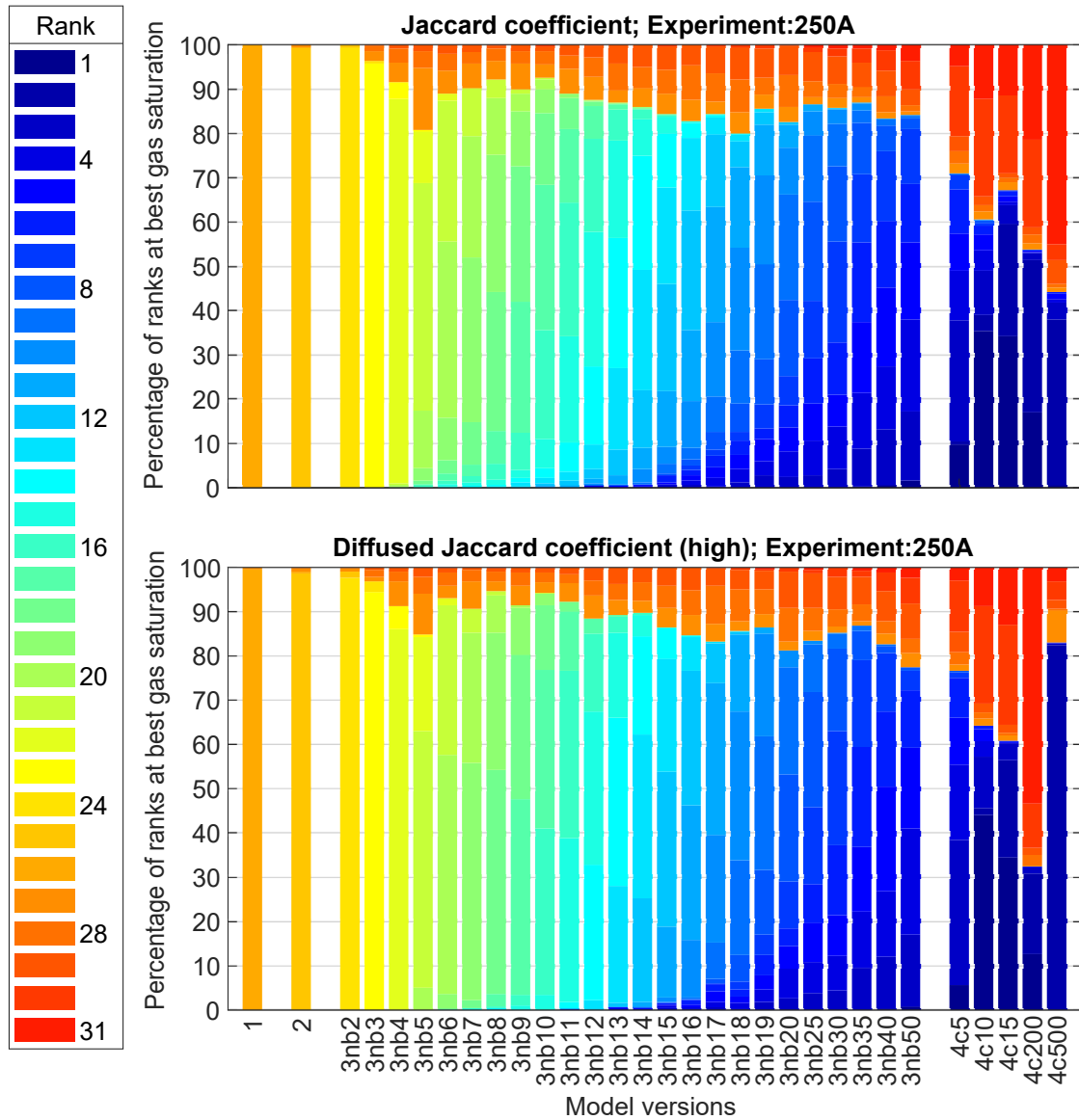
Figure 4.6: Bar plot of the percentage of relative ranks obtained by each model version out of the 500 runs for the best-performing gas-saturation value for the corresponding run. The experiment number 250-A and the corresponding metric used for ranking are mentioned in the title of the subplots. Labels 1 and 2 correspond to Models 1 and 2 of this study. The label 3nb2, 3nb3.... stands for Model 3 with $nb = 2, 3, ...$ invaded blocks and the label 4c5, 4c10,... stands for Model 4 with $c = 5, 10, ...$ respectively.

images only when accompanied by "good" T_e fields. With T_e fields far away from that of the experiment, these models perform the worst. Hence, the "very good" Model 4 is highly sensitive to the T_e field input.

Blurring the images (i.e. comparisons at larger scales) makes the ranking less strict. Even weak models like 1 and 2 rank well for a higher percentage of times (see bottom row plots in Figure 4.5) than they do for the non-blurred image comparison, i.e. using the plain Jaccard coefficient. However, for a high injection rate, blurring cannot help these models improve their ranking (bottom plot for Figure 4.6) because the models are missing surrogate processes for viscosity, which is essential in this flow regime. The extensions proposed in Models 3 and 4 in this regard perform well.

4.3.2 Detailed Discussion of the Model Selection Results

I further support the rankings observed in Section 4.3.1 with more visual evidence and provide insights into the performance of the individual model (with its best T_e field).

Comparing the images (both blurred and non-blurred) of experiment 100-A and 250-A of Figure 4.3 to outputs from Model 1 and Model 2 (Figure 4.7), one can see that they are incapable of producing branched gas-finger patterns resembling those from experiments at higher injection rates. Even with a high blurring radius, Model 1 and Model 2 produce patterns very different from the experiments at 100ml/min or 250ml/min. This is simply because they are incapable of having high volumes of gas in the domain, caused by their tendency to produce single thin fingers. I would refer you to Appendix B for more visual evidence.

Model 3, which emerges as the best model for almost all the metrics and experiments in Section 4.3.1, has more gas in the system (with many gas-occupied blocks in the domain) (Row 3 and columns 2 and 3 of Figure 4.7). This is why it matches the higher injection rate experimental images better than Models 1 and 2.

The experimental images for triplicate at any particular injection rate differ in structure. Even with very high blurring, experimental images from 250-A (Figure 4.3) and from 250-C (Figure B.2) have different patterns. This difference is not observed in the respective best-fitting outputs from Model 3 (see Figure 4.8 and Figure B.13). The
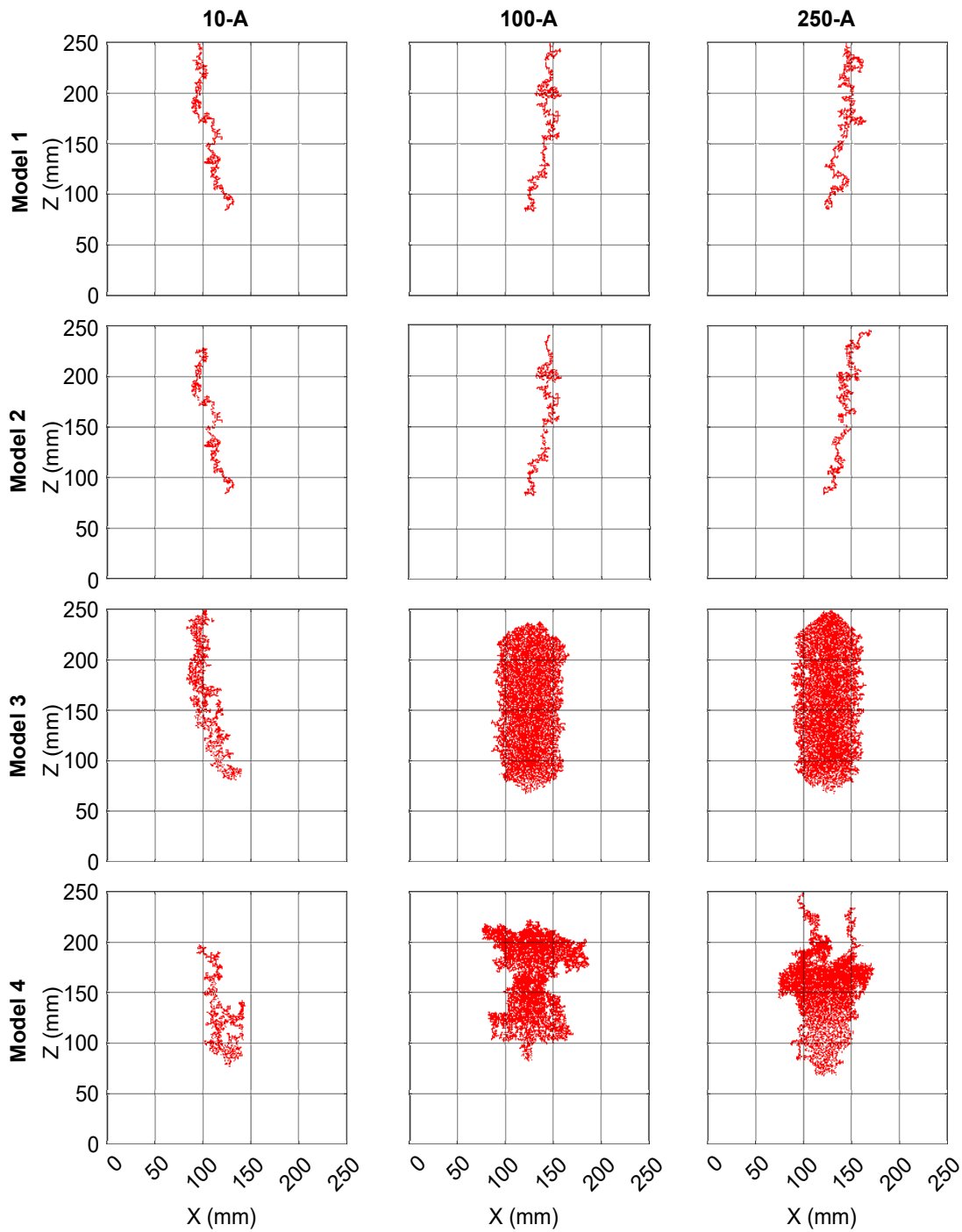
Figure 4.7: Model images for the different model versions with the best fit to non-blurred experimental images (with highest Jaccard value) from experiment no. 10-A, 100-A and 250-A. Row 1, Row 2, Row 3 and Row 4 correspond to Model 1, Model 2, Model 3 and Model 4, respectively.
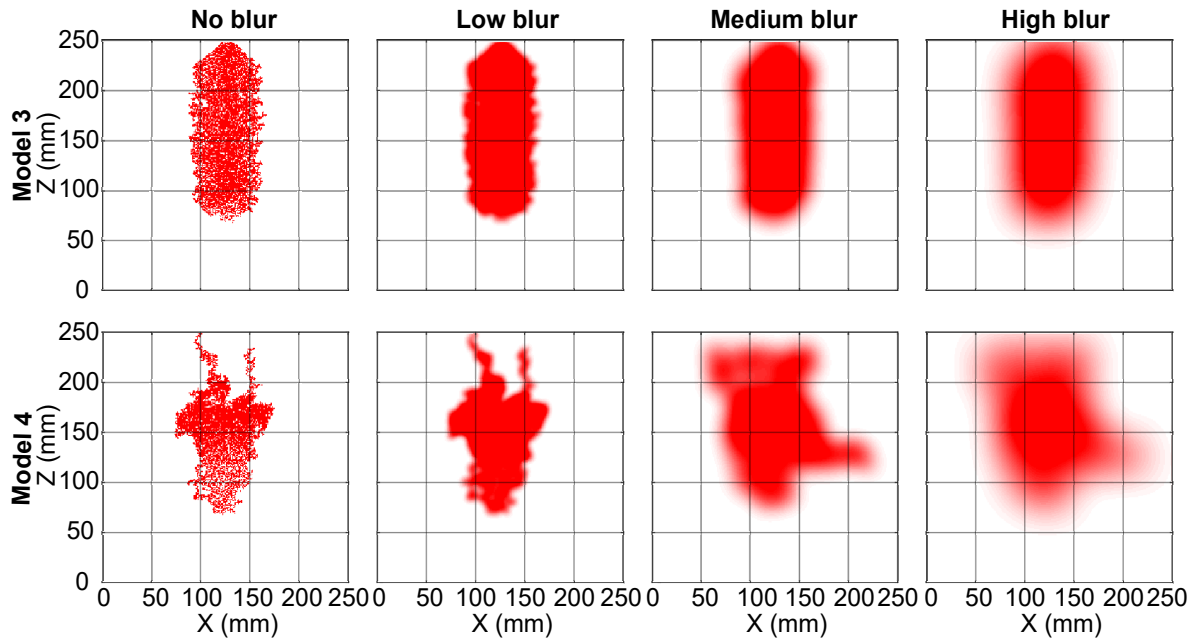
Figure 4.8: Best-fit model images for Models 3 and 4 relative to non-blurred and blurred versions of experimental image 250-A.

gas finger patterns produced by Model 3 are hardly distinct from one another (see Figure 4.8).

Model 4, due to the inherent randomness in the invasion decision, can have many gas-occupied blocks within the domain (Row 4 and columns 2 and 3 of Figure 4.7), facilitating a lateral spread of gas. However, unlike Model 3, it produces distinctive patterns. For example, in Figure 4.8, the best-fitting Model 4 outputs to the various blurred versions of the experimental image of 250-A are not all alike. Note that although the patterns are distinct, they are not always completely similar to the experimental image.

Therefore, I again recommend that Model 1 and Model 2 should not be used for transitional or continuous gas flow regimes. Model 3 can be used for the transitional gas flow regime (with single, slightly thick fingers). At higher flow rates with many-branched fingers (continuous flow regime), Model 3 can be used at large scales (with blurring), but *with caution*: Model 3 is not capable of differentiating between different gas cluster shapes and structures. Thus, using Model 3 in the continuous regime will likely misrepresent gas volumes, pathways, and gas-water contact with associated effects on storage and mass transfer estimates. The close runner-up model (Model 4) is a suitable

candidate for use in transitional and continuous flow regimes (identifying the different shapes of gas clusters), but the underlying rules need to be modified to closely match the gas flow processes involved at high injection rates, which is beyond the scope of the presented thesis.

4.3.3 Importance of the Entry Threshold Fields

From the discussions in the sections above, it is clear that the underlying structure of the T_e field is an important input for these models. Recall that each of the best-performing metrics in Figure 4.4 corresponds to a best-fitting T_e field. *Are there any similarities in the structures of these otherwise random best-fitting T_e fields for the different models?* I try to identify one path of least resistance through the T_e fields by running Model 1 on them. This means that Model 1 runs on the best T_e field for each model version evaluated using the maximum Jaccard coefficient. I choose Model 1 because, in it, all parameters except the T_e field are assumed fixed. The overlay of the so-obtained gas fingers on the experimental image shows that they partially cover the actual paths of the gas finger (Figure 4.9). This answers the question pertaining to the similarities in the underlying structure of the best-fitting T_e fields.

Further, this observation (from Figure 4.9) provides strategies to handle the importance of the T_e fields in spite of its uncertainty for these models. The strategy of Trevisan et al. [2017] was to run their IP model over multiple realisations of their T_e field to account for the uncertainty of the geological heterogeneity in their experimental setup. This seems a viable approach in this regard. Additionally, my comparison metric can be used to identify the "good performing" T_e fields for each model type. One could operate a (geostatistical) Bayesian inference to estimate (or conditionally simulate) the T_e fields, e.g., using Markov chain- Monte Carlo (MCMC) methods for random fields [Xu et al., 2020], a parameter Ensemble Kalman filter (EnKf) (e.g., Kalman Ensemble generator by [Nowak, 2009]) or transformed versions [Schöniger et al., 2012a].

4.3.4 Best-fitting Gas Saturation Values

Recall that the results presented in the table specified by Figure 4.4 used the best-fitting gas saturation values (S_g) resulting from the time matching procedure per model and
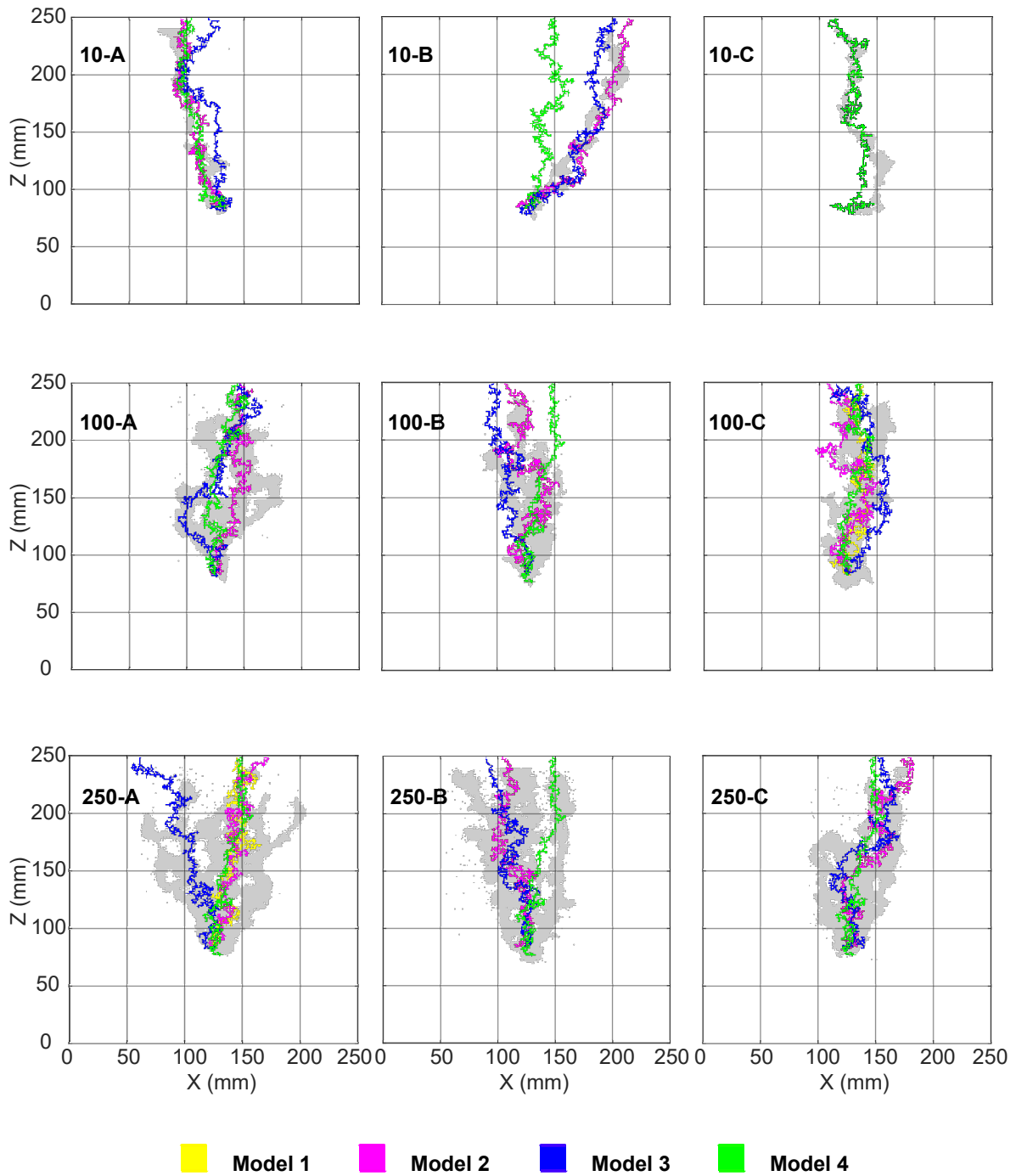
Figure 4.9: Figure shows the T_e field chosen for the maximum Jaccard coefficient per model
version. It is produced using Model 1, in which only T_e fields vary; the other
parameters are constant. Grey-coloured gas fingers represent the experimental
image. Please note that each of the nine images has five different coloured fingers.
The colours not visible in any of the sub-images are due to the overlap of pixels.

realization (of T_e field). Now, I investigate these best-fitting S_g values from my proposed range for each model per metric (Section 4.1). Remember that the experimental data and model outputs are binary (gas-presence/gas-absence) images. The gas saturation values are an overall value provided to the entire gas cluster, i.e. all gas blocks in the binary image are replaced by the same gas saturation value. Varying the gas-saturation value varies the V_{mod} in Equation 3.2, thus altering the corresponding time-matched image from the model outputs. Thus, the value of the metric changes when I change the gas-saturation value. In Table 4.2, I present the best-performing gas-saturation values corresponding to the best metric values for the three experimental triplicates (table specified by Figure 4.4).

While some of the gas-saturation values reported in Table 4.2 are comparable to those found in the experimental data, some are infeasible. For example, a value of $S_g = 0.02$ (appears multiple times in Table 4.2) for the entire gas cluster is clearly too low.

I further investigate the distribution of the gas saturation (S_g) values per model (sub-) version for all 500 T_e field realizations. For that, I present a sample of nine scatter plots for S_g (matched per T_e field realization) versus the metric (Jaccard coefficient and Diffused Jaccard coefficient (high)) for selected models (Model 1, Model 3 and Model 4) and experiments 10-A, 100-A, and 250-A in Figure 4.10. I pick the sub-versions of Models 3 and 4 with the best-performing parameter values: nb and c, for the corresponding cases (see Table 4.1).

There is no clear optimal value of S_g, i.e. the values do not show a cluster of points at an exceptionally high metric value for any particular S_g value (see Figs. 4.10**a**, 4.10**b**, 4.10**c**, 4.10**f**, 4.10**g** and 4.10**h**). It instead seems to be an individual choice of these models per T_e field. For example, in the case of non-blurred images (evaluation using J), more strict models (Model 1 and 2) stick to specific S_g values (see Figure 4.10**a**). For blurred images of the same strict models, the spectrum of well-performing S_g values increases, but it still does not tend to one optimal value (see Figure 4.10**b**). The blurring of the images spatially diffuses the pixels, and the actual structure of the gas finger becomes less relevant, which makes up for the conceptual weakness of Models 1 and 2, allowing them to cope with more varied S_g values. In other words, conceptually strong models are more flexible in their choice of S_g values. This is further supported by the observed spread of S_g values for Model 3 with $nb = 8$ (Figure 4.10**c**), which

Table 4.2: Table containing gas saturation values corresponding to the maximum metric value, Jaccard coefficient (J), Diffused Jaccard coefficient (low) (J_d^{low}), Diffused Jaccard coefficient (med) (J_d^{med}), and Diffused Jaccard coefficient (high) (J_d^{high}).

Injection rate	10 ml/min				100ml/min				250ml/min				
Models	1	2	3	4	1	2	3	4	1	2	3	4	
A	0.28	0.28	0.20	0.36	0.28	0.36	0.36	0.44	0.12	0.12	0.12	0.28	J
B	0.28	0.28	0.36	0.44	0.36	0.36	0.44	0.28	0.28	0.28	0.12	0.28	
C	0.28	0.28	0.36	0.44	0.36	0.36	0.44	0.44	0.28	0.28	0.44	0.28	
A	0.44	0.02ᵃ	0.20	0.28	0.28	0.28	0.44	0.02ᵃ	0.02ᵃ	0.02ᵃ	0.44	0.28	J_d^{low}
B	0.02ᵃ	0.02ᵃ	0.36	0.44	0.36	0.36	0.44	0.44	0.28	0.28	0.28	0.20	
C	0.20	0.20	0.36	0.20	0.28	0.28	0.44	0.02ᵃ	0.28	0.28	0.28ᵇ	0.28	
A	0.44	0.20	0.20	0.20	0.28	0.28	0.44	0.02ᵃ	0.02ᵃ	0.02ᵃ	0.20	0.02ᵃ	J_d^{med}
B	0.20	0.20	0.36	0.12	0.28	0.28	0.44	0.44	0.02ᵃ	0.02ᵃ	0.12	0.12	
C	0.20	0.20	0.20	0.44	0.20	0.20	0.44	0.36	0.02ᵃ	0.02ᵃ	0.02ᵃ	0.02ᵃ	
A	0.12	0.36	0.20	0.20	0.44	0.02ᵃ	0.44	0.44	0.12	0.12	0.36	0.12	J_d^{high}
B	0.44	0.36	0.12	0.20	0.12	0.12	0.44	0.44	0.20	0.02ᵃ	0.12ᶜ	0.12	
C	0.36	0.20	0.28	0.02ᵃ	0.36	0.02ᵃ	0.44	0.02ᵃ	0.36	0.12	0.02ᵃ	0.12	

Triplicate Experiments

ᵃ Same metric values also obtained for a gas saturation value of 0.04
ᵇ Same metric values also obtained for a gas saturation value of 0.36
ᶜ Same metric values also obtained for a gas saturation value of 0.20
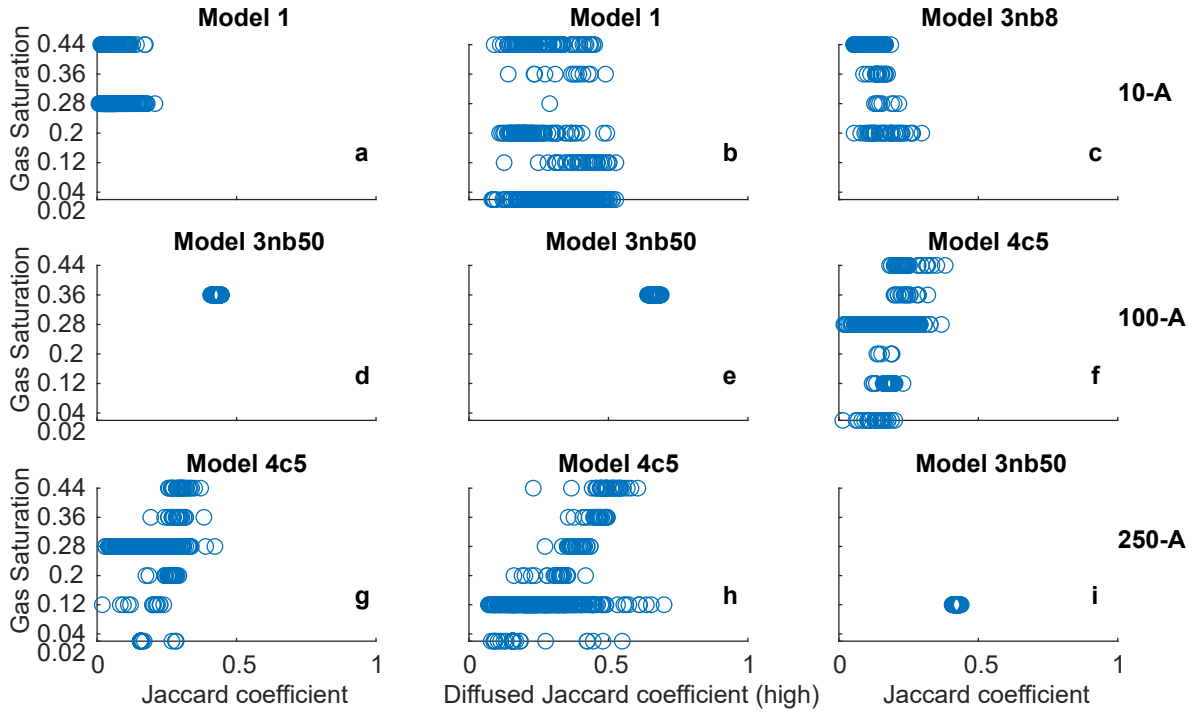
Figure 4.10: A sample of nine plots showing the gas saturation distribution per model (sub-)
version for all 500 realizations over the respective metric values for experiments
10-A, 100-A and 250-A. The title of the subplots 3nb8 and 3nb50 stands for
Model 3 with $nb = 8$ and $nb = 50$, respectively. The title of the subplots 4c5
stands for Model 4 with c value 5.

produced a gas finger with a close resemblance to the original experimental image for
10-A (see Figure 4.3 and 4.7).

Despite the flexibility of choice of S_g values, conceptually strong models are expected
to favour a particular S_g value. For Model 3, which ranks best in most scenarios of
the table specified by Figure 4.4, the sub-version with $nb = 50$ does favour a single
S_g value (see Figs. 4.10**d**, 4.10**e**, and 4.10**i**). However, this optimal S_g value is not
always realistic. For example, the converged S_g value for Model 3 ($nb = 50$) is 0.12
for experiment 250-A (see Figure 4.10**i**). Van De Ven et al. [2020] reported typical S_g
values between 0.2 to 0.4 for the inner core and 0.03 to 0.2 for the outer shell of each gas
finger, for the high injection rate (100 ml/min, 250 ml/min and 498 ml/min) triplicate
experiments of Van De Ven and Mumford [2019]. Thus, the value of $S_g = 0.12$ for the
entire gas cluster is lower than that observed and reported in Van De Ven et al. [2020].
As earlier discussed in Section 4.3.2, Model 3 does not adequately predict the shape
and structure of the gas clusters consisting of multiple fingers. Thus, the favoured S_g

value is merely the model's best attempt to fit the corresponding data.

For the close runner-up Model 4 with $c = 5$, one does not observe any most favoured optimal S_g value (see Figs. 4.10**f**, 4.10**g**, and 4.10**h**). Recall that this model version's performance is highly sensitive to the input of the entry threshold (T_e).

Therefore, the models apparently use the S_g values to compensate either for their own conceptual weakness or for "poor" T_e field inputs. Thus, from Figure 4.10, I can conclude that none of the models can predict the real physical S_g values and thus are not recommended for S_g calibration. As a possible way out, one could develop data assimilation or geostatistical inversion schemes for T_e fields as already mentioned in Section 4.3.3. Then, more plausible S_g values could be obtained as only the conceptual weakness of models would remain as the major error source. Alternatively, model versions with variable gas-saturated blocks [e.g., Ioannidis et al., 1996, Mumford et al., 2010, Koch and Nowak, 2015, Molnar et al., 2019] are an optional extension of macroscopic-IP models, which may be investigated for better calibration of S_g values.

4.4 Summary and Conclusions

I compared the performance of four macroscopic IP models against the data from nine gas-injection in homogeneous water-saturated sand experiments, using time-matching and (Diffused) Jaccard coefficient(s). These models are tested for transitional and continuous gas-flow regimes for the first time. I identified the strengths and weaknesses of these modelling strategies for simulating gas flow in water-saturated sand. Also, I calibrated a few of these model parameters.

Summarizing the results, I conclude that Models 1 and 2 are unsuitable for use in transitional and continuous gas flow regimes, even with high image blurring levels (Section 4.3.1). In particular, these models are completely weak for experiments at higher injection rates.

Models 3 and 4 perform better than Models 1 and 2 but do not accurately represent the gas finger patterns observed in the experiments (Section 4.3.1 and 4.3.2). In previous studies, IP-type models have been used extensively only in the capillary flow regime. The results from the model comparison show that IP models at a macroscopic scale

with variation as Model 3 can be used in transitional gas flow regime (single slightly thick gas finger) but cannot appropriately predict the gas-finger patterns seen in the experiments of the continuous gas flow regime (multiple fingers) (Section 4.3.2). Model 4 is a potential candidate for use in the transitional and continuous gas flow regimes, provided its rules are modified to reproduce the gas-flow behaviour at high injection rates (Section 4.3.2). The modification of Model 4's underlying rules is beyond the scope of the present study.

The blurring of images can be used as an efficient tool for reducing the detailed level of information in the images, depending on the application and the scale of interest. It is pointless to ask for a pixel-to-pixel match at and above the scale of the experiments used in this study, given the strong dependence of gas flow on pore-scale aspects of the porous medium (here: sand pack). This exercise can thus help use models like 3 or 4, which partially consider the viscous effects found at high gas injection rates for such applications. With blurring, i.e. at large scales where individual structures of the gas fingers are irrelevant, Models 3 and 4 may be used for continuous gas flow regimes (Section 4.3.1 and 4.3.2).

The underlying structure of the T_e fields is a critical input for the good performance of these models (Section 4.3.3). Moreover, the best models (3 or 4) are also the most sensitive to this input. The internal randomness of the invasion decision can partially compensate for the high uncertainty in the structure of the T_e fields (Section 4.3.1 and 4.3.2). Also, strategies like running multiple realizations of the T_e field can help tackle this uncertainty of the T_e fields. Further research could be conducted to identify the underlying structure of the T_e fields, e.g., using geostatistical inversion methods. I do not recommend these models for calibrating parameters like gas saturation (Section 4.3.4), at least as long as there is a dominant uncertainty in T_e fields.

5 Method of Forced Probabilities to Compute Bayesian Model Evidence*

In Chapter 1, I discussed the importance of Bayesian Model Selection (BMS) as a tool for the inter-comparison of models in sparsely known uncertain systems. Also, in Section 1.1.5, I highlighted the challenges in computing the Bayesian Model Evidence (BME) for BMS. In addition to these challenges, for a model-data system involving binary (yes/no) decision output (like in this thesis), the likelihood function becomes a Dirac-delta function, thus leading to likelihood values of zero for practically all sampled parameter values of the model. Thus, the BME value would tend to zero, and any model would be rejected as infinitely poor. This becomes a problem, especially for long-time sequences of repeated outputs. For example, in a lotto game, getting the first number right is not that difficult, but getting the exact sequence of six numbers in a row right is almost impossible.

For such model-data systems involving binary output, with *highly discretized atomic-event-type* data and *Markov chain* models, I propose a method discussed in this chapter to compute BME with a reasonably low computational effort. Observed states are called *atomic events* if each individual possible outcome can be enumerated and they are mutually exclusive and collectively exhaustive. *Markov Chain models* are stochastic models that fulfil the Markov Chain property, i.e. the probability distribution of model states in the next (time) step depends solely on the previous step, not on any prior state to that. I call this method of BME computation the *Method of Forced Probabilities* (MFP) due to its core idea: instead of evaluating millions of forward runs that may fit the data by random chance, the model is forced to follow the data during each time step. One records the individual probabilities of the model performing these exact transitions as if they were done without any constraints. Following a strict

---

mathematical derivation, one computes BME as the product of these probabilities. By exploiting the Markov Chain property of the model with this procedure, it is possible to compute BME in previously nearly impossible cases without resorting to any kind of approximations.

Model order reduction techniques offer an alternative approach for optimization, parameter sampling or Bayesian analysis of high-dimensional problems. Reduced-order models are computationally cheap abstractions of the original, high-fidelity models [Zhang et al., 2016]. Examples of such reduced-order modelling techniques include but are not limited to, models obtained using projection-based model reduction methods (e.g., polynomial chaos expansion [Xiu and Karniadakis, 2002], proper orthogonal decomposition [Willcox and Peraire, 2002]), response surface models (e.g., polynomials, kriging, radial basis functions, artificial neural networks, etc.[Razavi et al., 2012]) and, lower-fidelity models (physically reliable simple abstractions of the system under study [Razavi et al., 2012]). Although such reduced-order models assist in solving the computing time problem, they are only approximate. In contrast, my method (MFP) is exact. Also, my method tackles the challenge of evaluating BME rather than the computational efficiency issue of complex high-fidelity models. Further, my method can be used in combination with all reduced-order modelling approaches that maintain the Markov property. Other options include an abstraction of summary statistics from data (so-called approximate Bayesian computation [Beaumont, 2010]), manual-visible techniques (like moments matching [Mumford et al., 2015]), or the use of plausible, non-Bayesian metrics [Banerjee et al., 2021].

In the following section, I introduce the MFP approach for computing BME (Section 5.1), and illustrate it on a didactic example (Section 5.2). In Section 5.3, I introduce a test case for demonstration: I apply the method on Model 4 from Section 2.3.6. The corresponding highly resolved data set is from an experiment with gas injection into water-saturated, homogeneous sand at the rate of 0.1 ml/min (Experiment nr. 0.1-A of Section 2.2), and highlight the challenges in using this data set (Section 5.3.1). I also design a synthetic data scenario for the proof-of-concept of the method (Section 5.3.2) and list the implementation steps of the MFP for the case-study under the different data scenarios (Section 5.4). Further, I add a list of general algorithmic steps of MFP in Section 5.4.3. Section 5.5 discusses the results obtained from the synthetic (Section 5.5.1) and real-data scenarios (Section 5.5.2). Finally, I summarize the contributions of this study and draw conclusions in Section 5.5.3.

5.1 Method of Forced Probabilities (MFP): Key Idea

For the purpose of this study, let us redefine Equation 2.13 as:

$$I_k = \iint_{U_k} p\left(\mathbf{y}_0 \mid \boldsymbol{\omega}_k, \boldsymbol{\theta}_k, M_k\right) \cdot p\left(\boldsymbol{\omega}_k, \boldsymbol{\theta}_k \mid M_k\right) d\boldsymbol{\omega}_k \, d\boldsymbol{\theta}_k. \tag{5.1}$$

Here, the parameter space U_k is split into uncertain parameters $\boldsymbol{\theta}_k$ and random events $\boldsymbol{\omega}_k$, $p(\mathbf{y}_0 \mid \boldsymbol{\omega}_k, \boldsymbol{\theta}_k, M_k)$ is the likelihood of the parameters ($\boldsymbol{\omega}_k$ and $\boldsymbol{\theta}_k$) of model M_k to have generated the data set $\mathbf{y}_0$, and $p(\boldsymbol{\omega}_k, \boldsymbol{\theta}_k \mid M_k)$ is the prior probability density of these parameters. Uncertain parameters $\boldsymbol{\theta}_k$ comprise those parameters and inputs of the model with unknown or non-measurable values. Random events within the model $\boldsymbol{\omega}_k$ represent apparently stochastic system behaviour that cannot be explained deterministically (but only distribution-wise) by the model's equations, assumptions or mechanisms (see also Section 2.3.6).

Using the law of total probability [Kolmogorov, 1950], the double integral of Equation 5.1 is split into an inner integral over random events and an outer integral over uncertain parameters:

$$\begin{aligned} I_k = \int &\left[\int p\left(\mathbf{y}_0 \mid \boldsymbol{\omega}_k, \boldsymbol{\theta}_k, M_k\right) \cdot p\left(\boldsymbol{\omega}_k \mid \boldsymbol{\theta}_k, M_k\right) d\boldsymbol{\omega}_k \right] \\ &\cdot p\left(\boldsymbol{\theta}_k \mid M_k\right) d\boldsymbol{\theta}_k \\ = \int &p\left(\mathbf{y}_0 \mid \boldsymbol{\theta}_k, M_k\right) \cdot p\left(\boldsymbol{\theta}_k \mid M_k\right) d\boldsymbol{\theta}_k. \end{aligned} \tag{5.2}$$

The key idea of the Method of Forced Probabilities is to replace the inner integral (over random events) with a single analytical solution and use an MC integration (Equation 2.14) only for solving the outer integral over uncertain parameters ($\boldsymbol{\theta}_k$), for models obeying the Markov Chain property. This means that for random events $\boldsymbol{\omega}_k$, as opposed to simulating thousands of forward model runs and waiting for a random match with the observed data, one instead records the individual probabilities $p(\boldsymbol{\omega}_k \mid \boldsymbol{\theta}_k, M_k)$ of the model performing the exact transitions observed in the data at each time step. Using the Markov chain property, the product of these probabilities corresponds to $p(\mathbf{y}_0 \mid \boldsymbol{\theta}_k, M_k)$ in Equation 5.2:

$$p(\mathbf{y}_0 \mid \boldsymbol{\theta}_k, M_k) = \prod_{t=0}^{t_{max}-1} \mathrm{P}\left(\mathbf{y}_0(t+1) \mid \mathbf{y}_0(t), \boldsymbol{\theta}_k, M_k\right), \tag{5.3}$$

where $\mathrm{P}\left(\mathbf{y}_0(t+1) \mid \mathbf{y}_0(t), \boldsymbol{\theta}_k, M_k\right)$ is the probability of transition in y_0 (in accordance with the data) from time step t to $t+1$, and t_{max} is the total number of time steps in the experimental data. The idea is to plug this exact analytical solution into Equation 5.2 and use the MC method only for the uncertain parameters.

If numerical scaling becomes an issue for Equation 5.3, one can simply work in (negative) logarithmic scale:

$$
\begin{aligned}
&-\ln p(\mathbf{y}_0 \mid \boldsymbol{\theta}_k, M_k) \\
&= -\sum_{t=0}^{t_{max}-1} \ln P\left(\mathbf{y}_0(t+1) \mid \mathbf{y}_0(t), \boldsymbol{\theta}_k, M_k\right).
\end{aligned}
\tag{5.4}
$$

Further, even after using the logarithmic scale, numerical issues with the BME values can arise during averaging (after exponentiating Equation 5.4) for the outer integral of Equation 5.2 due to the scale and span of individual values. This is addressed by a numerical trick that involves subtracting a common BME value at the logarithmic scale, such that the exponent of Equation 5.4 (Equation 5.2) is closer to zero, see Appendix C.2.

One may argue that the act of multiplying individual likelihoods in order of appearance in a time sequence is close to the process done in data assimilation methods, where a time-series of time slice-wise likelihoods and cumulative BME values can be spit out as a simple by-product. This analogy is most apparent when comparing to particle-filter-like schemes for data assimilation [Gustafsson, 2010]. Moreover, just like my BME computation can be used for parameter selection / Bayesian update of parameters, this could also offer the path to parameter estimation in data-assimilation mode. Some data assimilation schemes perform a joint estimation of system states *and* uncertain parameters, typically called *augmented state vector* approaches [e.g., Ramgraber et al., 2019] or *parameter-space* schemes [e.g., Nowak, 2009, Schöniger et al., 2012b]. Without going into further detail, this opens a future pathway to apply the MFP method in

(real-time) data assimilation for either state forecasting, parameter updating, or both at once.

5.2 Implementation Illustrated with a Didactic Example

As a toy model for illustrating the implementation of the method, let us consider a simple Markov Chain with two output states (0 and 1) and a fixed (instead of uncertain) parameter π_k (e.g., a repeated coin flip experiment). Thus, the Bayesian integral in Equation 5.1 simplifies to:

$$
\begin{aligned}
&p\left(\mathbf{y}_0 \mid M_k\right) \\
&= \int_{U_k} p(\mathbf{y}_0 \mid \boldsymbol{\omega}_k, \boldsymbol{\theta}_k, M_k) \cdot p(\boldsymbol{\omega}_k \mid \boldsymbol{\theta}_k, M_k) d\boldsymbol{\omega}_k,
\end{aligned}
\tag{5.5}
$$

i.e. $\boldsymbol{\theta}_k$ is fixed, and the outer integral disappears. Note here that the integration domain U_k only contains the random events. The transition probabilities of the model are defined as:

$$
\mathbf{P}_k(b \mid a) = \begin{cases} \pi_k & \text{if } b \neq a \\ 1 - \pi_k & \text{if } b = a \end{cases}
\tag{5.6}
$$

Here, b is an output state at a particular flip, and a is an output state in the previous flip.
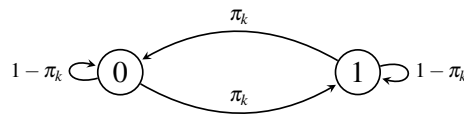
Figure 5.1: Transition graph of toy Markov chain model.

For a number of flips $t_{max} = 3$ (i.e., $t = 0, 1, 2, 3$), the possible predictions by the model are shown in the probability tree diagram in Figure 5.2. Additionally, in this diagram, let us fix the initial condition at $t = 0$ to $y(0) = 0$. Let us assume that the true observation data sequence is 0110 (highlighted in red in Figure 5.2).
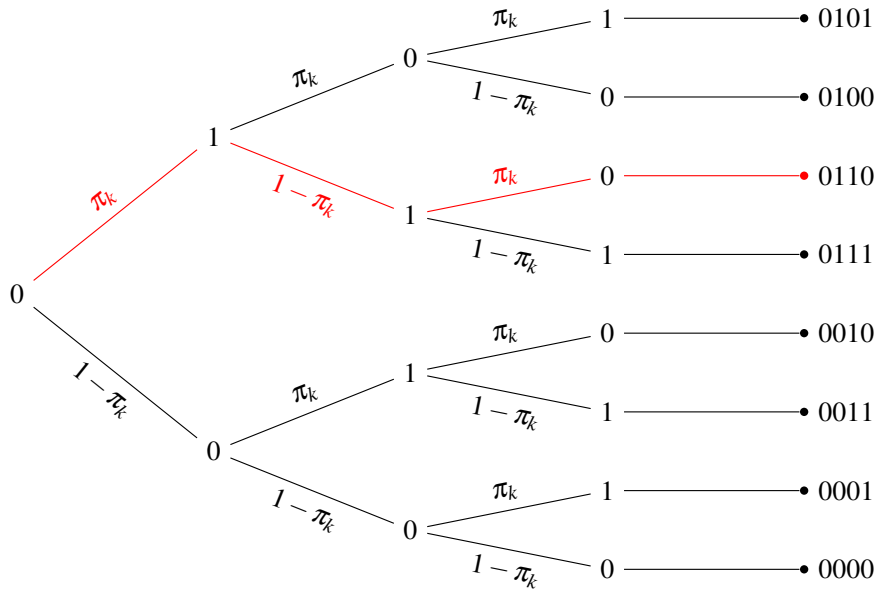
Figure 5.2: Probability tree diagram for the toy Markov chain model with $t_{max} = 3$. The true sequence or observed series of outcomes is highlighted in red.

In such a simple tree structure with equiprobable branching ($\pi_k = 0.5$), it is obvious that the probability (BME) of observing the single true path with likelihood one is $\frac{1}{\text{number of paths}}$. Now imagine if the sequences' length t_{max} increases (a deeper tree) or the dimension of the state space is increased (more than two branches for each node), the complexity of the probability tree diagram will increase exponentially (see Appendix C.1 for more details). For example, for a binary tree with $t_{max} = 100$, one ends up with 2^{100} different paths. This would further diminish the BME value and increase the computational effort to completely sample all possible paths in direct MC-based approaches based on the conventional Equation 2.14.

Most real-world applications involve a more complex structure, where the branches are not equiprobable or complete enumeration is not possible anymore. In such cases, an MC approach would be used to sample each random path in proportion to its probability, requiring an even more significant number of samples to represent all paths, including the ones with very low probability, statistically sufficiently well. Note that it is not enough to "hit" the one path that coincides with the observation, but for an accurate approximation of BME, one needs an accurate representation of low probabilities just as well (zeros play an essential role in arithmetic averaging), see, e.g. Schöniger et al. [2014].

In contrast, the MFP simply calculates BME as the probability of mimicking the observed state changes, i.e., a flip from 0 to 1 and then staying at 1 and finally flip again to 0:

$$p(\mathbf{y}_0 \mid \boldsymbol{\theta}_k, M_k) = \pi_k \cdot (1 - \pi_k) \cdot \pi_k.$$

With $\pi_k = 0.5$, this equals to the enumeration or MC solution of $\frac{1}{8}$. This means that one only needs to calculate a finite product over a set of t_{max} (here: three) values. Therefore, the method (MFP) scales linearly with t_{max} and does not exponentially explode like full enumeration or MC methods.

5.3 Demonstration on a Real Case-Study

I demonstrate the applicability of MFP on a more complex model with Markov Chain property: a version of the macroscopic Invasion percolation model (Model 4: Section 2.3.6). Recall that Models 1, 2 and 3 are deterministic for any given value of $\boldsymbol{\theta}$ and a frozen set of random P_e values (see Equations 2.2 - 2.5). So, there would be no random events $\boldsymbol{\omega}$ within these models. That means computing BME would focus only on the outer parameter-related integral of Equation 5.2. The inner integral would degenerate to a simple yes or no problem. Without addressing measurement errors or any other form of randomness between the model and data, the answer would be a straightforward rejection with BME = 0. Thus, to include the macroscopic IP models in the BME comparison using MFP, a modification of the model to include random events $\boldsymbol{\omega}$ is required. This is why I use Model 4 (Section 2.3.6) for this demonstration.

In this case-study, I compare Model 4 to experimental binary-image data from gas injection in homogeneous, water-saturated sand at an injection rate of 0.1 ml/min, see Section 2.2. The experimental data is a time-series of 2D binary images (around 10,000 images), obtained at the rate of 30 frames per second for a total of 330s [Van De Ven and Mumford, 2019]. An ideal data set for MFP would be where each atomic step (individual invasion events or re-invasion events for each block) is separately visible in time. I pick this particular data set because of its high resolution in both space and time. However, the data obtained is not free from some challenges that need to be overcome to use MFP.

5.3.1 Challenges in Using the Real Experimental Data

1. Firstly, non-atomic events are observed in the data set even at this high temporal resolution. This means that, from the one-time step to the next step, multiple atomic events (e.g. invasions, re-invasions) are found to occur so that their exact sequence is not given uniquely.

2. Secondly, at some time steps, the experimental data shows re-invasion at a block that is incompatible with the model's deterministic re-invasion rule as specified in Equation 2.8.

3. Thirdly, at some time steps, invasion of gas occurs at a block that does not appear to be connected to the cluster containing the original gas injection block, violating the assumptions behind Model 4 (see Section 2.3.4). This disconnection could result from the data's optical detection limits.

4. Fourthly, in some time steps, the number of gas pixels also decreases from the previous time step. This violates the mass conservation principle that the model (in the absence of a variable gas density) simplifies to a volume balance.

With the configuration of Model 4, using MFP would thus lead to zero probability events because of the aforementioned observations (second to fourth) in the data set. This would lead to, within the scope of the present work, meaningless BME computations. This is not an artefact of MFP but would also occur in all other methods to compute BME. The MFP is able to map it to individual zero-probability events, while other BME computation methods would merely return an overall zero value for the entire inner integral of Equation 5.2.

5.3.2 Synthetic Data

For a test in the absence of all problems that real experimental data bring about, I use synthetic model-generated data. By using synthetic data, I first test MFP under ideal conditions. To that purpose, I run Model 4, with cell selection weighting factor (Section 2.3.6): $c = 15$ on a particular invasion threshold field ($T_{e,syn}$) with no re-invasion events (i.e. the rule given by Equation 2.8 is removed) and use the results instead of a real data set. Thus, my synthetic data set consists of a sequence of atomic

events and no measurement errors. It is now guaranteed that the models can follow the data with a non-zero probability. Figure 5.3(a) shows this synthetic truth.

Next, I introduce irregularities in this synthetic data set in a controlled manner. Thus, as a next step, I add non-atomicity to the synthetic data set, which is also observed in the real data set. To make non-atomic synthetic data, I regularly omit time steps, such that Model 4 would need $n_{ev} = 2, 3, 6$ iterations to get from one state to the next. This means I keep only every second, third, and sixth state from our atomic synthetic data set.

5.4 Implementation on Model 4 for Synthetic and Real Data

In this section, I discuss the setup and implementation of the MFP on Model 4 for both the synthetic data set and the real experimental data set. First, I describe the common implementation setup for both types of data sets. Then, in Section 5.4.1 and Section 5.4.2, I will highlight the difference in scenario setups for the corresponding data sets.

I choose three cell selection weighting factors (c) (Section 2.3.6) to correspond to one rather random ($c = 5$), one more deterministic ($c = 100$) and one model version in between ($c = 15$) of Model 4. This results in three model versions of Model 4 for this study. The choice of these three different cell selection weighting factors can be thought of as representative sand pack experiments with different force-dominated regimes: viscous ($c = 5$) or capillary ($c = 100$) [Van De Ven and Mumford, 2019]. The invasion threshold field makes up the uncertain parameters $\boldsymbol{\theta}_k$ over which one has to marginalize the inner integral (random gas-invasion decisions of Model 4) through the outer integral of Equation 5.2 to obtain BME. In contrast to the didactic example of Section 5.2 (Figure 5.2), for Model 4, I consider at each "node" of the decision tree a random decision of gas migration. These random decisions each have multiple, situation-specific possibilities for invasion and re-invasion (illustrated in Figure 5.4) instead of binary decisions.
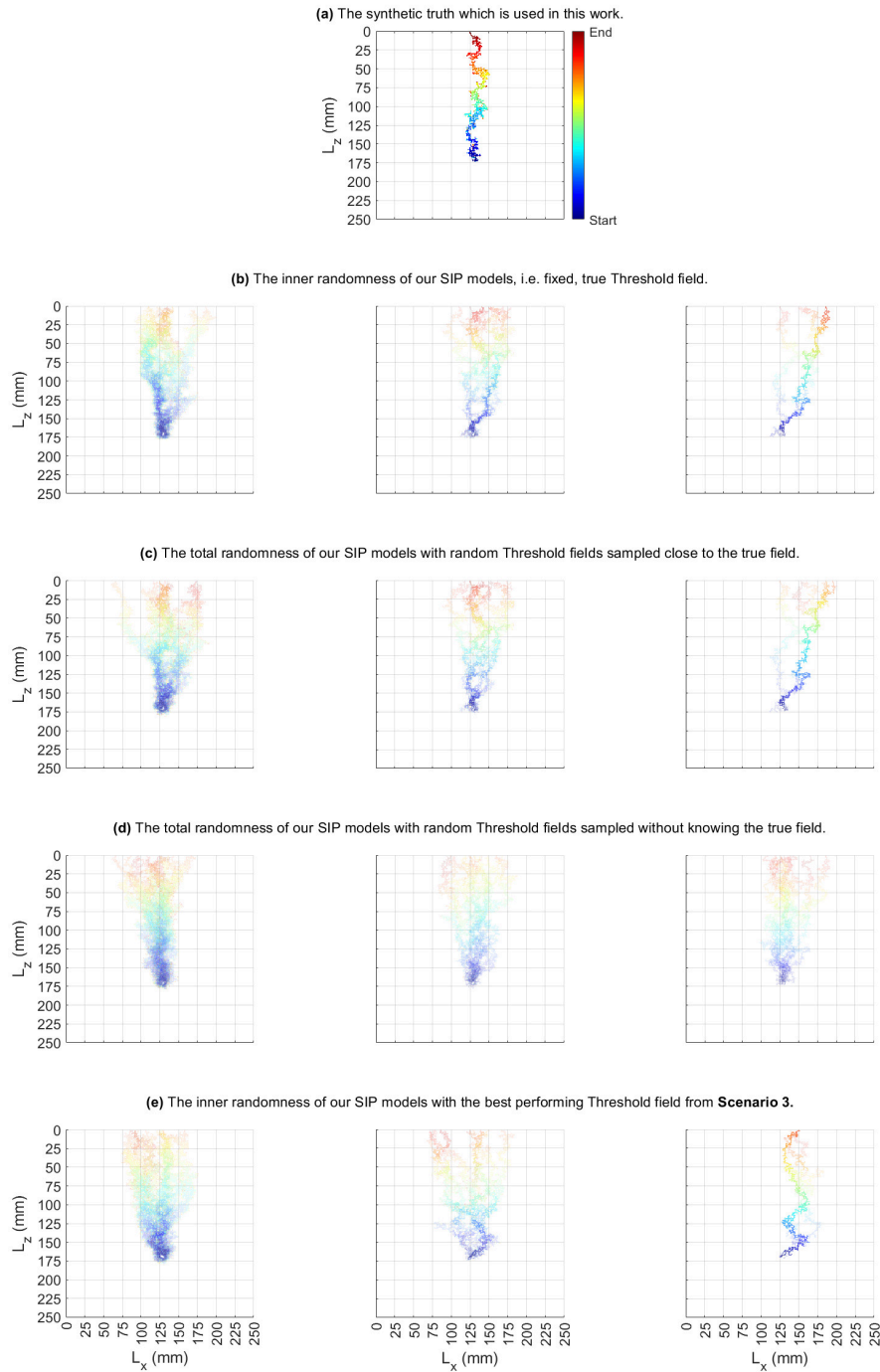
Figure 5.3: To visualize the different Model 4 versions and the synthetic scenarios (Section 5.4.1): this figure shows a sample of 10 model runs for each combination and compares them to the synthetic data set. More frequently invaded cells appear more opaque, and their colour shading indicates the relative time from the first to the last invaded cell. From left to right c values are $5, 15$, and 100.
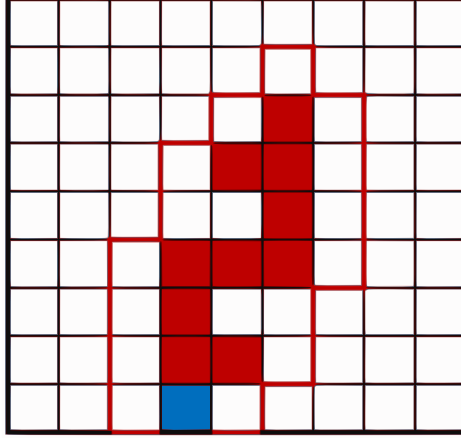
Figure 5.4: Schematic to visualize Model 4 (especially their difference to the didactic example in Figure 5.2); The blue block marks the injection block. The red-filled blocks mark the currently invaded blocks. In the next step, any block on the interface (red-rimmed blocks) might be invaded, and any one of the red-filled blocks or none might be re-invaded

Also, unlike the didactic example in Section 5.2, the probabilities for each forced time-step in Model 4 will not be a constant π_k, or $1 - \pi_k$, but they will depend on multiple factors, namely: (1) the cell selection weighting factor (c), (2) the invasion threshold (T_e) field that depends on the randomized P_e fields and, (3) the current shape of the cluster of gas-invaded blocks at the current time-step. Recall, from Section 2.3.6, the cumulative sum $T_{e,cum}$ (Equation 2.9) and its connection to the uniformly distributed random variable $\mathcal{R}$ in Equation 2.10. The model chooses to invade the block with the index i (of the ascending order structure) and not any other neighbouring block if and only if Equation 2.10 is fulfilled for i and not for $i - 1$, i.e.,

$$T_{e,cum}[i-1] \leq \mathcal{R}^c \times \sum_{j=1}^{j=n} T_e[j] < T_{e,cum}[i] \tag{5.7}$$

Rearranging the terms in the equation above gives us two bounds, and $\mathcal{R}$ must be between

$$\left(\frac{T_{e,cum}[i-1]}{\sum_{j=1}^{j=n} T_e[j]} \right)^{\frac{1}{c}} \leq \mathcal{R} < \left(\frac{T_{e,cum}[i]}{\sum_{j=1}^{j=n} T_e[j]} \right)^{\frac{1}{c}}. \tag{5.8}$$

The interval width between these bounds is the probability of this exact invasion at the block i. Note here that, for the block with index $i = 1$, the lower bound remains undefined by Equation 2.9 and is set to zero.

When investigating non-atomic steps in the data, one cannot simply evaluate the transition kernel of the model implied by Equation 5.8 but must think about a workaround. One can view it like an excerpt of a complete probability tree diagram as shown in Figure 5.2, where n_{ev} atomic events occur. The difficulty lies in not knowing the states and their ordering in between. One knows the start and the end and can only guess the sequence of atomic events that happened in between. This means that any permutation of the events could be a suitable choice.

A reasonable treatment is to consider all the permutations, i.e. compute the BME over all these possible permutations. Only permutations that do not lead to a path the model can traverse by its underlying rules (see Section 2.3.6) and give, by definition, a probability of zero can be excluded. Moreover, further, to not favour any specific one of the remaining permutations, it is reasonable (and statistically correct) to average their BME (see Figure 5.5). I call this workaround a mini-Monte Carlo (mini-MC) approach.

If one assumes that the number n_{ev} of the non-atomic events is bounded by a constant m throughout the whole experiment, one increases computational effort by a factor of $m!$, but the linear complexity of the method in t_{max} as mentioned in Section 5.2 remains preserved. It is reasonable to assume $m \ll t_{max}$, and thus an exhaustive search on only a small scale is employed and does not affect the overall effort significantly.

5.4.1 Synthetic Scenarios

Here, I specify scenario setups to treat the synthetic data set from Section 5.3.2. Figure 5.3 visualizes the randomness of Model 4 with 10 model runs for each of the model versions ($c = 5$ or 15 or 100). I split up my evaluations into three synthetic data scenarios as follows.

Scenario 1: In this scenario, I plug in the true invasion threshold field from Section 5.3.2 (i.e. the field $T_{e,syn}$ used to generate the synthetic data set) for all 3 model versions (visualization in Figure 5.3 (b)) and evaluate BME with the MFP on the atomic synthetic data and the non-atomic synthetic data (i.e, with 2, or 3, or $6 - $ step
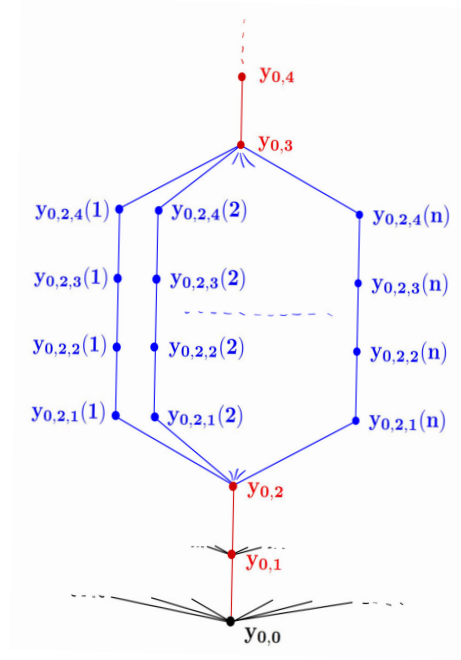
Figure 5.5: Schematic for the workaround for non-atomic data steps. In the experiment path $\mathbf{y_{0,a}}$, the step from $a = 2$ to $a = 3$ consists of 5 atomic events. Each blue path corresponds to one out of $\mathbf{n}$ paths of atomic events leading to $\mathbf{y_{0,3}}$, with $\mathbf{n}$ being the number of possible permutations of the order of the atomic events. (Here, in the schematic it is $\mathbf{n} = 5! = 120$)

jumps). This scenario represents gas-injection experiment repetitions in the same sand pack without any disturbances to the setup (ideally).

Scenario 2: In this scenario, I draw an ensemble of 1000 invasion threshold fields by adding small, random noise to the true invasion threshold field ($T_{e,syn}$). Then, I plug each of these fields into the 3 model versions (visualization in Figure 5.3 (c)) for both the atomic and non-atomic synthetic data (with 2, or $3 - $ step jumps). This scenario represents gas-injection experiment repetitions in the same sand pack with smoothed-out local heterogeneities or disturbances, e.g. due to grain re-arrangement during the injection of gas.

Scenario 3: This scenario involves an ensemble of 1000 independent random invasion threshold fields, each of which is plugged into the 3 model versions (visualization in Figure 5.3 (d)) for both the atomic and non-atomic synthetic data (with 2, or $3 - $ step jumps). This scenario represents gas-injection experiment repetitions, where the sand is repacked after each experiment.

5.4.2 Real Data Scenario

For the real data, I use the longest sub-sequence of the real-experimental data with non-decreasing $n_\text{invasions} \geq n_\text{re-invasions}$ number of invaded gas blocks (7 steps between image number 239 and 246), which excludes the third and fourth problem in the data mentioned in Section 5.3.1. Within that sub-sequence, the workarounds can be implemented without computational difficulties.

When using the real data sequence, I use a setup similar to Scenario 3 of Section 5.4.1 with 7000 random invasion threshold fields. The difference is that I now use Model 4 with the ability for re-invasions (recall that Section 5.4.1 uses Model 4 without Equation 2.8) so that they can better resemble the real data set, which belongs to the discontinuous gas flow regime (see Section 2.1). An immediate evaluation of these models leads to BME=0 for almost all invasion threshold fields; because of its deterministic re-invasion decision (rule specified in Equation 2.8), the model wants to re-invade a wrong block and is punished with complete Bayesian rejection. Theoretically, the BME value of 0 is correct, but it has no practical significance.

The focus of this case-study is primarily method development and not model development. Therefore, I probabilistically change the model. I assign a 90% probability to the model's decision to re-invade the block obtained from the rule specified in Equation 2.8 or not re-invade any block. The remaining probability of 10% is uniformly distributed among the other blocks of the gas cluster for the re-invasion of water. That means any block of the current gas cluster can be re-invaded with a probability of at least $\frac{0.1}{n_\text{gas,cluster}}$, see Figure 5.6. Note that $n_\text{gas,cluster}$ only accounts for the blocks in the respective cluster. Also, I have to treat the injection cluster differently as it has one less choice since the injection block cannot be re-invaded.

I also need to adjust the workaround for the non-atomic data (Figure 5.5) because I now have a re-invasion rule in the models. To do that, I combine the different orderings of re-invasions with the orderings of invasions from before and leave the rest of the non-atomic modification unchanged. Note that an atomic time-step may also have no re-invasion at all, since $n_\text{invasions} \geq n_\text{re-invasions}$. The total number of orderings is then $n_\text{orderings} = (n_\text{invasions}!)^2/(n_\text{invasions} - n_\text{re-invasions})!$. For example, a combination of non-atomic events with 5 invasions and 2 re-invasions leads to 2400 different orderings,
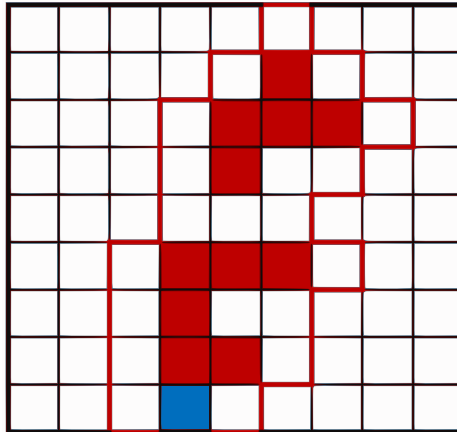
Figure 5.6: Illustration of the modification to tackle the second challenge in data from Section 5.3.1, where water re-invasion in gas-occupied blocks occur **not** according to the model's choice (guided by Equation 2.8): The blue block marks the injection block. The red blocks are gas-occupied. In this example, the top gas cluster has a probability of $\frac{0.1}{n_{\text{gas,top}}} = \frac{0.1}{5}$ and the injection cluster has a probability of $\frac{0.1}{n_{\text{gas,injection}}} = \frac{0.1}{6}$, for a re-invasion of water in the respective cluster.

which happens to be the maximum number for the real-data sequence used in this case-study.

5.4.3 List of Algorithmic Steps[†]

Before I discuss the results from my case-study, I summarize the general algorithmic steps of the MFP. These steps are the same for all models obeying the Markov Chain property combined with exact data (knowledge of each atomic event).

(1) List all possible events in the data, both reproducible and non-reproducible, by the model. For example, in the case of the demonstration case-study, the non-atomic events of the data fall under the model non-reproducible events category.

(2) State the formula for the probabilities of events being executed by the model. These could be individual, fixed values, evaluations of a probability distribution function or a combination of both. In this case-study, it is stated by Equation 5.8.

[†]The code implementation of the method of forced probabilities was done by my co-author Mr. Peter Walter as part of his Bachelor thesis (BSc. SimTech) and Masters Project (MSc. SimTech Projektarbeit) at the University of Stuttgart.

(3) In the original model code, code a new update rule to force the next model state, similar to a restart capability of a code.

(4) Propagate and accumulate probabilities through all time steps, i.e. a simple multiplication. At this stage, a possible code break-off criterion can also be included to identify and flag zero-probability events.

The implementation of the MFP code is mostly non-intrusive because no re-writing of the code is necessary. However, step (3) requires good restart abilities of the model code with forced model states per time step. Also, the simplest way to achieve step (2) is to add a line to the original code that outputs the probability of the forced event.

5.5 Results and Conclusions from the Case-Study

Now, I discuss the results obtained from the case-study. Table 5.1 contains the BME values on a negative logarithmic scale (the smaller these values are, the better the model) obtained using MFP on Model 4 for both synthetic data as well as real data.

5.5.1 Results from Synthetic Data Scenarios

In both Scenarios 1 and 2, the model version with $c = 15$ has the best BME values (see bold font in Synthetic Scenario 1 and 2 of Table 5.1). For Scenario 1, this is expected because this model version and threshold field were used to generate the synthetic data. For Scenario 2, the threshold fields were close to the synthetic data setup; therefore, the correct model version still had the best BME value. Also, according to expectations, all the model versions had significantly worse BME values for Scenario 3, where entirely random entry threshold fields were used. However, the ranking also changed, and the more random model version ($c = 5$) emerged as the best model in Scenario 3.

Why Does the Model Ranking Change for Scenario 3?

Let us first look at the two extreme model versions to understand why the ranking changes. The model version with $c = 100$ is almost deterministic in its choice of a

Table 5.1: Table containing the BME values obtained in the three synthetic scenarios and the real scenario on a negative logarithm scale, the ensemble sizes n_{MC}, number of atomic events n_{ev} occurring within a non-atomic step and, computed Bayes factors $\text{BF}_{\frac{k2}{k1}}$. Note, here the model versions $(k1, k2)$, are denoted by their respective c values. The best-performing model is highlighted with bold font $-\ln \textbf{BME}$ value.

Scenario		n_{MC}	n_{ev}	$c = 5$	$c = 15$	$c = 100$	$\text{BF}_{\frac{15}{5}}$	$\text{BF}_{\frac{5}{100}}$	$\text{BF}_{\frac{15}{100}}$
Synthetic	1	1	1	3034.6	**2672.3**	3063.3	2.6e157	3.0e12	6.1e169
			2	3099.9	**2741.0**	3124.6	7.5e155	5.3e10	4.0e166
			3	3169.8	**2817.5**	3202.3	9.7e152	1.3e14	1.3e167
			6	3301.9	**2961.8**	3345.5	4.8e147	9.1e18	4.4e166
	2	1000	1	3201.2	**2931.1**	3474.1	2.1e117	3.4e118	7.1e235
			2	3246.7	**2972.1**	3496.0	1.7e119	2.0e108	3.4e227
			3	3292.6	**3013.2**	3519.0	2.3e121	2.1e98	5.0e219
	3	1000	1	**5942.7**	6647.7	8461.9	6.4e − 307	1.2e1094	8.0e787
			2	**5942.1**	6644.5	8453.3	9.0e − 306	3.9e1090	3.5e785
			3	**5939.6**	6638.3	8439.8	3.6e − 304	7.0e1085	2.5e782
Real		7000	3 − 5	**269.22**	294.29	336.40	1.3e − 11	1.5e29	1.9e19

gas pathway, which is different for each invasion threshold field. This is why this model version can get good BME values (small $-\ln BME$) if and only if the invasion threshold field closely matches the true field $(T_{e,syn})$, which is highly unlikely when one uses entirely random invasion threshold fields. If this is put colloquially, the few good predictions of the $c = 100$ model version do not make up for the many bad ones. The more random ($c = 5$) model version is not as deterministic in its choice of the gas pathway as $c = 100$ is, and so, it is largely unimpaired by the choice of the invasion threshold field. This is why the random model version ($c = 5$) achieves mediocre values for any invasion threshold field. Thus, in the scenario where the invasion threshold field is highly uncertain, it has an advantage that helps it emerge as the best model version in Scenario 3. The model version with $c = 15$ is not identified as the best model when uncertainty in the threshold field is increased. This indicates that the entry threshold field is a highly sensitive and important parameter for Model 4 to function correctly.

Effect of Non-Atomic Synthetic Data

The introduction of non-atomicity in the synthetic data does **not** change the ranking of the models in any scenario (see, $-\ln$BME values for n_{ev} values other than 1 for Synthetic Scenarios (1, 2, and 3) in Table 5.1) but makes it slightly less decisive in comparison to $n_{ev} = 1$ for all the synthetic scenarios of Table 5.1. This coincides with the synthetic data set becoming, in a sense, weaker or less informative if parts of it are unknown in ordering. This is visible in Table 5.1 as, despite the general rise of $-\ln$ BME values with increasing n_{ev}, their differences become slightly smaller. Looking at the Bayes factors between the competing models makes it easier to see this effect: they generally decrease with increasing n_{ev}. There are only a few exceptions to this observation. For example, the Bayes Factors $\text{BF}_{\frac{15}{5}}$ between the models in Scenario 2 increases with the increased non-atomicity in the synthetic data. However, looking at the orders of magnitude of the values in comparison, it can be safely concluded that this does not affect or change the level of decisiveness.

5.5.2 Results from Real Data Scenario

Initially, I evaluated the model versions on the complete real data set. This helped gather information on the magnitude of the effect of the challenges in the real data for implementation of MFP, as discussed in Section 5.3.1. It is noticed that non-atomic events with a very high number of events n_{ev} are pretty common in the data set, which leads to very high computation time for the mini-MC workaround explained in Section 5.4, thus making a BME evaluation infeasible even with MFP.

The events of wrong block re-invasion (the second problem in data discussed in Section 5.3.1) in the data set are plenty, but I am able to tackle them with the workaround mentioned in Section 5.4.2. In the later time-steps of the data, block invasion in non-gas injection clusters (third problem in data discussed in Section 5.3.1) or events with decreasing numbers of invaded gas blocks (fourth problem in data discussed in Section 5.3.1) are predominant. However, I have no fix to this problem in the real data set.

Thus, I decide to look for a sub-sequence of time steps in the data that aligns with the model's assumptions and has a reasonably small number of non-atomic events (for

reasonable computation time of mini-MC runs, see Figure 5.5). The resulting sequence of time steps in the data is the one mentioned in Section 5.4.2. For that sequence, $-\ln\text{BME}$ is between 269 and 360 for the probability of correctly predicting seven steps, which is a small probability already. This is not a fault of the MFP but of the match between the models used and their corresponding data set of this study.

Regarding the ranking of the model versions, one sees a similar pattern as in the synthetic Scenario 3. The best model version is the one with $c = 5$, followed by $c = 15$ and then $c = 100$ (see Row: Real from Table 5.1). The uncertainty in the invasion threshold fields is handled better by a random (c=5) model than by the more deterministic models. Therefore, more information about the invasion threshold fields is necessary for these models to accurately predict the gas path under the experimental data's conditions and scale.

5.5.3 Conclusions

In conclusion, my method MFP makes it possible to calculate BME for Markov-Chain type models and discrete atomic data in previously impossible cases. The method works well, is mostly non-intrusive to the model and has a linear computational cost. Also, my method enables a fully Bayesian assessment of a macroscopic IP model for the first time.

In my case-study, the method was demonstrated only on a relatively small sequence of real data. This is because the large distance between the model outputs and the real data leads to many zero-probability events. So, for more conclusive results, better models or more-informative data are required, i.e. data with no or few non-atomic events and an improved Model 4.

When I use MFP to evaluate the BME for imperfect models or data or both, resulting in practically futile BME values (BME = 0), I can adapt my approach and use MFP to detect events leading to such values in the model and the data by flagging them. This exercise helps determine the structural errors in the model or the mismatch between the model concepts and the observations.

Summarizing the results from the implementation of MFP on Model 4 and gas-injection experimental data, I can conclude that both the model and the experimental data have

a scope for improvement. The rules in Model 4 could be updated by looking at specific types of events, e.g. the ones that get the model rejected or result in poor performance (like the deterministic re-invasion events in the current version). The experimental data technique processing could be updated to have more discrete and atomic data steps. However, experimental data or model improvement is beyond the scope of this study.

6 Summary, Conclusions and Outlook*

Looking back at the introduction of my thesis, there are many challenges involved in testing macroscopic IP models in the presence of data. I systematically contributed towards overcoming these challenges using three research questions (**RQ**s).

RQ1: *"How to appropriately compare time-ignorant macroscopic IP models to time-dependent experimental image data?"*

Contribution 1: *An appropriate method to compare time-ignorant macroscopic IP models to the time-dependent experimental image data is: volume-based time matching followed by computing the (Diffused) Jaccard coefficient to assess the quality of fit.*

To treat the challenge of the time-ignorance of IP-type models in **RQ1**, I implemented a volume-based time matching between experimental images and model output images. Once the model outputs were aligned with respective experimental images on the time axis, I computed the Jaccard coefficient to quantify the similarity between the experimental and model images (answering the **RQ1**). Traditional comparison of images based on perception is neither quantitative nor objective and can be extremely tedious. In contrast, the Jaccard coefficient is both quantitative and objective, and its evaluation can easily be automated. While the Jaccard coefficient quantifies a pixel-by-pixel agreement between images and is close to a "measure of perception", I introduced blurring in the images to compute the Diffused Jaccard coefficient. This blurring of images allows one to compare models and experiments across various levels of detail in the data, thus allowing comparisons across multiple scales. When I compared the results from my proposed method with that obtained using the traditional spatial-moments comparison method, the latter turned out to be less intuitive and sometimes misleading. The Diffused Jaccard coefficient can be seen as sliding between rigorous pixel-by-pixel

---

*This chapter contains text fragments from my publications Banerjee et al. [2021], Banerjee et al. [2023] and Banerjee et al..

assessment to aggregated (blurred) assessment over space as done in spatial moments. The advantage is that a single insightful number is available for ranking, and this slider (over the blur radius) can be used for model investigation and improvement. The most meaningful blur radius for a specific application has to be decided by the user so that it reflects the intended purpose of identification, e.g. in an application of identifying the radius of a gas contamination zone in the subsurface to protect the groundwater table, a relatively high blur radius can be used. The method can be extended to any application involving high-resolution model output and experimental data as raster images. Further, this metric can be used for model calibration (identification of best-fit parameter values) and for comparison of alternative model types.

RQ2: *"Using the comparison approach developed in research question 1 on the different macroscopic IP model versions, how to determine which model version is better at describing which of these gas-flow regime experiments? Can specific deficits and recommendations be derived?"*

Contribution 2: *The inter-comparison of competing macroscopic IP model versions identifies "suitable"and "less adequate"models for the transitional and continuous gas-flow regime experiments for the first time. This comparison process also highlights the models' strengths and weaknesses.*

To answer **RQ2**, I compared four competing macroscopic IP model versions against nine experiments belonging to the transitional and continuous gas flow regimes, using the tool developed to answer **RQ1**. These models were tested for transitional and continuous gas-flow regimes for the first time. To test the models with a different detailed level of information in the data, I used three different blur-radii to compute the Diffused Jaccard coefficient for assessing the model-data fit. On the one hand, I could distinguish that certain versions of the macroscopic IP models are unsuitable for use in transitional and continuous gas flow regimes, even with high levels of blurring in images. On the other hand, I could identify macroscopic IP-model versions that are suitable for the transitional gas flow regime and have the potential to be used in continuous gas flow regime if further research towards refinement of their rules for gas-invasion, water-re-invasion, finger branching and so on are done. For example, in their present state, I recommend the use of macroscopic IP Models 3 (with > 1 block invaded per step; Section 2.3.5) and 4 (with a stochastic modification of the gas-invasion rule; Section 2.3.6) with high blurring (i.e. with large blur radius) for large-scale applications

in the continuous gas flow regime, where the details of the gas-cluster structure are insignificant. Besides, I identified that the structure of the T_e field is a critical input for the good performance of these models. Further, in the absence of a good fit of the structure of T_e field to the original experimental porous medium, the more flexible models (e.g. Model 4 with low c values, see Section 4.3.1) fare well. I discovered that these models are not fit for calibration of parameters like gas saturation as long as there is a dominant uncertainty in the T_e fields.

RQ3: *"How can we efficiently compute Bayesian Model Evidence for extremely large data sets like highly space-time resolved image data, knowing that all existing computational algorithms would be computationally infeasible? If yes, can we pinpoint very detailed strengths and weaknesses of the models?"*

Contribution 3: *The method of forced probabilities (MFP) is an effective technique to compute Bayesian model evidence for models following the Markov-chain property and complete data.*

There are challenges involved in computing Bayesian model evidence for IP-type models with binary outputs and extensive space-time-resolved image data. This limits using the Bayesian model selection framework for the inter-comparison of the different IP-type model hypotheses if no - potentially misleading - approximation methods shall be applied. Therefore, to answer **RQ3**, I developed the MFP to calculate BME for models with Markov-Chain property (like IP-type models) and discrete detailed atomic data in previously impossible cases. In this method, I replaced numerous forward runs of the model (to compute BME using numerical methods) with a single analytical equation developed, taking the Markov property into account. The method works well, is primarily non-intrusive to the model and has a linear computational cost. Under certain conditions, my method enabled a fully Bayesian assessment of an IP-type model and an elaborate gas-injection experimental data set, which was impossible before. By testing the MFP on an IP-type model, I confirmed some conclusions of my earlier model inter-comparison study (answer to **RQ2**): e.g. the importance of T_e fields on an excellent performance of the models. Going beyond the findings from my model selection study (answer to **RQ2**), using MFP, I detected and flagged events in the model that caused a mismatch with the data. Information about such events is, in general, helpful in determining the mismatch between model concepts and observations,

which is essential to develop more accurate model formulations and experimental data-processing techniques. MFP, in the current stage of development, is applicable for models with Markov Chain property and complete noise-free observation data.

Through my thesis' contributions, I enabled the testing of IP-type models in the presence of experimental data for gas flow in saturated porous media. I addressed the uncertainty in modelling these systems by enabling a Bayesian assessment. In these models, this allowed detection of the uncaptured or incorrectly captured gas flow processes in the saturated subsurface, thus paving the way for future refinement of the model rules and parameters.

To use these models in flow regimes, where viscous effects cannot be ignored, the model rules must be redefined. A possible extension could be a mix of Model 3's rule of invading more blocks per step combined with a stochastic invasion rule similar to that of Model 4. The rule for this extension would also need to be adapted to closely mimic the gas flow behaviour in the continuous flow regime, e.g., with finger invasion rules enabling the growth of multiple parallel thick fingers. For using the models in capillary-dominated flow regimes, to accurately represent the water re-invasion processes, a probabilistic re-invasion rule instead of a deterministic one is recommended. Also, I recommend that the refinement of models be executed bearing not only the flow regimes but also the scale and the purpose of application in mind.

Simultaneously, through my analyses, insights into experimental methods were also obtained. For example, improved detection limits in experiments could prevent observations: (1) tunnelling of gas pixels into non-neighbours of the injection gas cluster (2) the non-increasing gas pixels between images at successive time steps, in the data (Chapter 5).

The results of my thesis and the obtained conclusions stimulate future areas of research:

- Efforts are needed towards reducing the uncertainty of the invasion threshold (T_e) fields used as input to the models. At the scale of the experiments used in this thesis, it is impossible to determine the exact structure of the invasion threshold field. One strategy for accounting for the uncertainty of the geological heterogeneity in the experimental setup is to run the corresponding IP model over multiple realisations of the T_e field [Trevisan et al., 2017]. The other strategy is

to investigate and identify the T_e fields' underlying structure, e.g., using geostatistical inversion methods. The comparison metric (Diffused Jaccard coefficient) can identify the "good performing"T_e fields for each model type. One could then operate a (geostatistical) Bayesian inference to estimate (or conditionally simulate) the T_e fields, e.g., using Markov chain- Monte Carlo (MCMC) methods for random fields [Xu et al., 2020], a parameter Ensemble Kalman filter (EnKf) (e.g., Kalman Ensemble generator by Nowak [2009]) or transformed versions [Schöniger et al., 2012a].

- The MFP, in its current stage of development, requires that the data be noise-free. A possible direction of research is modifying MFP to apply to noisy data (e.g. with statistical assumptions on the distribution of black/white detection errors). A straightforward idea would be to perturb the available data with several realisations of randomly generated noise and then handle each realisation with my method. However, this multiplies computational costs by a substantial factor to host these repetitions.

- The tools I developed in my thesis are not limited to gas flow in water-saturated porous media systems. The Diffused Jaccard metric can be extended to model calibration and model comparisons for multiphase (other than gas-water) flow regimes in porous media and, again, in any other discipline that works with raster model output and data. The MFP can be applied to gas (fluid) migration in fractured-porous media under the conditions of Markov-style model formulation and complete observations (e.g. in thin slices or with high-resolution 3D micro-tomography). It can also be applied to systems involving experiments and models at the microscopic scale, where appropriate monitoring techniques resolve individual pores [e.g., Gao et al., 2021]. Other than multiphase flow applications, MFP can be used in applications such as counting processes (e.g. as in traffic), discrete computerised systems (e.g. network traffic), probabilistic Markov-style model-based river water quality monitoring [González-Nicolás et al., 2021], tracer experiments / Lagrangian movement (e.g. fluorescent microparticles to monitor turbulent flow [Adrian, 2005]), stochastic models for discrete, dynamic systems and complete observation (e.g. chemical reaction modelling), statistics-based data-driven soil-plant-atmosphere modelling [Gong et al., 2013] and micro-seismic modelling [Shapiro, 2008] to name a few.

Modelling a physical system is the art of mathematically formulating our understanding of such systems. Comprehensive testing of a class of models against observations helps confirm or dismiss our concepts and beliefs regarding the system's behaviour. My thesis is an effort to confirm, clarify, and update the concepts of gas flow behaviour in the subsurface.

A Appendix to Chapter 2

Image-Data Processing

Here, I elaborate on details of the image processing technique for the experimental data described in Section 2.2. The following details are adapted from Van De Ven and Mumford [2019] and Van De Ven et al. [2020].

Each pixel of a grey-scale image obtained using the light transmission technique [Tidwell and Glass, 1994], has an intensity value for the transmitted light. A group of pixels is considered a block of a chosen discretization scale, and the mean of the intensities of all the pixels contained within a block is assigned as intensity value per block. In this way, the images are discretized as blocks of averaged intensity values. Thereafter, either the gas saturation data or the optical density (OD) data for detecting the gas presence is calculated as follows.

In this thesis, I have used the OD values to obtain gas presence/absence type image data. To calculate the OD per block from the light intensity values of the block-averaged greyscale image, Equation A.1 is used from Kechavarzi et al. [2000]:

$$OD = -\log_{10}\left(\frac{I}{I_{sat}}\right). \tag{A.1}$$

A detection limit for OD is calculated based on the variance of a zone of the experiment that is known to not contain any gas throughout the experiment. The blocks where the OD values exceed the detection limit are considered gas-occupied at a certain saturation value [Van De Ven and Mumford, 2019].

If one wants to convert the light intensity values from the grey-scale images to liquid saturation data, a few methods are proposed by Niemet and Selker [2001]. I list method

C from Niemet and Selker [2001] because its underlying assumptions fit the experimental conditions of this thesis. This method is proposed for homogeneous sands where pores drain independently, randomly and completely. The water-solid contact angle is assumed as zero degrees. Additionally, it is assumed that, after wetting, a film of liquid remains on the surface of the solid grains. Hence, the available pore space is the space in between the water films. Based on these assumptions, the effective saturation S_{eff} between complete and residual water-saturated images can be calculated using Equation A.2:

$$S_{eff} = 1 - \frac{\ln\left(\frac{I}{I_s}\right)}{\ln\left(\frac{I_{res}}{I_{sat}}\right)}, \tag{A.2}$$

where I is the intensity of light transmitted through the medium per block, I_{sat} and I_{res} are the intensities of light transmitted through a completely water-saturated image and an image with residual saturation of water, respectively [Niemet and Selker, 2001]. The gas saturation S_g can be evaluated from the effective saturation using Equation A.3, where S_w is the actual water saturation and S_{res} is the residual water saturation in the experiment. Measurement error for gas saturation is calculated based on the variance of wetting saturation (S_w) in a zone of completely water-saturated pixels, i.e. where the expected $S_w = 1$.

$$\begin{aligned} S_w &= S_{eff}(1 - S_{res}) + S_{res} \\ S_g &= 1 - S_w \end{aligned} \tag{A.3}$$

B Appendix to Chapter 4*

I present more visual evidence from my analyses supporting the results and conclusions from Sections 4.3.1 — 4.4. Figure B.1 contains the experimental images and their blurred versions for experiments 10-B, 100-B and 250-B.

Figure B.2 contains the experimental images and their blurred versions for experiments 10-C, 100-C and 250-C.

This is followed by corresponding best-fitting model realizations obtained using the maximum Jaccard coefficient for these experiments (Figures B.3 and B.4).

The best-fitting model realizations to the experimental triplicate at 10 ml/min, 100 ml/min, and 250 ml/min, obtained using the maximum Diffused Jaccard coefficient (low) metric, are shown in Figures B.5 - B.7.

Figures B.8 - B.10 contain the best-fitting model realizations to the experimental triplicate at 10 ml/min, 100 ml/min, and 250 ml/min, obtained using the maximum Diffused Jaccard coefficient (med) metric.

The best-fitting model realizations to the experimental triplicate at 10 ml/min, 100 ml/min, and 250 ml/min, obtained using the maximum Diffused Jaccard coefficient (high) metric, are shown in Figures B.11 - B.13.

---

*This appendix contains figures from the Supporting Information to my publication Banerjee et al.
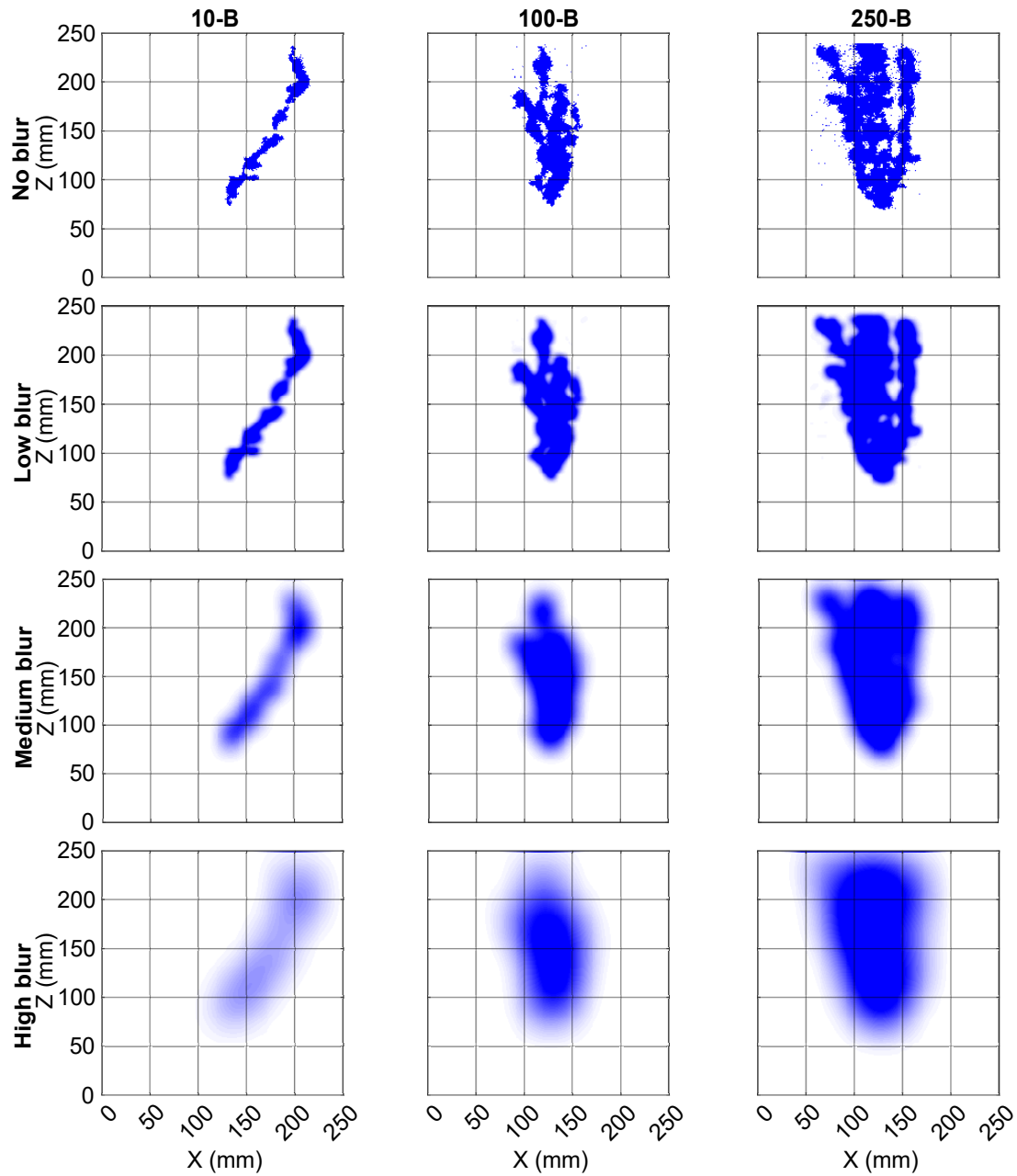
Figure B.1: Final experimental image of the experiments 10-B, 100-B and 250-B. Row 2-4 contains the blurred version of the images of Row 1 for the three different blur-radii.
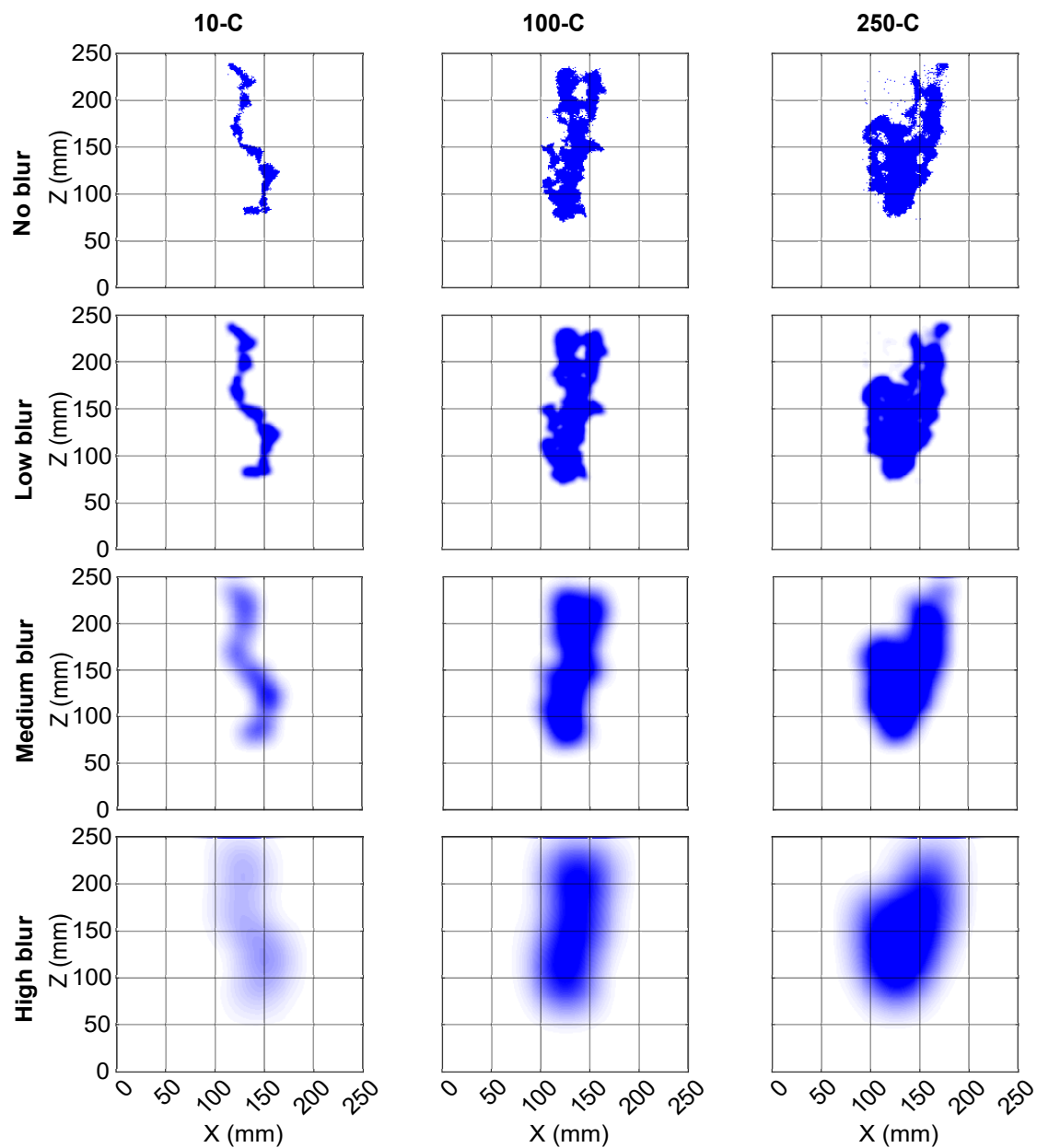
Figure B.2: Final experimental image of the experiments 10-C, 100-C and 250-C. Row 2-4 contains the blurred version of the images of Row 1 for the three different blur-radii.
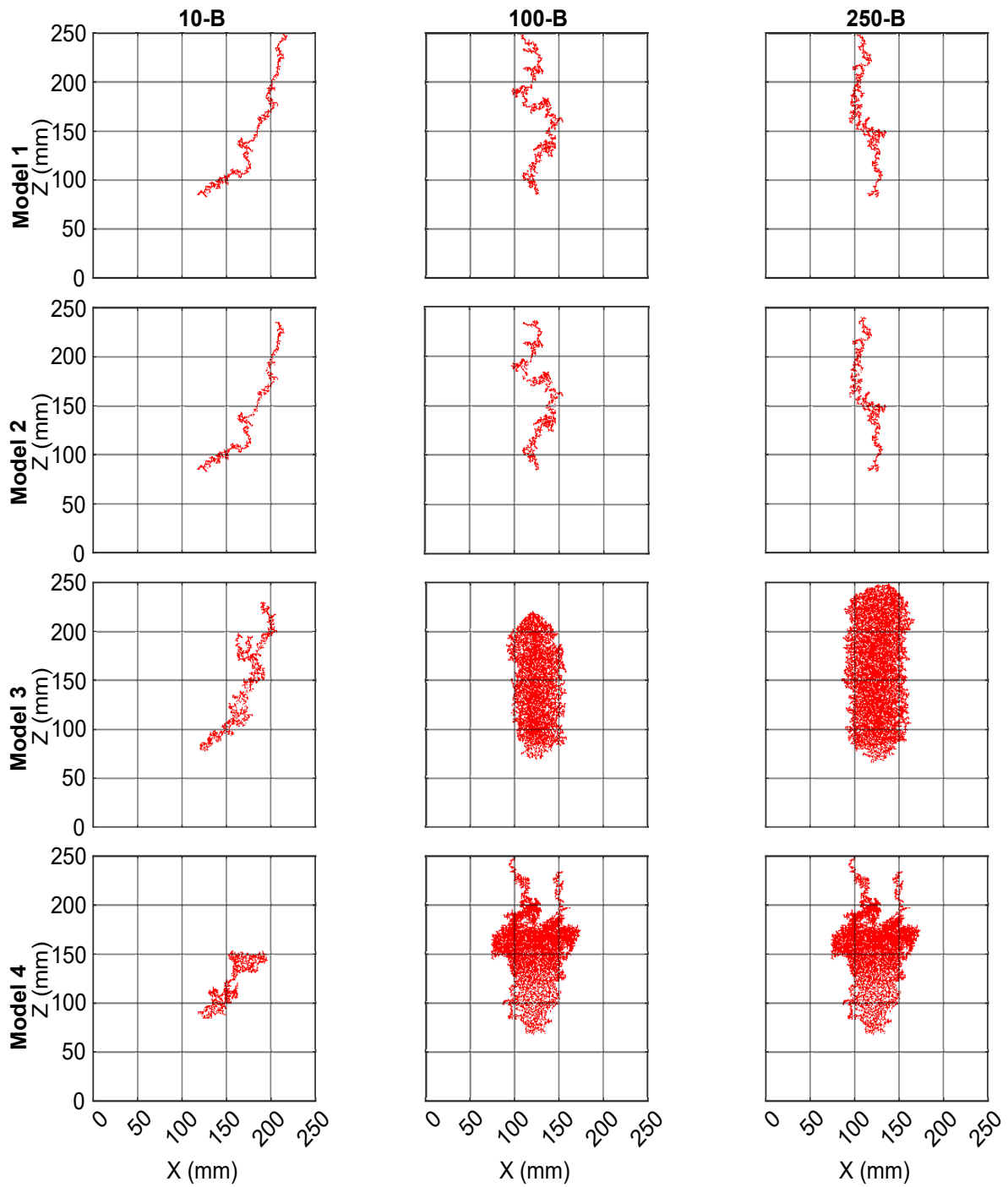
Figure B.3: Model images for the different model versions with the best fit to non-blurred experimental images (with highest Jaccard value) from experiment no. 10-B, 100-B and 250-B. Row 1, Row 2, Row 3 and Row 4 correspond to Model 1, Model 2, Model 3 and Model 4, respectively.
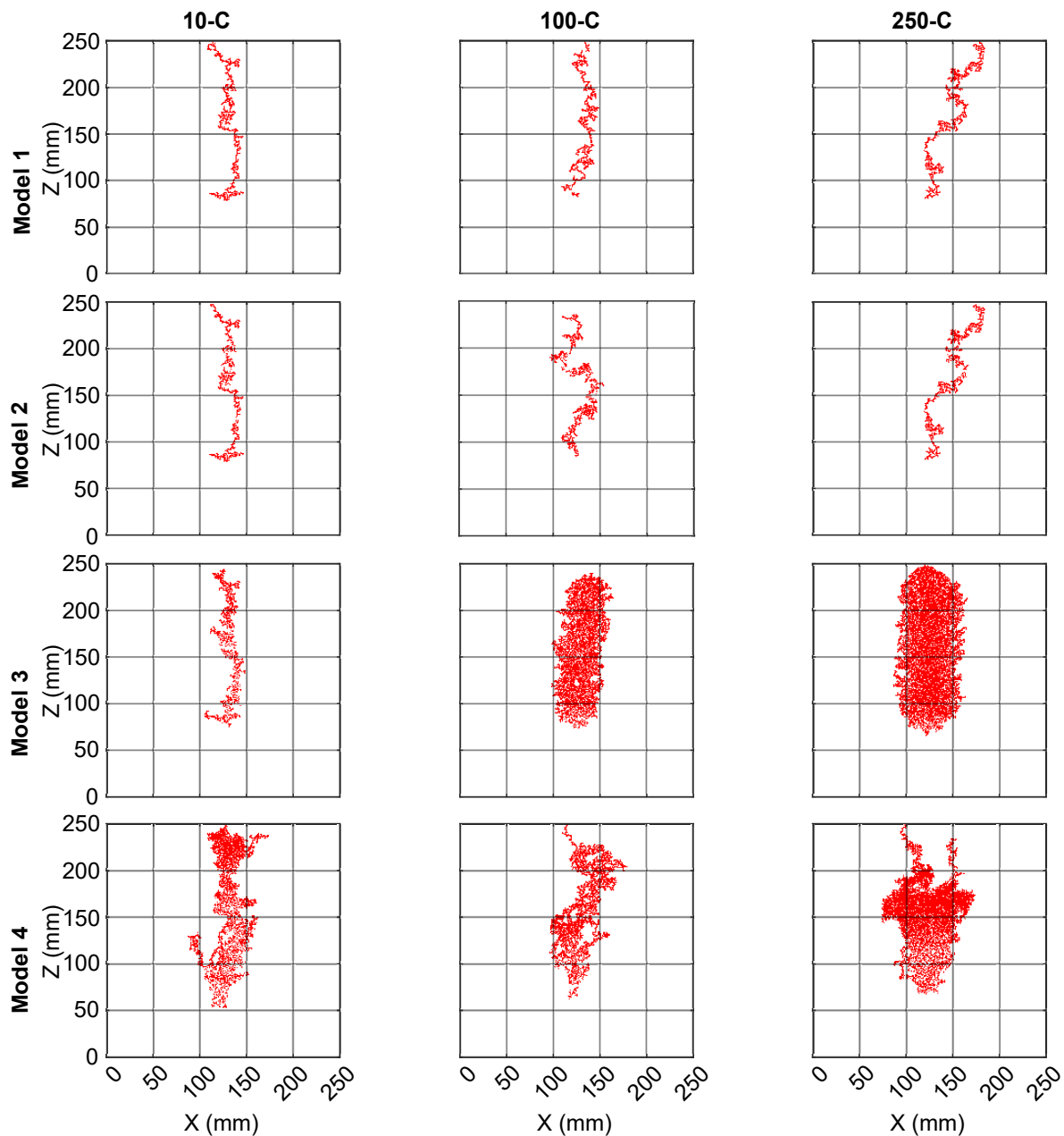
Figure B.4: Model images for the different model versions with the best fit to non-blurred experimental images (with highest Jaccard value) from experiment no. 10-C, 100-C and 250-C. Row 1, Row 2, Row 3 and Row 4 correspond to Model 1, Model 2, Model 3 and Model 4, respectively.
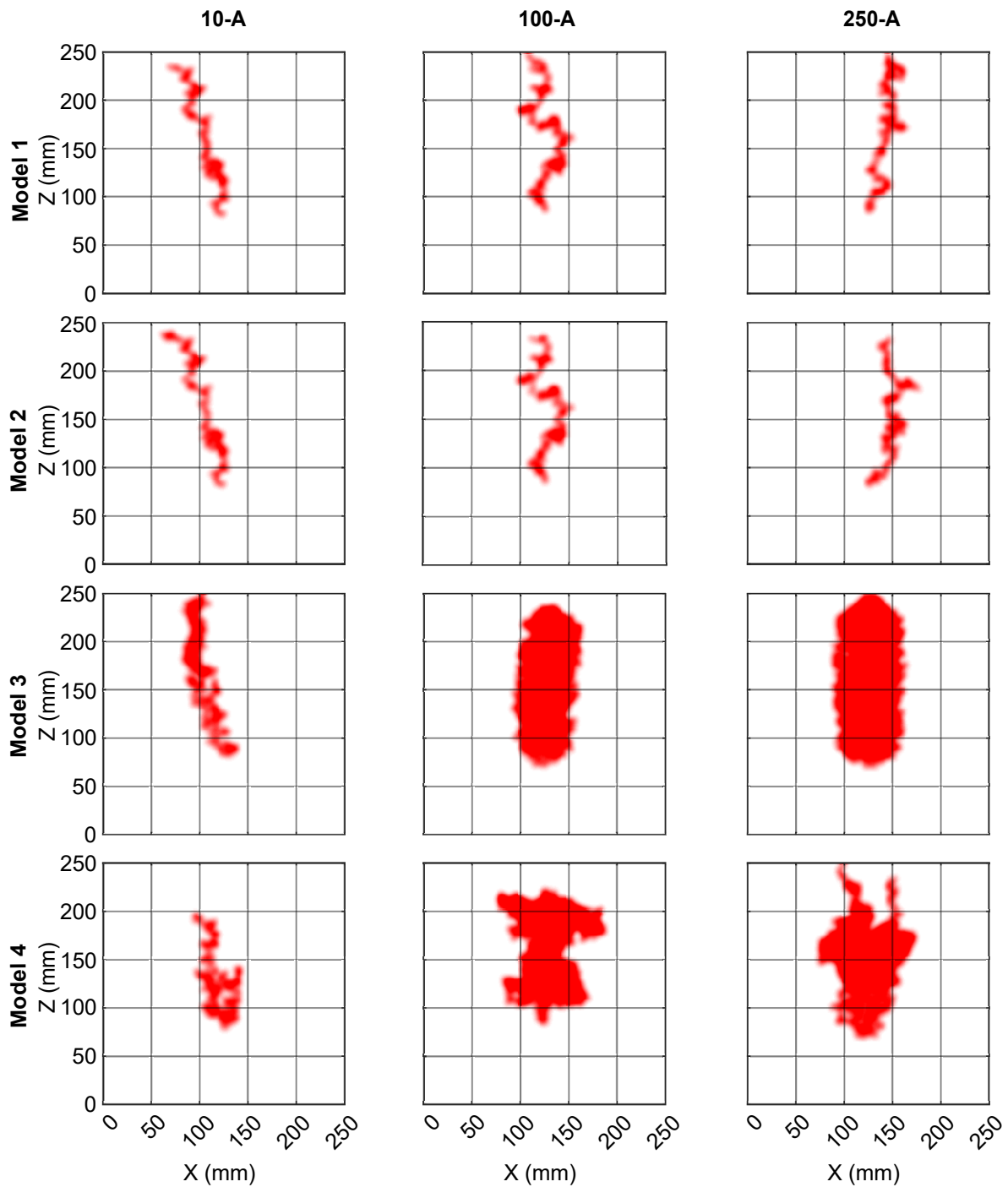
Figure B.5: Model images for the different model versions with the best fit to blurred experimental images (with highest Diffused Jaccard (low) value) from experiment no. 10-A, 100-A and 250-A. Row 1, Row 2, Row 3 and Row 4 correspond to Model 1, Model 2, Model 3 and Model 4, respectively.
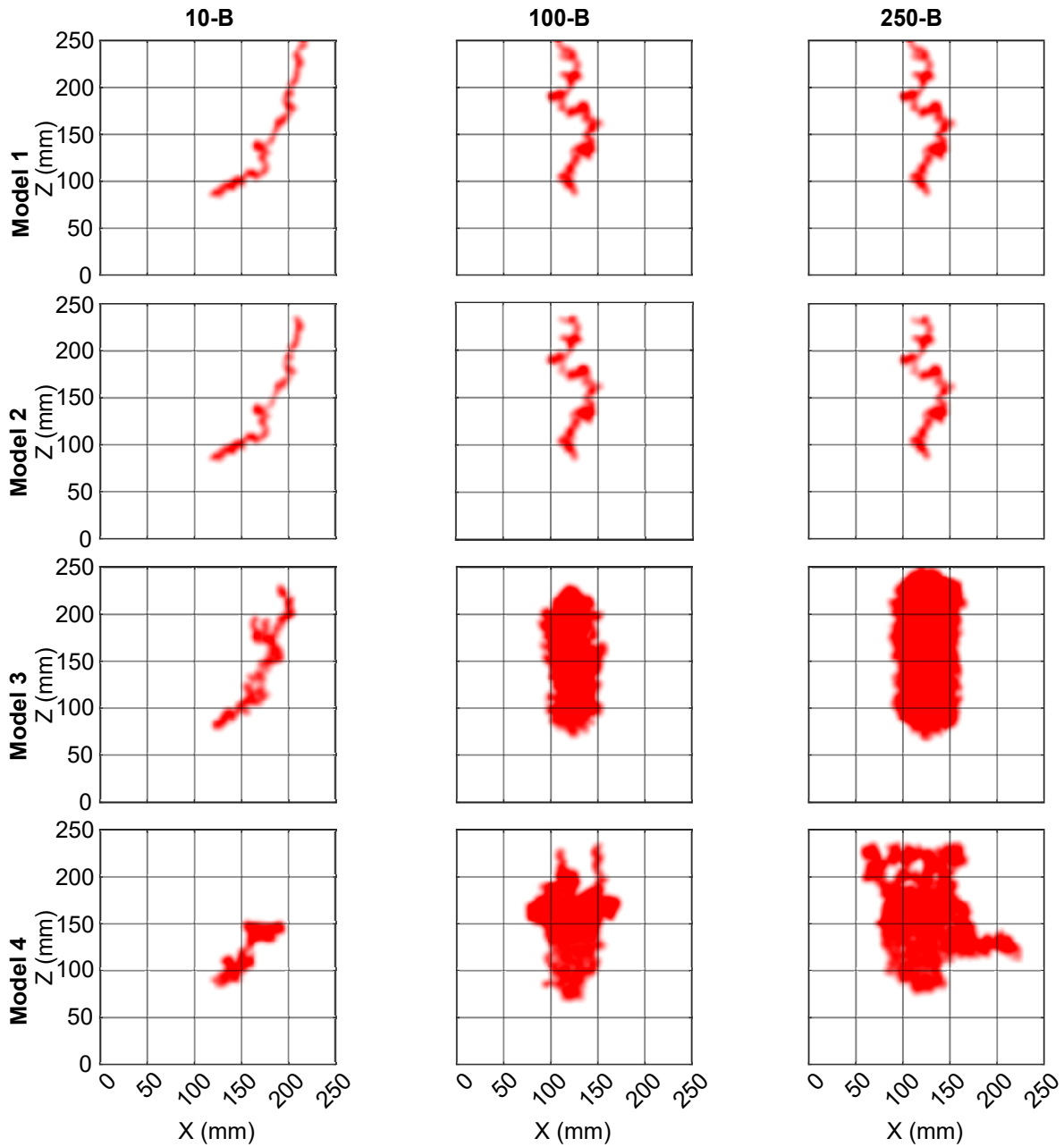
Figure B.6: Model images for the different model versions with the best fit to blurred experimental images (with highest Diffused Jaccard (low) value) from experiment no. 10-B, 100-B and 250-B. Row 1, Row 2, Row 3 and Row 4 correspond to Model 1, Model 2, Model 3 and Model 4, respectively.
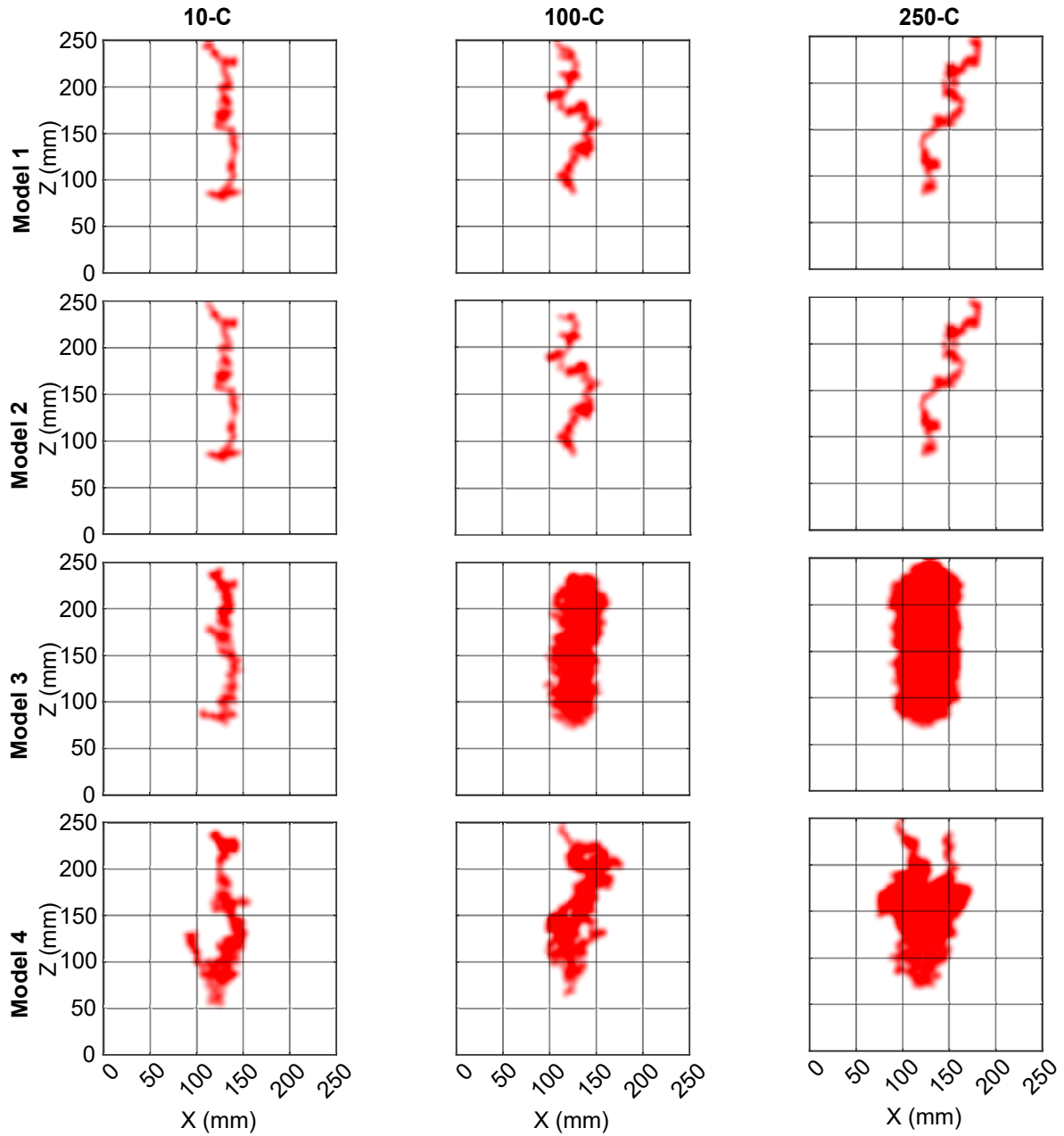
Figure B.7: Model images for the different model versions with the best fit to blurred exper-
imental images (with highest Diffused Jaccard (low) value) from experiment no.
10-C, 100-C and 250-C. Row 1, Row 2, Row 3 and Row 4 correspond to Model
1, Model 2, Model 3 and Model 4, respectively.
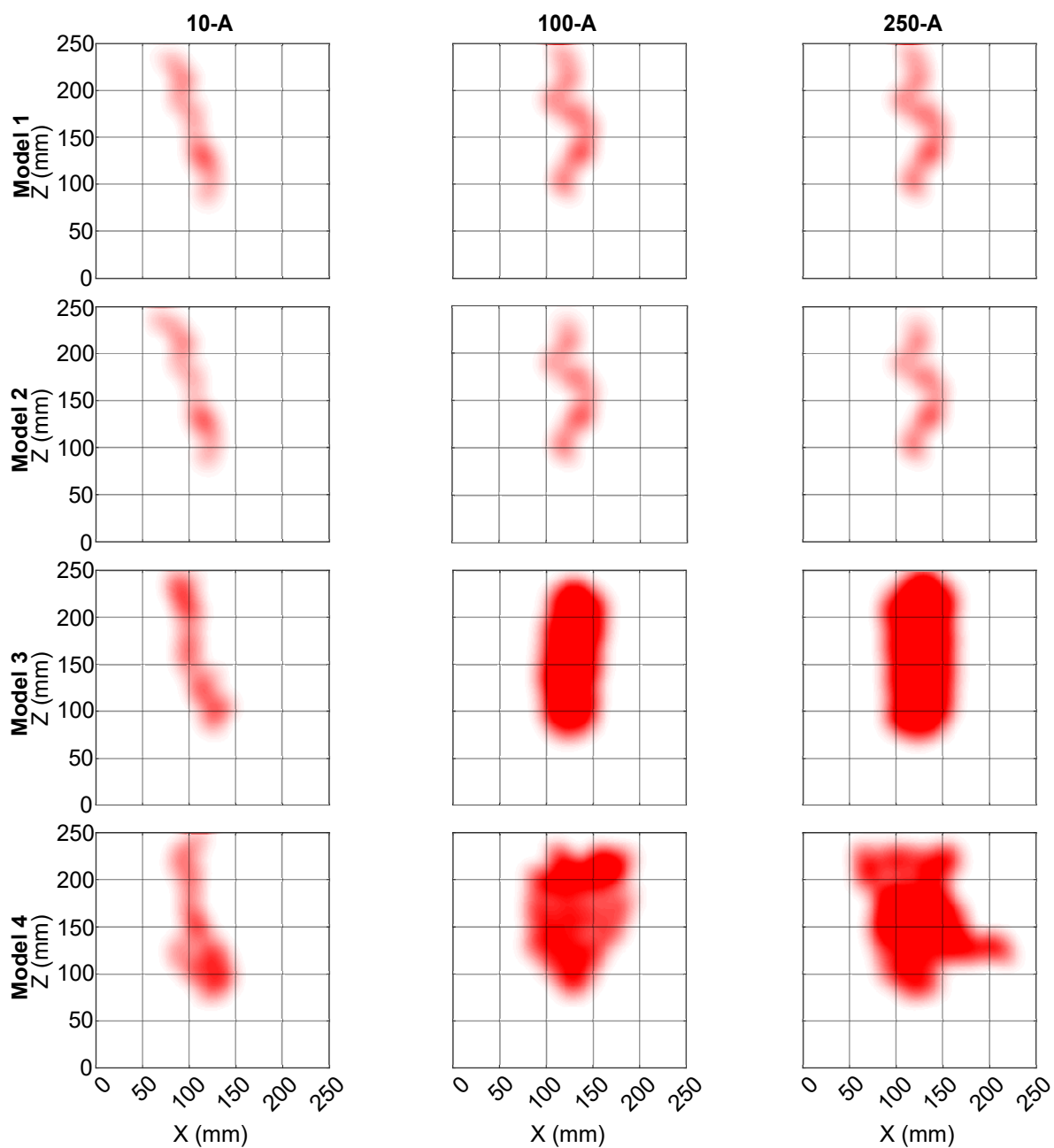
Figure B.8: Model images for the different model versions with the best fit to blurred experimental images (with highest Diffused Jaccard (med) value) from experiment no. 10-A, 100-A and 250-A. Row 1, Row 2, Row 3 and Row 4 correspond to Model 1, Model 2, Model 3 and Model 4, respectively.
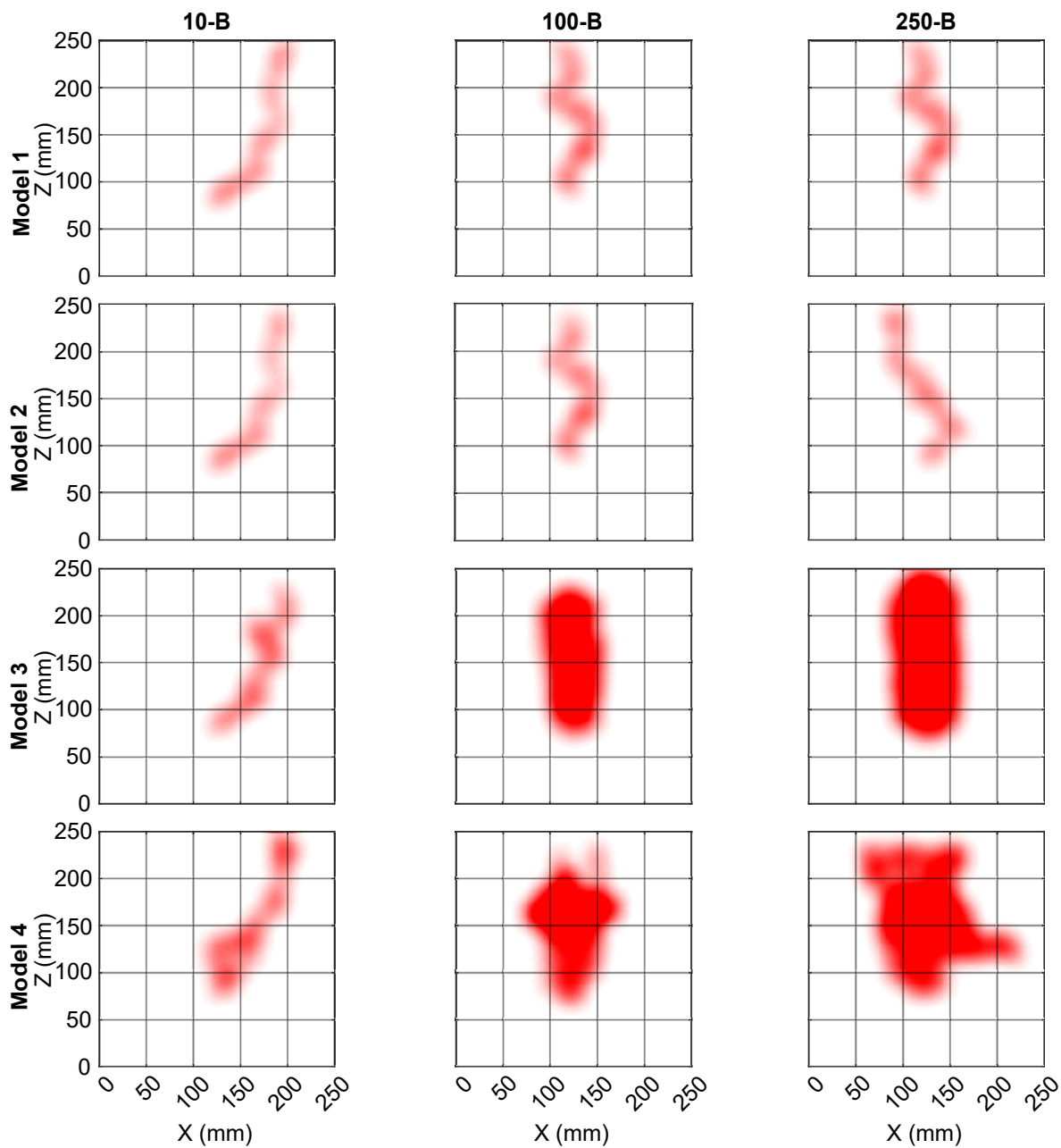
Figure B.9: Model images for the different model versions with the best fit to blurred experimental images (with highest Diffused Jaccard (med) value) from experiment no. 10-B, 100-B and 250-B. Row 1, Row 2, Row 3 and Row 4 correspond to Model 1, Model 2, Model 3 and Model 4, respectively.
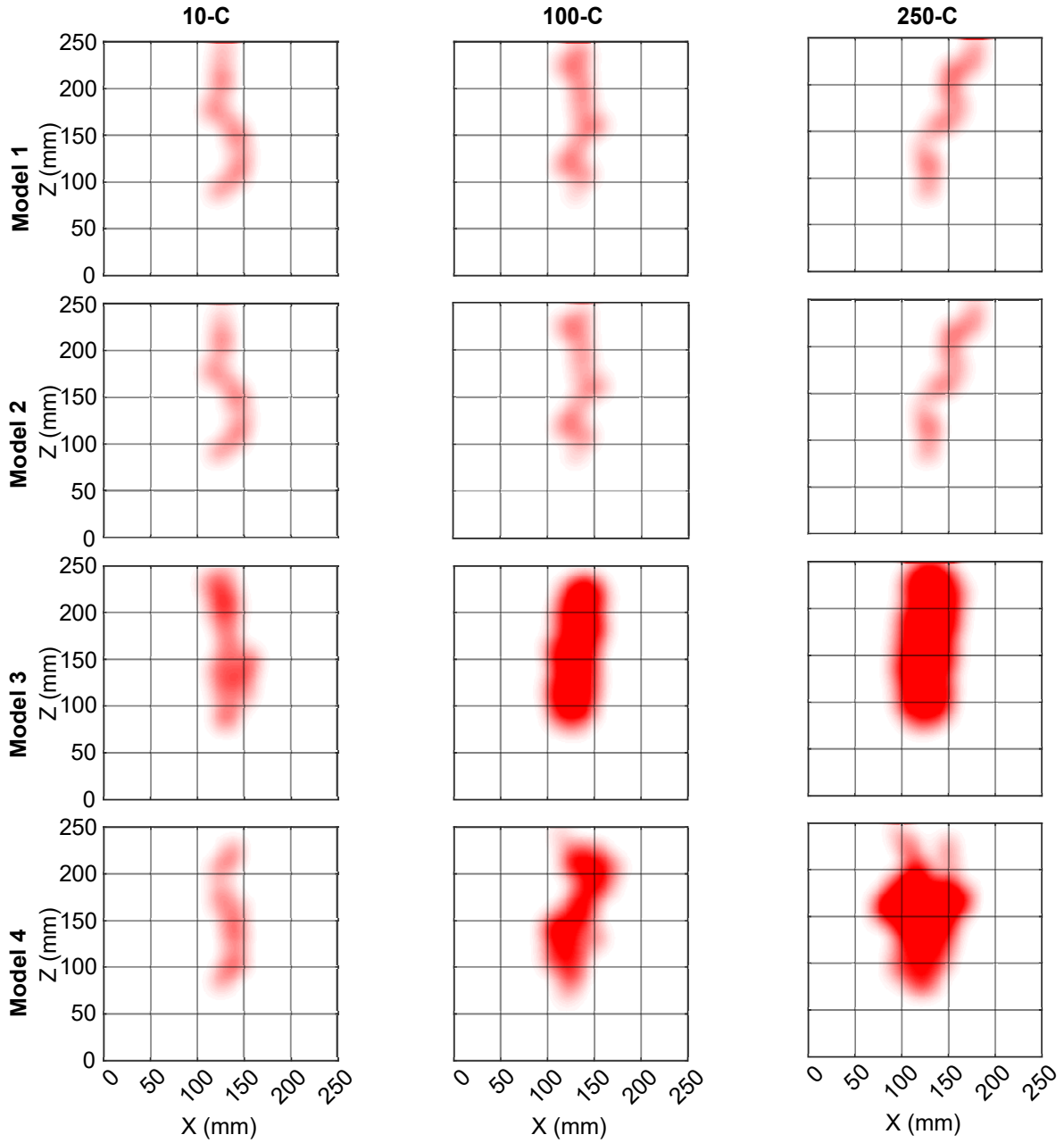
Figure B.10: Model images for the different model versions with the best fit to blurred experimental images (with highest Diffused Jaccard (med) value) from experiment no. 10-C, 100-C and 250-C. Row 1, Row 2, Row 3 and Row 4 correspond to Model 1, Model 2, Model 3 and Model 4, respectively.
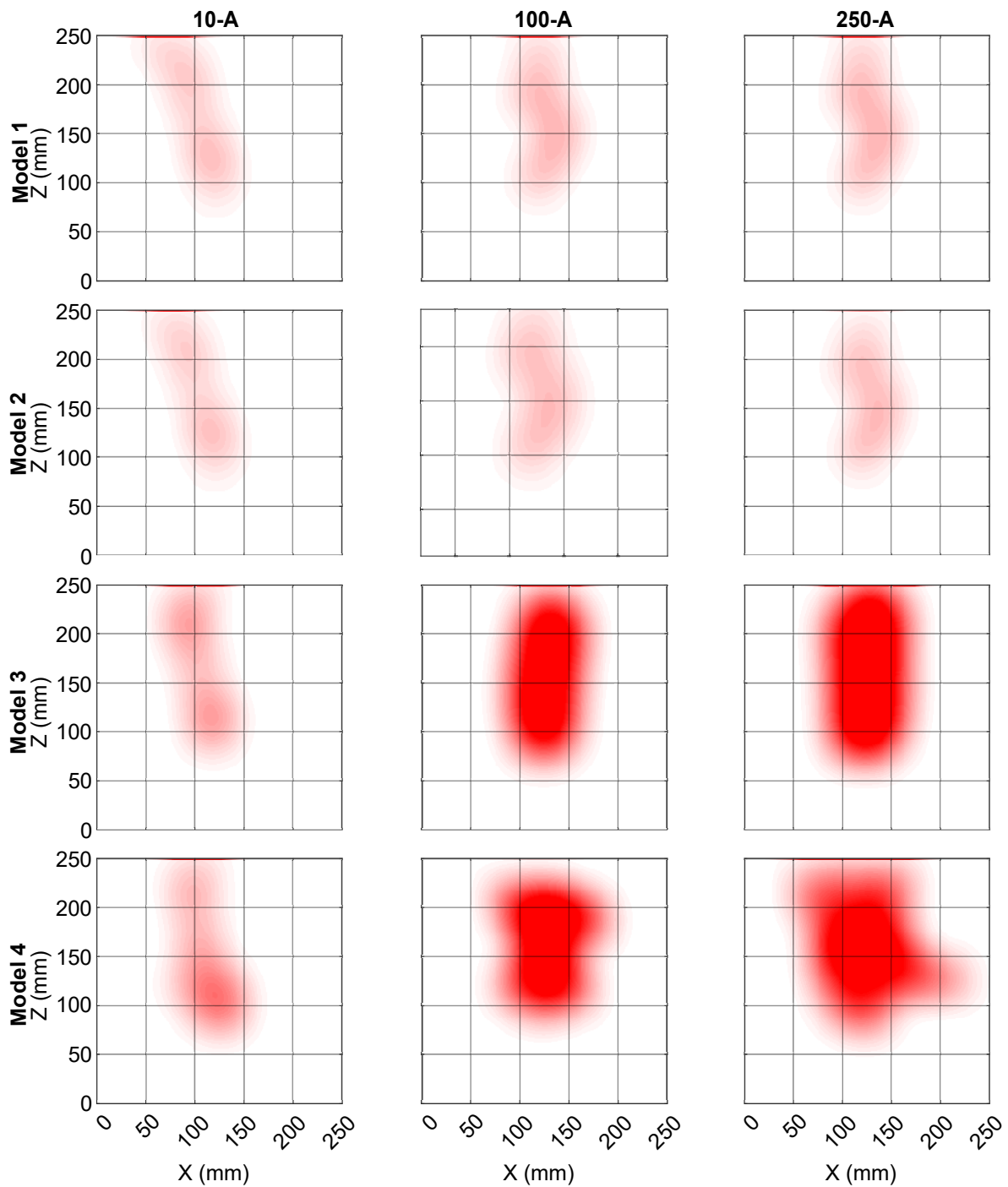
Figure B.11: Model images for the different model versions with the best fit to blurred experimental images (with highest Diffused Jaccard (high) value) from experiment no. 10-A, 100-A and 250-A. Row 1, Row 2, Row 3 and Row 4 correspond to Model 1, Model 2, Model 3 and Model 4, respectively.
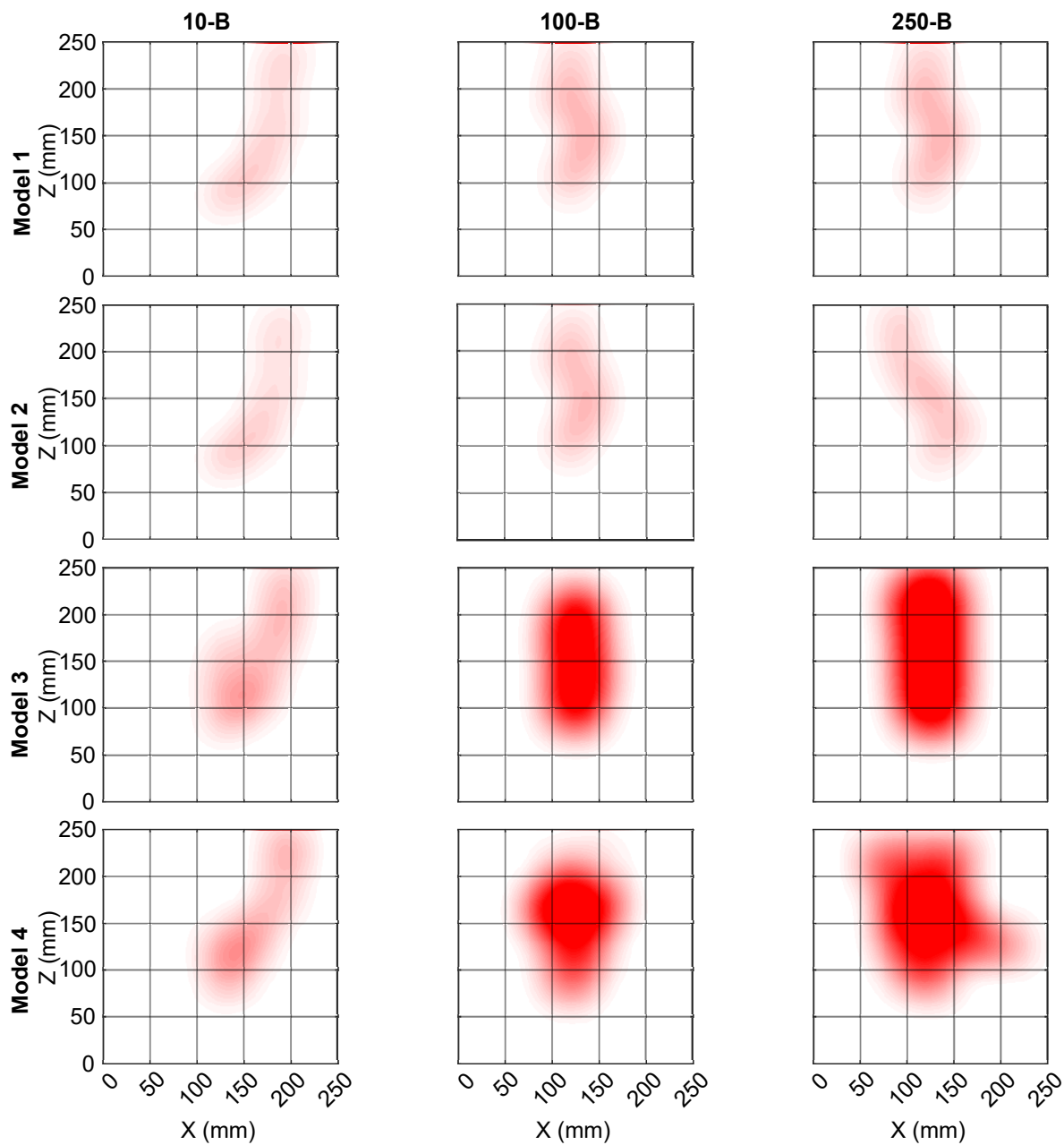
Figure B.12: Model images for the different model versions with the best fit to blurred experimental images (with highest Diffused Jaccard (high) value) from experiment no. 10-B, 100-B and 250-B. Row 1, Row 2, Row 3 and Row 4 correspond to Model 1, Model 2, Model 3 and Model 4, respectively.
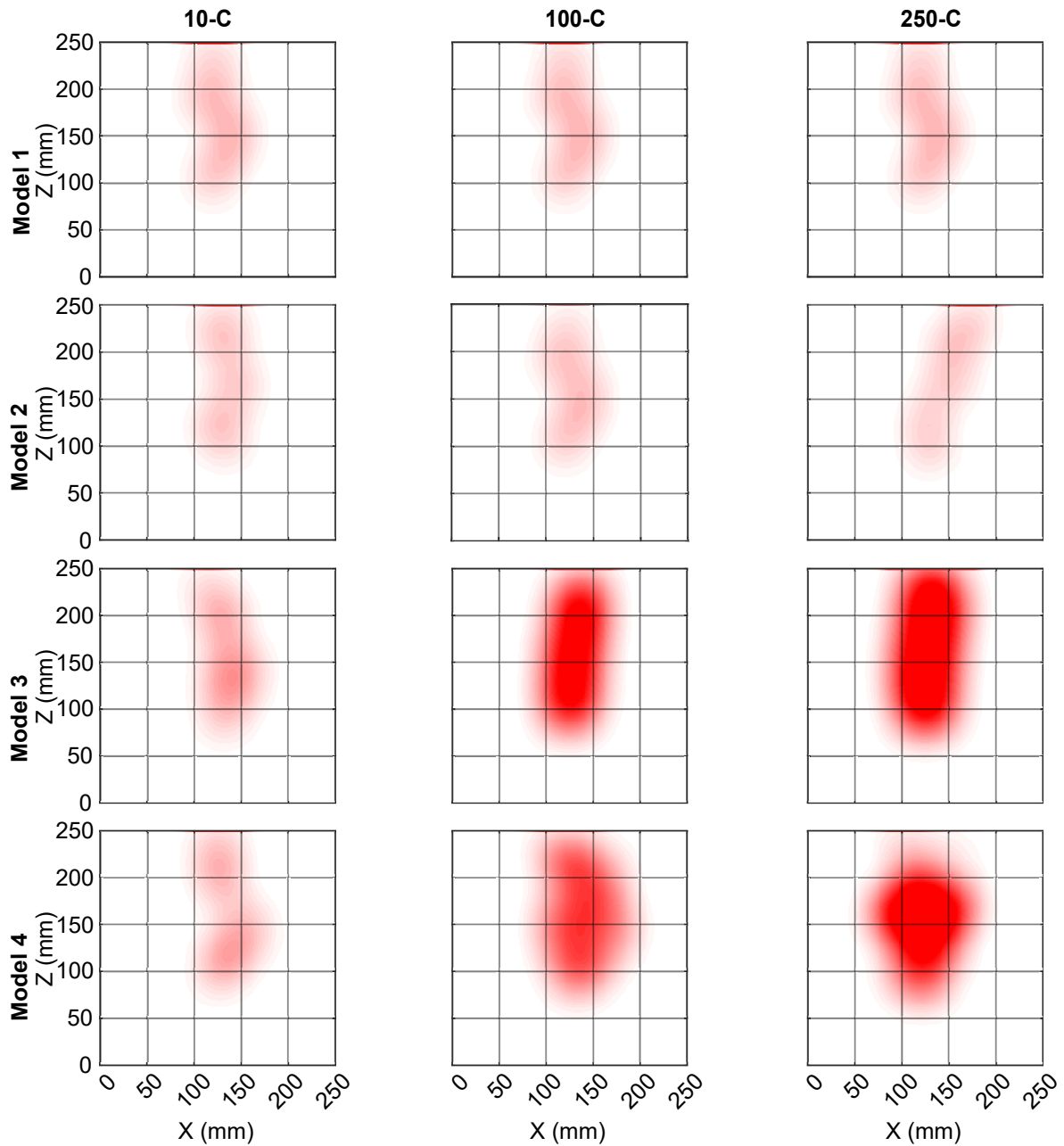
Figure B.13: Model images for the different model versions with the best fit to blurred experimental images (with highest Diffused Jaccard (high) value) from experiment no. 10-C, 100-C and 250-C. Row 1, Row 2, Row 3 and Row 4 correspond to Model 1, Model 2, Model 3 and Model 4, respectively.

C Appendix to Chapter 5*

C.1 Monte Carlo Simulations Grow Exponentially in t_{max}

Let us prove here that the required size of MC simulations grows exponentially in t_{max}. Based on the tree structure in the didactic example from Section 5.2, one can see that there are $N = 2^{t_{max}}$ equiprobable branches. Therefore, the probability of the correct branch (the one with non-zero likelihood) is exactly:

$$P_{true} = \frac{1}{N} = \frac{1}{2^{t_{max}}} = 2^{-t_{max}} = BME, \tag{C.1}$$

which apparently is the situation-specific definition of BME. When approximating BME via MC sampling with $i = 1 \ldots n$ independent random realizations, then each realization i has a constant and independent probability of finding or not finding the correct branch. This situation is described exactly by the Binomial distribution. The Binomial distribution is a discrete probability distribution of the number of success events k out of n independent trials:

$$P(X = k) = \binom{n}{k} p^k \left(1 - p\right)^{(n-k)} \tag{C.2}$$

where p is the probability of success, and $1 - p$ is the probability of not obtaining success. Here, I define n as number of MC trials, X is the (random under repetition of the entire MC simulation) number of times the MC finds the correct branch (i.e., the one with $Likelihood = 1$). For a given execution of MC with given n, one will find k times the correct branch and $n - k$ times any branch with $Likelihood = 0$.

Also, in the context of the example from Section 5.2, the probability parameter p of the Binomial distribution is equal to $BME = P_{true}$. From the MC results, one would estimate:

$$\widehat{BME}_{MC} = \frac{k}{n} = \hat{p} \approx BME$$

Just for reassurance, the asymptotic MC result for BME at $n \to \infty$ converges to the exact solution:

$$\mathrm{E}\left[\frac{X}{n}\right] = \frac{1}{n} E[X] = p = BME.$$

But can one estimate the MC error in this approximation, e.g., expressed as the coefficient of variation (CV)? For the Binomial distribution, it is known that:

$$\text{Variance of } X: \ \mathrm{Var}[X] = n \cdot p \cdot (1-p)$$
$$\text{Mean of } X: \ \mathrm{E}[X] = n \cdot p$$

As the conversion from k to the estimate of p is simply a division by n, applying the rules of linearized uncertainty quantification one sees that:

$$\text{Variance of } \frac{X}{n}: \ \mathrm{Var}\left[\frac{X}{n}\right] = \frac{p \cdot (1-p)}{n}$$
$$\text{Mean of } \frac{X}{n}: \ \mathrm{E}\left[\frac{X}{n}\right] = p$$

Using this in the definition of the coefficient of variation:

$$\text{CV of } \frac{X}{n} = CV\left[\widehat{BME}\right] = \frac{\sqrt{\mathrm{Var}\left[\frac{X}{n}\right]}}{\mathrm{E}\left[\frac{X}{n}\right]}$$
$$= \frac{\sqrt{1-p}}{\sqrt{n} \cdot \sqrt{p}}$$

For small values of p as in the given example with $p = 2^{-t_{max}}$, one can replace $1 - p \approx 1$, and hence:

$$\text{CV of } \frac{X}{n} \text{ for small } p: \; CV = \frac{1}{\sqrt{n} \cdot \sqrt{p}}$$
$$= \frac{1}{\sqrt{n} \cdot \sqrt{2^{-t_{max}}}}$$
$$= \frac{2^{\frac{t_{max}}{2}}}{\sqrt{n}}.$$

Thus, the number of MC runs required for a desired accuracy (expressed as a desired value of the CV) is:

$$n_{required} = \frac{2^{t_{max}}}{CV_{desired}^2}.$$

This shows that the number n of required MC samples increases, for a given precision requirement, exponentially in t_{max}. The base 2 of the exponent originates from the tree structure, where each node expands into two further branches. In real applications, where the evolution of the model over time has more than two possibilities, the base will simply increase, so the exponential growth will be even stronger.

C.2 Tackling Numerical Instabilities in Computation of BME

Here, I provide details on the approach of handling numerical instabilities in the BME computation when using MC integration (Eq. 2.14) for the uncertain parameters in Eq. 5.2.

To avoid very small likelihoods (BME values from the perspective of random events ω) turning into numerical zeros, I divide each sample likelihood by the maximum likelihood encountered in the whole ensemble, $\max\{p(\mathbf{y}_0 \mid \theta_k, M_k)\}$, yielding values between 0 and 1. Then, Eq. 5.2 rewrites as:

$$I_k = \max\{p(\mathbf{y}_0 \mid \theta_k, M_k)\} \int \frac{p\left(\mathbf{y_0} \mid \theta_k, M_k\right)}{\max\{p(\mathbf{y}_0 \mid \theta_k, M_k)\}}$$
$$\cdot \, p\left(\theta_k \mid M_k\right) d\theta_k.$$

Taking the logarithm and applying the MC approximation of the integral yields:

$$\ln I_k = \ln \max\{p(\mathbf{y}_0 \mid \theta_k, M_k)\} - \ln N$$
$$+ \ln \sum_{r=1}^{N} \frac{p\left(\mathbf{y_0} \mid \theta_{k,r}, M_k\right)}{\max\{p(\mathbf{y}_0 \mid \theta_k, M_k)\}}.$$

Bibliography

R. Adrian. Twenty years of particle image velocimetry. *Experiments in Fluids*, 39: 159–169, 2005. doi: 10.1007/s00348-005-0991-7.

I. Banerjee, A. Guthke, C. J. C. Van De Ven, K. G. Mumford, and W. Nowak. Comparison of four competing invasion percolation models for gas flow in porous media (*tentative title*). *manuscript to be submitted to a geoscientific journal*.

I. Banerjee, A. Guthke, C. J. C. Van De Ven, K. G. Mumford, and W. Nowak. Overcoming the model-data-fit problem in porous media: A quantitative method to compare invasion-percolation models to high-resolution data. *Water Resources Research*, 57, 2021. doi: 10.1029/2021WR029986.

I. Banerjee, P. Walter, A. Guthke, K. G. Mumford, and W. Nowak. The method of forced probabilities: a computation trick for bayesian model evidence. *Computational Geosciences*, 27:45–62, 2023. doi: 10.1007/s10596-022-10179-x.

M. A. Beaumont. Approximate bayesian computation in evolution and ecology. *Annual Review of Ecology, Evolution, and Systematics*, 41(1):379–406, 2010. doi: 10.1146/annurev-ecolsys-102209-144621.

T. Bengtsson, P. Bickel, and B. Li. Curse-of-dimensionality revisited: Collapse of the particle filter in very large scale systems. In D. Nolan and T. Speed, editors, *Probability and Statistics: Essays in Honor of David A. Freedman*, volume 2, pages 316–334, Beachwood, Ohio, USA, 2008. Institute of Mathematical Statistics.

B. Berkowitz and R. P. Ewing. Percolation theory and network modeling applications in soil physics. *Surveys in Geophysics*, 19:23–72, 1998. doi: 10.1023/A:1006590500229.

A. Birovljev, L. Furuberg, J. Feder, T. Jøssang, K. J. Mly, and A. Aharony. Gravity invasion percolation in two dimensions: Experiment and simulation. *Physical Review Letters*, 1991. ISSN 00319007. doi: 10.1103/PhysRevLett.67.584.

S. R. Broadbent and J. M. Hammersley. Percolation processes: I. crystals and mazes. *Mathematical Proceedings of the Cambridge Philosophical Society*, 53(3):629–641, 1957. doi: 10.1017/S0305004100032680.

M. C. Brooks, W. R. Wise, and M. D. Annable. Fundamental changes in in situ air sparging flow patterns. *Groundwater Monitoring & Remediation*, 19(2):105–113, 1999. doi: 10.1111/j.1745-6592.1999.tb00211.x.

R. Brooks and A. Corey. Hydraulic properties of porous media. *Hydrology Papers, Colorado State University*, page 4, 1964.

A. J. Cavanagh and R. S. Haszeldine. The sleipner storage site: Capillary flow modeling of a layered co2 plume requires fractured shale barriers within the utsira formation. *International Journal of Greenhouse Gas Control*, 21:101–112, 2014. ISSN 1750-5836. doi: 10.1016/j.ijggc.2013.11.017.

M. M. Deza and E. Deza. *Encyclopedia of Distances*. Springer-Verlag, Berlin, Heidelberg, 2016. ISBN 978-3-662-52844-0. doi: 10.1007/978-3-662-52844-0.

H. I. Essaid and K. M. Hess. Monte Carlo Simulations of Multiphase Flow Incorporating Spatial Variability of Hydraulic Properties. *Groundwater*, 1993. ISSN 17456584. doi: 10.1111/j.1745-6584.1993.tb00836.x.

R. P. Ewing and B. Berkowitz. A generalized growth model for simulating initial migration of dense non-aqueous phase liquids. *Water Resources Research*, 34:611–622, 1998. doi: 10.1029/97WR03754.

R. P. Ewing and B. Berkowitz. Stochastic pore-scale growth models of DNAPL migration in porous media. *Advances in Water Resources*, 2001. ISSN 03091708. doi: 10.1016/S0309-1708(00)00059-2.

R. P. Ewing and S. C. Gupta. Modeling percolation properties of random media using a domain network. *Water Resources Research*, 29(9):3169–3178, 1993. doi: 10.1029/93WR01496.

L. Foglia, S. W. Mehl, M. C. Hill, and P. Burlando. Evaluating model structure adequacy: The case of the maggia valley groundwater system, southern switzerland. *Water Resources Research*, 49:260–282, 2013. doi: 10.1029/2011WR011779.

V. Frette, J. Feder, T. Jøssang, and P. Meakin. Buoyancy-driven fluid migration in porous media. *Physical Review Letters*, 1992. ISSN 00319007. doi: 10.1103/PhysRevLett.68.3164.

H. Gao, A. Tatomir, N. Karadimitriou, H. Steeb, and M. Sauter. Effects of surface roughness on the kinetic interface-sensitive tracer transport during drainage processes. *Advances in Water Resources*, 157:104044, 2021. ISSN 0309-1708. doi: 10.1016/j.advwatres.2021.104044.

H. Geistlinger, G. Krauss, D. Lazik, and L. Luckner. Direct gas injection into saturated glass beads: Transition from incoherent to coherent gas flow pattern. *Water Resources Research*, 42(7):1–12, 2006. ISSN 00431397. doi: 10.1029/2005WR004451.

J. I. Gerhard and B. H. Kueper. Capillary pressure characteristics necessary for simulating DNAPL infiltration, redistribution, and immobilization in saturated porous media. *Water Resources Research*, 2003. ISSN 00431397. doi: 10.1029/2002WR001270.

S. Gideon. Estimating the dimension of a model. *The Annals of Statistics*, 6(2):461–464, 1978.

R. Glass and M. Nicholl. Physics of gravity fingering of immiscible fluids within porous media: An overview of current understanding and selected complicating factors. *Geoderma*, 70(2):133–163, 1996. ISSN 0016-7061. doi: 10.1016/0016-7061(95)00078-X.

R. J. Glass and L. Yarrington. Simulation of gravity fingering in porous media using a modified invasion percolation model. *Geoderma*, 70(2):231–252, 1996. ISSN 0016-7061. doi: 10.1016/0016-7061(95)00087-9.

R. J. Glass and L. Yarrington. Mechanistic modeling of fingering, nonmonotonicity, fragmentation, and pulsation within gravity/buoyant destabilized two-phase/unsaturated flow. *Water Resources Research*, 39(3), 2003. doi: 10.1029/2002WR001542.

R. J. Glass, S. H. Conrad, and W. Peplinski. Gravity-destabilized nonwetting phase invasion in macroheterogeneous porous media: Experimental observations of invasion

dynamics and scale analysis. *Water Resources Research*, 36(11):3121–3137, 2000. doi: 10.1029/2000WR900152.

R. J. Glass, S. H. Conrad, and L. Yarrington. Gravity-destabilized nonwetting phase invasion in macroheterogeneous porous media: Near-pore-scale macro modified invasion percolation simulation of experiments. *Water Resources Research*, 37(5):1197–1207, 2001. ISSN 00431397. doi: 10.1029/2000WR900294.

W. Gong, H. V. Gupta, D. Yang, K. Sricharan, and A. O. Hero III. Estimating epistemic and aleatory uncertainties during hydrologic modeling: An information theoretic approach. *Water Resources Research*, 49(4):2253–2273, 2013. doi: doi.org/10.1002/wrcr.20161.

A. González-Nicolás, L. Trevisan, T. H. Illangasekare, A. Cihan, and J. T. Birkholzer. Enhancing capillary trapping effectiveness through proper time scheduling of injection of supercritical CO2 in heterogeneous formations. *Greenhouse Gases: Science and Technology*, 2017. ISSN 21523878. doi: 10.1002/ghg.1646.

A. González-Nicolás, M. Schwientek, M. Sinsbeck, and W. Nowak. Characterization of export regimes in concentration–discharge plots via an advanced time-series model and event-based sampling strategies. *Water*, 13, 2021. doi: 10.3390/w13131723.

F. Gustafsson. Particle filter theory and practice with positioning applications. *IEEE Aerospace and Electronic Systems Magazine*, 25(7):53–82, 2010. doi: 10.1109/MAES.2010.5546308.

J. M. Hammersley. Monte carlo methods for solving multivariable problems. *Annals of the New York Academy of Sciences*, 86:844–874, 1960. doi: 10.1111/j.1749-6632.1960.tb42846.x.

P. R. Hegele and K. G. Mumford. Gas production and transport during bench-scale electrical resistance heating of water and trichloroethene. *Journal of Contaminant Hydrology*, 2014. ISSN 18736009. doi: 10.1016/j.jconhyd.2014.07.002.

R. J. Held and T. H. Illangasekare. Fingering of dense nonaqueous phase liquids in porous media: 2. analysis and classification. *Water Resources Research*, 31(5):1223–1231, 1995. doi: 10.1029/95WR00429.

M. Höge, T. Wöhling, and W. Nowak. A primer for model selection: The decisive role of model complexity. *Water Resources Research*, 54(3):1688–1715, 2018. doi: 10.1002/2017WR021902.

J. Holden. *Darcy's Law*, pages 63–64. John Wiley & Sons, Ltd, 2005. ISBN 9780471478447. doi: 10.1002/047147844X.gw146.

M. A. Ioannidis, I. Chatzis, and F. A. L. Dullien. Macroscopic percolation model of immiscible displacement: Effects of buoyancy and spatial structure. *Water Resources Research*, 32(11):3297–3310, 1996. doi: 10.1029/95WR02216.

J. W. Jawitz, M. D. Annable, G. G. Demmy, and P. S. Rao. Estimating nonaqueous phase liquid spatial variability using partitioning tracer higher temporal moments. *Water Resources Research*, 2003. ISSN 00431397. doi: 10.1029/2002WR001309.

H. Jeffreys. *Theory of probability*. Clarendon Press, Oxford, U.K., 3rd edition, 1961.

W. Ji, A. Dahmani, D. P. Ahlfeld, J. D. Lin, and E. Hill III. Laboratory study of air sparging: Air flow visualization. *Groundwater Monitoring & Remediation*, 13(4): 115–126, 1993. doi: 10.1111/j.1745-6592.1993.tb00455.x.

R. E. Kass and A. E. Raftery. Bayes factors. *Journal of the American Statistical Association*, 90:773–795, 1995. doi: 10.1080/01621459.1995.10476572.

C. Kechavarzi, K. Soga, and P. Wiart. Multispectral image analysis method to determine dynamic fluid saturation distribution in two-dimensional three-fluid phase flow laboratory experiments. *Journal of Contaminant Hydrology*, 2000. ISSN 01697722. doi: 10.1016/S0169-7722(00)00133-9.

T. Kloek and H. K. van Dijk. Bayesian estimates of equation system parameters: An application of integration by monte carlo. *Econometrica*, 46:1–19, 1978. doi: 10.2307/1913641.

J. Koch and W. Nowak. Predicting dnapl mass discharge and contaminated site longevity probabilities: Conceptual model and high-resolution stochastic simulation. *Water Resources Research*, 51(2):806–831, 2015. doi: 10.1002/2014WR015478.

A. Kolmogorov. *Foundations of the theory of probability*. Chelsea Publishing Company, New York, 1950.

B. H. Kueper and J. I. Gerhard. Variability of point source infiltration rates for two-phase flow in heterogeneous porous media. *Water Resources Research*, 1995. ISSN 19447973. doi: 10.1029/95WR02329.

B. H. Kueper and D. B. McWhorter. The use of macroscopic percolation theory to construct large-scale capillary pressure curves. *Water Resources Research*, 1992. ISSN 19447973. doi: 10.1029/92WR01176.

R. Lenormand, E. Touboul, and C. Zarcone. Numerical models and experiments on immiscible displacements in porous media. *Journal of Fluid Mechanics*, 189(November): 165–187, 1988. ISSN 14697645. doi: 10.1017/S0022112088000953.

G. Løvoll, Y. Méheust, K. J. Måløy, E. Aker, and J. Schmittbuhl. Competition of gravity, capillary and viscous forces during drainage in a two-dimensional porous medium, a pore scale study. *Energy*, 30(6):861–872, 2005. ISSN 0360-5442. doi: 10.1016/j.energy.2004.03.100. Second International Onsager Conference.

P. Meakin and J. M. Deutch. The formation of surfaces by diffusion limited annihilation. *The Journal of Chemical Physics*, 85(4):2320–2325, 1986. doi: 10.1063/1.451129.

P. Meakin, J. Feder, V. Frette, and T. Jøssang. Invasion percolation in a destabilizing gradient. *Phys. Rev. A*, 46:3357–3368, Sep 1992. doi: 10.1103/PhysRevA.46.3357.

I. L. Molnar, K. G. Mumford, and M. M. Krol. Electro-Thermal Subsurface Gas Generation and Transport: Model Validation and Implications. *Water Resources Research*, 2019. ISSN 19447973. doi: 10.1029/2018WR024095.

E. Morales-Casique, S. P. Neuman, and V. V. Vesselinov. Maximum likelihood bayesian averaging of airflow models in unsaturated fractured tuff using occam and variance windows. *Stochastic Environmental Research and Risk Assessment*, 24:863–880, 2010. doi: 10.1007/s00477-010-0383-2.

N. R. Morrow. Interplay of Capillary, Viscous And Buoyancy Forces In the Mobilization of Residual Oil. *Journal of Canadian Petroleum Technology*, 18(03), 07 1979. ISSN 0021-9487. doi: 10.2118/79-03-03.

K. G. Mumford, S. E. Dickson, and J. E. Smith. Slow gas expansion in saturated natural porous media by gas injection and partitioning with non-aqueous phase

liquids. *Advances in Water Resources*, 32(1):29–40, 2009. ISSN 03091708. doi: 10.1016/j.advwatres.2008.09.006.

K. G. Mumford, J. E. Smith, and S. E. Dickson. The effect of spontaneous gas expansion and mobilization on the aqueous-phase concentrations above a dense nonaqueous phase liquid pool. *Advances in Water Resources*, 33(4):504–513, 2010. ISSN 03091708. doi: 10.1016/j.advwatres.2010.02.002.

K. G. Mumford, P. R. Hegele, and G. P. Vandenberg. Comparison of Two-Dimensional and Three-Dimensional Macroscopic Invasion Percolation Simulations with Laboratory Experiments of Gas Bubble Flow in Homogeneous Sands. *Vadose Zone Journal*, 14(11):0, 2015. doi: 10.2136/vzj2015.02.0028.

M. R. Niemet and J. S. Selker. A new method for quantification of liquid saturation in 2D translucent porous media systems using light transmission. *Advances in Water Resources*, 24(6):651–666, 2001. ISSN 03091708. doi: 10.1016/S0309-1708(00) 00045-2.

E. G. Nisbet, E. J. Dlugokencky, M. R. Manning, D. Lowry, R. E. Fisher, J. L. France, S. E. Michel, J. B. Miller, J. W. C. White, B. Vaughn, P. Bousquet, J. A. Pyle, N. J. Warwick, M. Cain, R. Brownlow, G. Zazzeri, M. Lanoisellé, A. C. Manning, E. Gloor, D. E. J. Worthy, E.-G. Brunke, C. Labuschagne, E. W. Wolff, and A. L. Ganesan. Rising atmospheric methane: 2007–2014 growth and isotopic shift. *Global Biogeochemical Cycles*, 30(9):1356–1370, 2016. doi: 10.1002/2016GB005406.

W. Nowak. Best unbiased ensemble linearization and the quasi-linear kalman ensemble generator. *Water Resources Research*, 45(4), 2009. doi: 10.1029/2008WR007328.

C. M. Oldenburg, S. Mukhopadhyay, and A. Cihan. On the use of darcy's law and invasion-percolation approaches for modeling large-scale geologic carbon sequestration. *Greenhouse Gases: Science and Technology*, 6(1):19–33, 2016. doi: 10.1002/ghg.1564.

M. Oostrom, J. H. Dane, and T. W. Wietsma. A Review of Multidimensional, Multifluid, Intermediate-Scale Experiments: Flow Behavior, Saturation Imaging, and Tracer Detection and Quantification. *Vadose Zone Journal*, 2007. ISSN 1539-1663. doi: 10.2136/vzj2006.0178.

M. Pantazidou and K. Liu. DNAPL distribution in the source zone: Effect of soil structure and uncertainty reduction with increased sampling density. *Journal of Contaminant Hydrology*, 2008. ISSN 01697722. doi: 10.1016/j.jconhyd.2007.11.002.

L. Paterson. Diffusion-limited aggregation and two-fluid displacements in porous media. *Phys. Rev. Lett.*, 52:1621–1624, Apr 1984. doi: 10.1103/PhysRevLett.52.1621.

E. Petermann and P. Bossew. Mapping indoor radon hazard in germany: The geogenic component. *Science of The Total Environment*, 780:146601, 2021. ISSN 0048-9697. doi: 10.1016/j.scitotenv.2021.146601.

E. Petermann, H. Meyer, M. Nussbaum, and P. Bossew. Mapping the geogenic radon potential for germany by machine learning. *Science of The Total Environment*, 754: 142291, 2021. ISSN 0048-9697. doi: 10.1016/j.scitotenv.2020.142291.

E. Poeter and D. Anderson. Multimodel ranking and inference in ground water modeling. *Ground Water*, 43:597–605, 2005. doi: 10.1111/j.1745-6584.2005.0061.x.

M. Ramgraber, C. Albert, and M. Schirmer. Data assimilation and online parameter optimization in groundwater modeling using nested particle filters. *Water Resources Research*, 55(11):9724–9747, 2019. doi: 10.1029/2018WR024408.

S. Razavi, B. A. Tolson, and D. H. Burn. Review of surrogate modeling in water resources. *Water Resources Research*, 48(7), 2012. doi: 10.1029/2011WR011527.

V. Reitenbach, L. Ganzer, D. Albrecht, and B. Hagemann. Influence of added hydrogen on underground gas storage: a review of key issues. *Environmental Earth Sciences*, 73(11):6927–6937, 2015. doi: 10.1007/s12665-015-4176-2.

T. Sakaki, M. R. Plampin, R. Pawar, M. Komatsu, and T. H. Illangasekare. What controls carbon dioxide gas phase evolution in the subsurface? Experimental observations in a 4.5m-long column under different heterogeneity conditions. *International Journal of Greenhouse Gas Control*, 2013. ISSN 17505836. doi: 10.1016/j.ijggc.2013.03.025.

A. Schöniger, W. Nowak, and H.-J. Hendricks Franssen. Parameter estimation by ensemble kalman filters with transformed data: Approach and application to hydraulic tomography. *Water Resources Research*, 48(4), 2012a. doi: 10.1029/2011WR010462.

A. Schöniger, W. Nowak, and H.-J. Hendricks Franssen. Parameter estimation by ensemble kalman filters with transformed data: Approach and application to hydraulic tomography. *Water Resources Research*, 48(4), 2012b. doi: 10.1029/2011WR010462.

M. H. Schroth, J. D. Istok, S. J. Ahearn, and J. S. Selker. Characterization of miller-similar silica sands for laboratory hydrologic studies. *Soil Science Society of America Journal*, 60:1331–1339, 1996. doi: 10.2136/sssaj1996.03615995006000050007x.

A. Schöniger, T. Wöhling, L. Samaniego, and W. Nowak. Model selection on solid ground: Rigorous comparison of nine ways to evaluate bayesian model evidence. *Water Resources Research*, 50:9484–9513, 2014. doi: 10.1002/2014WR016062.

J. S. Selker, M. Niemet, S. M. Mcduffie, Norton G.and Gorelick, and J.-Y. Parlange. The local geometry of gas injection into saturated homogeneous porous media. *Transp Porous Med*, 68:107–127, 2006. doi: 10.1007/s11242-006-0005-0.

S. A. Shapiro. *Microseismicity - a tool for reservoir characterization*. EAGE Publications bv, Amsterdam, 2008.

A. Singh, S. Mishra, and G. Ruskauff. Model averaging techniques for quantifying conceptual model uncertainty. *Ground Water*, 48:701–715, 2010. doi: 10.1111/j.1745-6584.2009.00642.x.

C. Snyder, T. Bengtsson, P. Bickel, and J. Anderson. Obstacles to high-dimensional particle filtering. *Monthly Weather Review*, 136:4629–4640, 2008. doi: 10.1175/2008MWR2529.1.

M. Stöhr and A. Khalili. Dynamic regimes of buoyancy-affected two-phase flow in unconsolidated porous media. *Phys. Rev. E*, 73:036301, Mar 2006. doi: https://10.1103/PhysRevE.73.036301.

P.-N. Tan, M. Steinbach, and V. Kumar. Association Analysis: Basic Concepts and Algorithms. *Introduction to Data mining*, 2005. ISSN 1600-0765. doi: 10.1111/j.1600-0765.2011.01426.x.

V. C. Tidwell and R. J. Glass. X ray and visible light transmission for laboratory measurement of two-dimensional saturation fields in thin-slab systems. *Water Resources Research*, 30(11):2873–2882, 1994. ISSN 19447973. doi: 10.1029/94WR00953.

L. Trevisan, R. Pini, A. Cihan, J. T. Birkholzer, Q. Zhou, and T. H. Illangasekare. Experimental analysis of spatial correlation effects on capillary trapping of supercritical CO2 at the intermediate laboratory scale in heterogeneous porous media. *Water Resources Research*, 2015. ISSN 19447973. doi: 10.1002/2015WR017440.

L. Trevisan, T. H. Illangasekare, and T. A. Meckel. Modelling plume behavior through a heterogeneous sand pack using a commercial invasion percolation model. *Geomechanics and Geophysics for Geo-Energy and Geo-Resources*, 3(3):327–337, 2017. ISSN 23638427. doi: 10.1007/s40948-017-0055-5.

F. T.-C. Tsai and X. Li. Inverse groundwater modeling for hydraulic conductivity estimation using bayesian model averaging and variance window. *Water Resources Research*, 44, 2008. doi: 10.1029/2007WR006576.

F. T.-C. Tsai and X. Li. Reply to comment by ming ye et al. on "inverse groundwater modeling for hydraulic conductivity estimation using bayesian model averaging and variance window". *Water Resources Research*, 46, 2010. doi: 10.1029/2009WR008591.

I. N. Tsimpanogiannis and Y. C. Yortsos. The critical gas saturation in a porous medium in the presence of gravity. *Journal of Colloid and Interface Science*, 2004. ISSN 00219797. doi: 10.1016/j.jcis.2003.09.036.

C. Van De Ven and K. G. Mumford. Visualization of gas dissolution following upward gas migration in porous media: Technique and implications for stray gas. *Advances in Water Resources*, 115:33–43, 2018. ISSN 0309-1708. doi: 10.1016/j.advwatres.2018.02.015.

C. J. Van De Ven and K. G. Mumford. Characterization of gas injection flow patterns subject to gravity and viscous forces. *Vadose Zone Journal*, 18(1):1–11, 2019. ISSN 1539-1663. doi: 10.2136/vzj2019.02.0014.

C. J. Van De Ven, J. E. Abraham, and K. G. Mumford. Laboratory investigation of free-phase stray gas migration in shallow aquifers using modified light transmission. *Advances in Water Resources*, 2020. ISSN 03091708. doi: 10.1016/j.advwatres.2020.103543.

A. Vengosh, N. Warner, R. Jackson, and T. Darrah. The Effects of Shale Gas Exploration and Hydraulic Fracturing on the Quality of Water Resources in the

United States. *Procedia Earth and Planetary Science*, 2013. ISSN 18785220. doi: 10.1016/j.proeps.2013.03.213.

A. Vengosh, R. Jackson, N. Warner, T. Darrah, and A. Kondash. A critical review of the risks to water resources from unconventional shale gas development and hydraulic fracturing in the united states. *Environmental science & technology*, 48, 03 2014. doi: 10.1021/es405118y.

G. Wagner, P. Meakin, J. Feder, and T. Jøssang. Buoyancy-driven invasion percolation with migration and fragmentation. *Physica A: Statistical Mechanics and its Applications*, 245(3-4):217–230, 1997. ISSN 03784371. doi: 10.1016/S0378-4371(97)00324-5.

C. J. Werth, C. Zhang, M. L. Brusseau, M. Oostrom, and T. Baumann. A review of non-invasive imaging methods and applications in contaminant hydrogeology research. *Journal of Contaminant Hydrology*, 2010. ISSN 01697722. doi: 10.1016/j.jconhyd. 2010.01.001.

D. Wilkinson. Percolation model of immiscible displacement in the presence of buoyancy forces. *Physical Review A*, 1984. ISSN 10502947. doi: 10.1103/PhysRevA.30.520.

D. Wilkinson and J. F. Willemsen. Invasion percolation: A new form of percolation theory. *Journal of Physics A: Mathematical and General*, 1983. ISSN 13616447. doi: 10.1088/0305-4470/16/14/028.

K. Willcox and J. Peraire. Balanced model reduction via the proper orthogonal decomposition. *AIAA Journal*, 40(11):2323–2330, 2002. doi: 10.2514/2.1570.

T. A. Witten and L. M. Sander. Diffusion-limited aggregation. *Phys. Rev. B*, 27: 5686–5697, May 1983. doi: 10.1103/PhysRevB.27.5686.

A. W. Woods and S. Norris. Dispersion and dissolution of a buoyancy driven gas plume in a layered permeable rock. *Water Resources Research*, 52(4):2682–2697, 2016. doi: 10.1002/2015WR018159.

D. Xiu and G. E. Karniadakis. The wiener–askey polynomial chaos for stochastic differential equations. *SIAM Journal on Scientific Computing*, 24(2):619–644, 2002. doi: 10.1137/S1064827501387826.

T. Xu, S. Reuschen, W. Nowak, and H.-J. Hendricks Franssen. Preconditioned crank-nicolson markov chain monte carlo coupled with parallel tempering: An efficient method for bayesian inversion of multi-gaussian log-hydraulic conductivity fields. *Water Resources Research*, 56(8):e2020WR027110, 2020. doi: 10.1029/2020WR027110.

M. Ye, P. D. Meyer, and S. P. Neuman. On model selection criteria in multimodel analysis. *Water Resources Research*, 44, 2008. doi: 10.1029/2008WR006803.

M. Ye, D. Lu, S. P. Neuman, and P. D. Meyer. Comment on "inverse groundwater modeling for hydraulic conductivity estimation using bayesian model averaging and variance window" by frank t.-c. tsai and xiaobao li. *Water Resources Research*, 46, 2010a. doi: 10.1029/2009WR008501.

M. Ye, K. F. Pohlmann, J. B. Chapman, G. M. Pohll, and D. M. Reeves. A model-averaging method for assessing groundwater conceptual model uncertainty. *Ground Water*, 48:716–728, 2010b. doi: 10.1111/j.1745-6584.2009.00633.x.

A. Zellner and P. E. Rossi. Bayesian analysis of dichotomous quantal response models. *Journal of Econometrics*, 25:365–393, 1984. doi: 10.1016/0304-4076(84)90007-1.

Y. Zhang, Y. Liu, G. Pau, S. Oladyshkin, and S. Finsterle. Evaluation of multiple reduced-order models to enhance confidence in global sensitivity analyses. *International Journal of Greenhouse Gas Control*, 49:217–226, 2016. ISSN 1750-5836. doi: 10.1016/j.ijggc.2016.03.003.
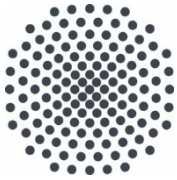
Institut für Wasser- und Umweltsystemmodellierung
Universität Stuttgart

Pfaffenwaldring 61
70569 Stuttgart (Vaihingen)
Telefon (0711) 685 - 60156
Telefax (0711) 685 - 51073
E-Mail: iws@iws.uni-stuttgart.de
http://www.iws.uni-stuttgart.de

Direktoren
Prof. Dr.-Ing. Rainer Helmig
Prof. Dr.-Ing. Wolfgang Nowak
Prof. Dr.-Ing. Silke Wieprecht

Emeriti
Prof. Dr.-Ing. habil. Dr.-Ing. E.h. Jürgen Giesecke
Prof. Dr.h.c. Dr.-Ing. E.h. Helmut Kobus, PhD

Lehrstuhl für Wasserbau und
Wassermengenwirtschaft
Leiterin: Prof. Dr.-Ing. Silke Wieprecht
Stellv.: Dr.-Ing. Kristina Terheiden
Versuchsanstalt für Wasserbau
Leiter: Stefan Haun, PhD

Lehrstuhl für Hydromechanik
und Hydrosystemmodellierung
Leiter: Prof. Dr.-Ing. Rainer Helmig
Stellv.: apl. Prof. Dr.-Ing. Holger Class

Lehrstuhl für Stochastische Simulation und
Sicherheitsforschung für Hydrosysteme
Leiter: Prof. Dr.-Ing. Wolfgang Nowak
Stellv.: apl. Prof. Dr.-Ing. Sergey Oladyshkin
Hydrogeophysik der Vadosen Zone
(mit Forschungszentrum Jülich)
Leiter: Prof. Dr. J.A. Sander Huisman

VEGAS, Versuchseinrichtung zur
Grundwasser- und Altlastensanierung
Leiter: Dr.-Ing. Simon Kleinknecht
PD Dr.-Ing. Claus Haslauer

Verzeichnis der Mitteilungshefte

7   *Sonderheft anläßlich des 65. Geburtstages von Prof. Arthur Röhnisch mit Beiträgen von* Benk, Dieter; Breitling, J.; Gurr, Siegfried; Haberhauer, Robert; Honekamp, Hermann; Kuz, Klaus Dieter; Marotz, Günter; Mayer-Vorfelder, Hans-Jörg; Miller, Rudolf; Plate, Erich J.; Radomski, Helge; Schwarz, Helmut; Vollmer, Ernst; Wildenhahn, Eberhard; 1967

8   Jumikis, Alfred: *Beitrag zur experimentellen Untersuchung des Wassernachschubs in einem gefrierenden Boden und die Beurteilung der Ergebnisse*, 1968

9   Marotz, Günter: *Technische Grundlagen einer Wasserspeicherung im natürlichen Untergrund*, 1968

10 Radomski, Helge: *Untersuchungen über den Einfluß der Querschnittsform wellenförmiger Spundwände auf die statischen und rammtechnischen Eigenschaften*, 1968

11 Schwarz, Helmut: *Die Grenztragfähigkeit des Baugrundes bei Einwirkung vertikal gezogener Ankerplatten als zweidimensionales Bruchproblem*, 1969

12 Erbel, Klaus: *Ein Beitrag zur Untersuchung der Metamorphose von Mittelgebirgsschneedecken unter besonderer Berücksichtigung eines Verfahrens zur Bestimmung der thermischen Schneequalität*, 1969

13 Westhaus, Karl-Heinz: *Der Strukturwandel in der Binnenschiffahrt und sein Einfluß auf den Ausbau der Binnenschiffskanäle*, 1969

14 Mayer-Vorfelder, Hans-Jörg: *Ein Beitrag zur Berechnung des Erdwiderstandes unter Ansatz der logarithmischen Spirale als Gleitflächenfunktion*, 1970

15 Schulz, Manfred: *Berechnung des räumlichen Erddruckes auf die Wandung kreiszylindrischer Körper*, 1970

16 Mobasseri, Manoutschehr: *Die Rippenstützmauer. Konstruktion und Grenzen ihrer Standsicherheit*, 1970

17 Benk, Dieter: *Ein Beitrag zum Betrieb und zur Bemessung von Hochwasserrückhaltebecken*, 1970

18 Gàl, Attila: *Bestimmung der mitschwingenden Wassermasse bei überströmten Fischbauchklappen mit kreiszylindrischem Staublech*, 1971, *vergriffen*

19 Kuz, Klaus Dieter: *Ein Beitrag zur Frage des Einsetzens von Kavitationserscheinungen in einer Düsenströmung bei Berücksichtigung der im Wasser gelösten Gase*, 1971, *vergriffen*

20 Schaak, Hartmut: *Verteilleitungen von Wasserkraftanlagen*, 1971

21 *Sonderheft zur Eröffnung der neuen Versuchsanstalt des Instituts für Wasserbau der Universität Stuttgart mit Beiträgen von* Brombach, Hansjörg; Dirksen, Wolfram; Gàl, Attila; Gerlach, Reinhard; Giesecke, Jürgen; Holthoff, Franz-Josef; Kuz, Klaus Dieter; Marotz, Günter; Minor, Hans-Erwin; Petrikat, Kurt; Röhnisch, Arthur; Rueff, Helge; Schwarz, Helmut; Vollmer, Ernst; Wildenhahn, Eberhard; 1972

22 Wang, Chung-su: *Ein Beitrag zur Berechnung der Schwingungen an Kegelstrahlschiebern*, 1972

23 Mayer-Vorfelder, Hans-Jörg: *Erdwiderstandsbeiwerte nach dem Ohde-Variationsverfahren*, 1972

24 Minor, Hans-Erwin: *Beitrag zur Bestimmung der Schwingungsanfachungsfunktionen überströmter Stauklappen*, 1972, *vergriffen*

25 Brombach, Hansjörg: *Untersuchung strömungsmechanischer Elemente (Fluidik) und die Möglichkeit der Anwendung von Wirbelkammerelementen im Wasserbau*, 1972, *vergriffen*

26 Wildenhahn, Eberhard: *Beitrag zur Berechnung von Horizontalfilterbrunnen*, 1972

27 Steinlein, Helmut: *Die Eliminierung der Schwebstoffe aus Flußwasser zum Zweck der unterirdischen Wasserspeicherung, gezeigt am Beispiel der Iller*, 1972

28 Holthoff, Franz Josef: *Die Überwindung großer Hubhöhen in der Binnenschiffahrt durch Schwimmerhebewerke*, 1973

50   Mehlhorn, Hans: *Temperaturveränderungen im Grundwasser durch Brauchwassereinleitungen*, 1982, ISBN 3-921694-50-7, *vergriffen*

51   Hafner, Edzard: *Rohrleitungen und Behälter im Meer*, 1983, ISBN 3-921694-51-5

52   Rinnert, Bernd: *Hydrodynamische Dispersion in porösen Medien: Einfluß von Dichteunterschieden auf die Vertikalvermischung in horizontaler Strömung*, 1983, ISBN 3-921694-52-3, *vergriffen*

53   Lindner, Wulf: *Steuerung von Grundwasserentnahmen unter Einhaltung ökologischer Kriterien*, 1983, ISBN 3-921694-53-1, *vergriffen*

54   Herr, Michael; Herzer, Jörg; Kinzelbach, Wolfgang; Kobus, Helmut; Rinnert, Bernd: *Methoden zur rechnerischen Erfassung und hydraulischen Sanierung von Grundwasserkontaminationen*, 1983, ISBN 3-921694-54-X

55   Schmitt, Paul: *Wege zur Automatisierung der Niederschlagsermittlung*, 1984, ISBN 3-921694-55-8, *vergriffen*

56   Müller, Peter: *Transport und selektive Sedimentation von Schwebstoffen bei gestautem Abfluß*, 1985, ISBN 3-921694-56-6

57   El-Qawasmeh, Fuad: *Möglichkeiten und Grenzen der Tropfbewässerung unter besonderer Berücksichtigung der Verstopfungsanfälligkeit der Tropfelemente*, 1985, ISBN 3-921694-57-4, *vergriffen*

58   Kirchenbaur, Klaus: *Mikroprozessorgesteuerte Erfassung instationärer Druckfelder am Beispiel seegangsbelasteter Baukörper*, 1985, ISBN 3-921694-58-2

59   Kobus, Helmut (Hrsg.): *Modellierung des großräumigen Wärme- und Schadstofftransports im Grundwasser*, Tätigkeitsbericht 1984/85 (DFG-Forschergruppe an den Universitäten Hohenheim, Karlsruhe und Stuttgart), 1985, ISBN 3-921694-59-0, *vergriffen*

60   Spitz, Karlheinz: *Dispersion in porösen Medien: Einfluß von Inhomogenitäten und Dichteunterschieden*, 1985, ISBN 3-921694-60-4, *vergriffen*

61   Kobus, Helmut: *An Introduction to Air-Water Flows in Hydraulics*, 1985, ISBN 3-921694-61-2

62   Kaleris, Vassilios: *Erfassung des Austausches von Oberflächen- und Grundwasser in horizontalebenen Grundwassermodellen*, 1986, ISBN 3-921694-62-0

63   Herr, Michael: *Grundlagen der hydraulischen Sanierung verunreinigter Porengrundwasserleiter*, 1987, ISBN 3-921694-63-9

64   Marx, Walter: *Berechnung von Temperatur und Spannung in Massenbeton infolge Hydratation*, 1987, ISBN 3-921694-64-7

65   Koschitzky, Hans-Peter: *Dimensionierungskonzept für Sohlbelüfter in Schußrinnen zur Vermeidung von Kavitationsschäden*, 1987, ISBN 3-921694-65-5

66   Kobus, Helmut (Hrsg.): *Modellierung des großräumigen Wärme- und Schadstofftransports im Grundwasser*, Tätigkeitsbericht 1986/87 (DFG-Forschergruppe an den Universitäten Hohenheim, Karlsruhe und Stuttgart) 1987, ISBN 3-921694-66-3

67   Söll, Thomas: *Berechnungsverfahren zur Abschätzung anthropogener Temperaturanomalien im Grundwasser*, 1988, ISBN 3-921694-67-1

68   Dittrich, Andreas; Westrich, Bernd: *Bodenseeufererosion, Bestandsaufnahme und Bewertung*, 1988, ISBN 3-921694-68-X, *vergriffen*

69   Huwe, Bernd; van der Ploeg, Rienk R.: *Modelle zur Simulation des Stickstoffhaushaltes von Standorten mit unterschiedlicher landwirtschaftlicher Nutzung*, 1988, ISBN 3-921694-69-8, *vergriffen*

70   Stephan, Karl: *Integration elliptischer Funktionen*, 1988, ISBN 3-921694-70-1

71   Kobus, Helmut; Zilliox, Lothaire (Hrsg.): *Nitratbelastung des Grundwassers, Auswirkungen der Landwirtschaft auf die Grundwasser- und Rohwasserbeschaffenheit und Maßnahmen zum Schutz des Grundwassers*. Vorträge des deutsch-französischen Kolloquiums am 6. Oktober 1988, Universitäten Stuttgart und Louis Pasteur Strasbourg (Vorträge in deutsch oder französisch, Kurzfassungen zweisprachig), 1988, ISBN 3-921694-71-X

95   Cirpka, Olaf: *Numerische Methoden zur Simulation des reaktiven Mehrkomponenten-transports im Grundwasser*, 1997, ISBN 3-921694-95-7, *vergriffen*

96   Färber, Arne: *Wärmetransport in der ungesättigten Bodenzone: Entwicklung einer thermischen In-situ-Sanierungstechnologie*, 1997, ISBN 3-921694-96-5

97   Betz, Christoph: *Wasserdampfdestillation von Schadstoffen im porösen Medium: Entwicklung einer thermischen In-situ-Sanierungstechnologie*, 1998, SBN 3-921694-97-3

98   Xu, Yichun: *Numerical Modeling of Suspended Sediment Transport in Rivers*, 1998, ISBN 3-921694-98-1, *vergriffen*

99   Wüst, Wolfgang: *Geochemische Untersuchungen zur Sanierung CKW-kontaminierter Aquifere mit Fe(0)-Reaktionswänden,* 2000, ISBN 3-933761-02-2

100 Sheta, Hussam: *Simulation von Mehrphasenvorgängen in porösen Medien unter Einbeziehung von Hysterese-Effekten*, 2000, ISBN 3-933761-03-4

101 Ayros, Edwin: *Regionalisierung extremer Abflüsse auf der Grundlage statistischer Verfahren*, 2000, ISBN 3-933761-04-2, *vergriffen*

102 Huber, Ralf: *Compositional Multiphase Flow and Transport in Heterogeneous Porous Media*, 2000, ISBN 3-933761-05-0

103 Braun, Christopherus: *Ein Upscaling-Verfahren für Mehrphasenströmungen in porösen Medien*, 2000, ISBN 3-933761-06-9

104 Hofmann, Bernd: *Entwicklung eines rechnergestützten Managementsystems zur Beurteilung von Grundwasserschadensfällen*, 2000, ISBN 3-933761-07-7

105 Class, Holger: *Theorie und numerische Modellierung nichtisothermer Mehrphasenprozesse in NAPL-kontaminierten porösen Medien,* 2001, ISBN 3-933761-08-5

106 Schmidt, Reinhard: *Wasserdampf- und Heißluftinjektion zur thermischen Sanierung kontaminierter Standorte*, 2001, ISBN 3-933761-09-3

107 Josef, Reinhold: *Schadstoffextraktion mit hydraulischen Sanierungsverfahren unter Anwendung von grenzflächenaktiven Stoffen*, 2001, ISBN 3-933761-10-7

108 Schneider, Matthias: *Habitat- und Abflussmodellierung für Fließgewässer mit unscharfen Berechnungsansätzen*, 2001, ISBN 3-933761-11-5

109 Rathgeb, Andreas: *Hydrodynamische Bemessungsgrundlagen für Lockerdeckwerke an überströmbaren Erddämmen*, 2001, ISBN 3-933761-12-3

110 Lang, Stefan: *Parallele numerische Simulation instätionärer Probleme mit adaptiven Methoden auf unstrukturierten Gittern*, 2001, ISBN 3-933761-13-1

111 Appt, Jochen; Stumpp Simone: *Die Bodensee-Messkampagne 2001, IWS/CWR Lake Constance Measurement Program 2001*, 2002, ISBN 3-933761-14-X

112 Heimerl, Stephan: *Systematische Beurteilung von Wasserkraftprojekten,* 2002, ISBN 3-933761-15-8, *vergriffen*

113 Iqbal, Amin: *On the Management and Salinity Control of Drip Irrigation,* 2002, ISBN 3-933761-16-6

114 Silberhorn-Hemminger, Annette: *Modellierung von Kluftaquifersystemen: Geostatistische Analyse und deterministisch-stochastische Kluftgenerierung,* 2002, ISBN 3-933761-17-4

115 Winkler, Angela: *Prozesse des Wärme- und Stofftransports bei der In-situ-Sanierung mit festen Wärmequellen,* 2003, ISBN 3-933761-18-2

116 Marx, Walter: *Wasserkraft, Bewässerung, Umwelt - Planungs- und Bewertungsschwerpunkte der Wasserbewirtschaftung,* 2003, ISBN 3-933761-19-0

117 Hinkelmann, Reinhard: *Efficient Numerical Methods and Information-Processing Techniques in Environment Water,* 2003, ISBN 3-933761-20-4

118 Samaniego-Eguiguren, Luis Eduardo: *Hydrological Consequences of Land Use / Land Cover and Climatic Changes in Mesoscale Catchments*, 2003, ISBN 3-933761-21-2

119 Neunhäuserer, Lina: *Diskretisierungsansätze zur Modellierung von Strömungs- und Transportprozessen in geklüftet-porösen Medien*, 2003, ISBN 3-933761-22-0

142 Hundecha, Hirpa Yeshewatesfa: *Regionalization of Parameters of a Conceptual Rainfall-Runoff Model*, 2005, ISBN: 3-933761-45-X

143 Wege, Ralf: *Untersuchungs- und Überwachungsmethoden für die Beurteilung natürlicher Selbstreinigungsprozesse im Grundwasser,* 2005, ISBN 3-933761-46-8

144 Breiting, Thomas: *Techniken und Methoden der Hydroinformatik - Modellierung von komplexen Hydrosystemen im Untergrund*, 2006, ISBN 3-933761-47-6

145 Hrsg.: Braun, Jürgen; Koschitzky, Hans-Peter; Müller, Martin: *Ressource Untergrund: 10 Jahre VEGAS: Forschung und Technologieentwicklung zum Schutz von Grundwasser und Boden,* Tagungsband zur Veranstaltung am 28. und 29. September 2005 an der Universität Stuttgart, Campus Stuttgart-Vaihingen, 2005, ISBN 3-933761-48-4

146 Rojanschi, Vlad: *Abflusskonzentration in mesoskaligen Einzugsgebieten unter Berücksichtigung des Sickerraumes,* 2006, ISBN 3-933761-49-2

147 Winkler, Nina Simone: *Optimierung der Steuerung von Hochwasserrückhaltebeckensystemen,* 2006, ISBN 3-933761-50-6

148 Wolf, Jens: *Räumlich differenzierte Modellierung der Grundwasserströmung alluvialer Aquifere für mesoskalige Einzugsgebiete*, 2006, ISBN: 3-933761-51-4

149 Kohler, Beate: *Externe Effekte der Laufwasserkraftnutzung*, 2006, ISBN 3-933761-52-2

150 Hrsg.: Braun, Jürgen; Koschitzky, Hans-Peter; Stuhrmann, Matthias: *VEGAS-Statuskolloquium 2006,* Tagungsband zur Veranstaltung am 28. September 2006 an der Universität Stuttgart, Campus Stuttgart-Vaihingen, 2006, ISBN 3-933761-53-0

151 Niessner, Jennifer: *Multi-Scale Modeling of Multi-Phase - Multi-Component Processes in Heterogeneous Porous Media*, 2006, ISBN 3-933761-54-9

152 Fischer, Markus: *Beanspruchung eingeerdeter Rohrleitungen infolge Austrocknung bindiger Böden,* 2006, ISBN 3-933761-55-7

153 Schneck, Alexander: *Optimierung der Grundwasserbewirtschaftung unter Berücksichtigung der Belange der Wasserversorgung, der Landwirtschaft und des Naturschutzes*, 2006, ISBN 3-933761-56-5

154 Das, Tapash: *The Impact of Spatial Variability of Precipitation on the Predictive Uncertainty of Hydrological Models,* 2006, ISBN 3-33761-57-3

155 Bielinski, Andreas: *Numerical Simulation of CO_2 sequestration in geological formations*, 2007, ISBN 3-933761-58-1

156 Mödinger, Jens: *Entwicklung eines Bewertungs- und Entscheidungsunterstützungssystems für eine nachhaltige regionale Grundwasserbewirtschaftung*, 2006, ISBN 3-933761-60-3

157 Manthey, Sabine: *Two-phase flow processes with dynamic effects in porous media - parameter estimation and simulation,* 2007, ISBN 3-933761-61-1

158 Pozos Estrada, Oscar: *Investigation on the Effects of Entrained Air in Pipelines,* 2007, ISBN 3-933761-62-X

159 Ochs, Steffen Oliver: *Steam injection into saturated porous media – process analysis including experimental and numerical investigations*, 2007, ISBN 3-933761-63-8

160 Marx, Andreas: *Einsatz gekoppelter Modelle und Wetterradar zur Abschätzung von Niederschlagsintensitäten und zur Abflussvorhersage,* 2007, ISBN 3-933761-64-6

161 Hartmann, Gabriele Maria: *Investigation of Evapotranspiration Concepts in Hydrological Modelling for Climate Change Impact Assessment*, 2007, ISBN 3-933761-65-4

162 Kebede Gurmessa, Tesfaye: *Numerical Investigation on Flow and Transport Characteristics to Improve Long-Term Simulation of Reservoir Sedimentation*, 2007, ISBN 3-933761-66-2

163 Trifković, Aleksandar: *Multi-objective and Risk-based Modelling Methodology for Planning, Design and Operation of Water Supply Systems*, 2007, ISBN 3-933761-67-0

164 Götzinger, Jens: *Distributed Conceptual Hydrological Modelling - Simulation of Climate, Land Use Change Impact and Uncertainty Analysis*, 2007, ISBN 3-933761-68-9

189   Thapa, Pawan Kumar: *Physically-based spatially distributed rainfall runoff modelling for soil erosion estimation*, 2010, ISBN 978-3-933761-93-4

190   Wurms, Sven: *Numerische Modellierung der Sedimentationsprozesse in Retentionsanlagen zur Steuerung von Stoffströmen bei extremen Hochwasserabflussereignissen*, 2011, ISBN 978-3-933761-94-1

191   Merkel, Uwe: *Unsicherheitsanalyse hydraulischer Einwirkungen auf Hochwasserschutzdeiche und Steigerung der Leistungsfähigkeit durch adaptive Strömungsmodellierung*, 2011, ISBN 978-3-933761-95-8

192   Fritz, Jochen: *A Decoupled Model for Compositional Non-Isothermal Multiphase Flow in Porous Media and Multiphysics Approaches for Two-Phase Flow*, 2010,
ISBN 978-3-933761-96-5

193   Weber, Karolin (Hrsg.): *12. Treffen junger WissenschaftlerInnen an Wasserbauinstituten*, 2010, ISBN 978-3-933761-97-2

194   Bliefernicht, Jan-Geert: *Probability Forecasts of Daily Areal Precipitation for Small River Basins,* 2011, ISBN 978-3-933761-98-9

195   Hrsg.: Koschitzky, Hans-Peter; Braun, Jürgen: *VEGAS-Kolloquium 2010 In-situ-Sanierung - Stand und Entwicklung Nano und ISCO -,* Tagungsband zur Veranstaltung am 07. Oktober 2010 an der Universität Stuttgart, Campus Stuttgart-Vaihingen, 2010,
ISBN 978-3-933761-99-6

196   Gafurov, Abror: *Water Balance Modeling Using Remote Sensing Information - Focus on Central Asia,* 2010, ISBN 978-3-942036-00-9

197   Mackenberg, Sylvia: *Die Quellstärke in der Sickerwasserprognose: Möglichkeiten und Grenzen von Labor- und Freilanduntersuchungen,* 2010, ISBN 978-3-942036-01-6

198   Singh, Shailesh Kumar: *Robust Parameter Estimation in Gauged and Ungauged Basins,* 2010, ISBN 978-3-942036-02-3

199   Doğan, Mehmet Onur: *Coupling of porous media flow with pipe flow,* 2011,
ISBN 978-3-942036-03-0

200   Liu, Min: *Study of Topographic Effects on Hydrological Patterns and the Implication on Hydrological Modeling and Data Interpolation,* 2011, ISBN 978-3-942036-04-7

201   Geleta, Habtamu Itefa: *Watershed Sediment Yield Modeling for Data Scarce Areas,* 2011, ISBN 978-3-942036-05-4

202   Franke, Jörg: *Einfluss der Überwachung auf die Versagenswahrscheinlichkeit von Staustufen,* 2011, ISBN 978-3-942036-06-1

203   Bakimchandra, Oinam: *Integrated Fuzzy-GIS approach for assessing regional soil erosion risks,* 2011, ISBN 978-3-942036-07-8

204   Alam, Muhammad Mahboob: *Statistical Downscaling of Extremes of Precipitation in Mesoscale Catchments from Different RCMs and Their Effects on Local Hydrology,* 2011, ISBN 978-3-942036-08-5

205   Hrsg.: Koschitzky, Hans-Peter; Braun, Jürgen: *VEGAS-Kolloquium 2011 Flache Geothermie - Perspektiven und Risiken,* Tagungsband zur Veranstaltung am 06. Oktober 2011 an der Universität Stuttgart, Campus Stuttgart-Vaihingen, 2011, ISBN 978-3-933761-09-2

206   Haslauer, Claus: *Analysis of Real-World Spatial Dependence of Subsurface Hydraulic Properties Using Copulas with a Focus on Solute Transport Behaviour,* 2011,
ISBN 978-3-942036-10-8

207   Dung, Nguyen Viet: *Multi-objective automatic calibration of hydrodynamic models – development of the concept and an application in the Mekong Delta,* 2011,
ISBN 978-3-942036-11-5

208   Hung, Nguyen Nghia: *Sediment dynamics in the floodplain of the Mekong Delta, Vietnam,* 2011, ISBN 978-3-942036-12-2

209   Kuhlmann, Anna: *Influence of soil structure and root water uptake on flow in the unsaturated zone,* 2012, ISBN 978-3-942036-13-9

210 Tuhtan, Jeffrey Andrew: *Including the Second Law Inequality in Aquatic Ecodynamics: A Modeling Approach for Alpine Rivers Impacted by Hydropeaking,* 2012, ISBN 978-3-942036-14-6

211 Tolossa, Habtamu: *Sediment Transport Computation Using a Data-Driven Adaptive Neuro-Fuzzy Modelling Approach,* 2012, ISBN 978-3-942036-15-3

212 Tatomir, Alexandru-Bodgan: *From Discrete to Continuum Concepts of Flow in Fractured Porous Media,* 2012, ISBN 978-3-942036-16-0

213 Erbertseder, Karin: *A Multi-Scale Model for Describing Cancer-Therapeutic Transport in the Human Lung,* 2012, ISBN 978-3-942036-17-7

214 Noack, Markus: *Modelling Approach for Interstitial Sediment Dynamics and Reproduction of Gravel Spawning Fish,* 2012, ISBN 978-3-942036-18-4

215 De Boer, Cjestmir Volkert: *Transport of Nano Sized Zero Valent Iron Colloids during Injection into the Subsurface,* 2012, ISBN 978-3-942036-19-1

216 Pfaff, Thomas: *Processing and Analysis of Weather Radar Data for Use in Hydrology*, 2013, ISBN 978-3-942036-20-7

217 Lebrenz, Hans-Henning: *Addressing the Input Uncertainty for Hydrological Modeling by a New Geostatistical Method*, 2013, ISBN 978-3-942036-21-4

218 Darcis, Melanie Yvonne: *Coupling Models of Different Complexity for the Simulation of CO_2 Storage in Deep Saline Aquifers*, 2013, ISBN 978-3-942036-22-1

219 Beck, Ferdinand: *Generation of Spatially Correlated Synthetic Rainfall Time Series in High Temporal Resolution - A Data Driven Approach*, 2013, ISBN 978-3-942036-23-8

220 Guthke, Philipp: *Non-multi-Gaussian spatial structures: Process-driven natural genesis, manifestation, modeling approaches, and influences on dependent processes*, 2013, ISBN 978-3-942036-24-5

221 Walter, Lena: *Uncertainty studies and risk assessment for CO_2 storage in geological formations*, 2013, ISBN 978-3-942036-25-2

222 Wolff, Markus: *Multi-scale modeling of two-phase flow in porous media including capillary pressure effects,* 2013, ISBN 978-3-942036-26-9

223 Mosthaf, Klaus Roland: *Modeling and analysis of coupled porous-medium and free flow with application to evaporation processes,* 2014, ISBN 978-3-942036-27-6

224 Leube, Philipp Christoph: *Methods for Physically-Based Model Reduction in Time: Analysis, Comparison of Methods and Application*, 2013, ISBN 978-3-942036-28-3

225 Rodríguez Fernández, Jhan Ignacio: *High Order Interactions among environmental variables: Diagnostics and initial steps towards modeling*, 2013, ISBN 978-3-942036-29-0

226 Eder, Maria Magdalena: *Climate Sensitivity of a Large Lake*, 2013, ISBN 978-3-942036-30-6

227 Greiner, Philipp: *Alkoholinjektion zur In-situ-Sanierung von CKW Schadensherden in Grundwasserleitern: Charakterisierung der relevanten Prozesse auf unterschiedlichen Skalen*, 2014, ISBN 978-3-942036-31-3

228 Lauser, Andreas: *Theory and Numerical Applications of Compositional Multi-Phase Flow in Porous Media*, 2014, ISBN 978-3-942036-32-0

229 Enzenhöfer, Rainer: *Risk Quantification and Management in Water Production and Supply Systems*, 2014, ISBN 978-3-942036-33-7

230 Faigle, Benjamin: *Adaptive modelling of compositional multi-phase flow with capillary pressure*, 2014, ISBN 978-3-942036-34-4

231 Oladyshkin, Sergey: *Efficient modeling of environmental systems in the face of complexity and uncertainty*, 2014, ISBN 978-3-942036-35-1

232 Sugimoto, Takayuki: *Copula based Stochastic Analysis of Discharge Time Series*, 2014, ISBN 978-3-942036-36-8

233 Koch, Jonas: *Simulation, Identification and Characterization of Contaminant Source Architectures in the Subsurface*, 2014, ISBN 978-3-942036-37-5

234 Zhang, Jin: *Investigations on Urban River Regulation and Ecological Rehabilitation Measures, Case of Shenzhen in China*, 2014, ISBN 978-3-942036-38-2

235 Siebel, Rüdiger: *Experimentelle Untersuchungen zur hydrodynamischen Belastung und Standsicherheit von Deckwerken an überströmbaren Erddämmen,* 2014, ISBN 978-3-942036-39-9

236 Baber, Katherina: *Coupling free flow and flow in porous media in biological and technical applications: From a simple to a complex interface description,* 2014, ISBN 978-3-942036-40-5

237 Nuske, Klaus Philipp: *Beyond Local Equilibrium — Relaxing local equilibrium assumptions in multiphase flow in porous media,* 2014, ISBN 978-3-942036-41-2

238 Geiges, Andreas: *Efficient concepts for optimal experimental design in nonlinear environmental systems*, 2014, ISBN 978-3-942036-42-9

239 Schwenck, Nicolas: *An XFEM-Based Model for Fluid Flow in Fractured Porous Media*, 2014, ISBN 978-3-942036-43-6

240 Chamorro Chávez, Alejandro: *Stochastic and hydrological modelling for climate change prediction in the Lima region, Peru*, 2015, ISBN 978-3-942036-44-3

241 Yulizar: *Investigation of Changes in Hydro-Meteorological Time Series Using a Depth-Based Approach*, 2015, ISBN 978-3-942036-45-0

242 Kretschmer, Nicole: *Impacts of the existing water allocation scheme on the Limarí watershed – Chile, an integrative approach*, 2015, ISBN 978-3-942036-46-7

243 Kramer, Matthias: *Luftbedarf von Freistrahlturbinen im Gegendruckbetrieb*, 2015, ISBN 978-3-942036-47-4

244 Hommel, Johannes: *Modeling biogeochemical and mass transport processes in the subsurface: Investigation of microbially induced calcite precipitation*, 2016, ISBN 978-3-942036-48-1

245 Germer, Kai: *Wasserinfiltration in die ungesättigte Zone eines makroporösen Hanges und deren Einfluss auf die Hangstabilität*, 2016, ISBN 978-3-942036-49-8

246 Hörning, Sebastian: *Process-oriented modeling of spatial random fields using copulas*, 2016, ISBN 978-3-942036-50-4

247 Jambhekar, Vishal: *Numerical modeling and analysis of evaporative salinization in a coupled free-flow porous-media system,* 2016, ISBN 978-3-942036-51-1

248 Huang, Yingchun: *Study on the spatial and temporal transferability of conceptual hydrological models*, 2016, ISBN 978-3-942036-52-8

249 Kleinknecht, Simon Matthias: *Migration and retention of a heavy NAPL vapor and remediation of the unsaturated zone*, 2016, ISBN 978-3-942036-53-5

250 Kwakye, Stephen Oppong: *Study on the effects of climate change on the hydrology of the West African sub-region*, 2016, ISBN 978-3-942036-54-2

251 Kissinger, Alexander: *Basin-Scale Site Screening and Investigation of Possible Impacts of CO_2 Storage on Subsurface Hydrosystems*, 2016, ISBN 978-3-942036-55-9

252 Müller, Thomas: *Generation of a Realistic Temporal Structure of Synthetic Precipitation Time Series for Sewer Applications*, 2017, ISBN 978-3-942036-56-6

253 Grüninger, Christoph: *Numerical Coupling of Navier-Stokes and Darcy Flow for Soil-Water Evaporation*, 2017, ISBN 978-3-942036-57-3

254 Suroso: *Asymmetric Dependence Based Spatial Copula Models: Empirical Investigations and Consequences on Precipitation Fields*, 2017, ISBN 978-3-942036-58-0

255 Müller, Thomas; Mosthaf, Tobias; Gunzenhauser, Sarah; Seidel, Jochen; Bárdossy, András: *Grundlagenbericht Niederschlags-Simulator (NiedSim3)*, 2017, ISBN 978-3-942036-59-7

256 Mosthaf, Tobias: *New Concepts for Regionalizing Temporal Distributions of Precipitation and for its Application in Spatial Rainfall Simulation*, 2017, ISBN 978-3-942036-60-3

257 Fenrich, Eva Katrin: *Entwicklung eines ökologisch-ökonomischen Vernetzungsmodells für Wasserkraftanlagen und Mehrzweckspeicher,* 2018, ISBN 978-3-942036-61-0

258 Schmidt, Holger: *Microbial stabilization of lotic fine sediments,* 2018, ISBN 978-3-942036-62-7

259 Fetzer, Thomas: *Coupled Free and Porous-Medium Flow Processes Affected by Turbulence and Roughness–Models, Concepts and Analysis,* 2018, ISBN 978-3-942036-63-4

260 Schröder, Hans Christoph: *Large-scale High Head Pico Hydropower Potential Assessment,* 2018, ISBN 978-3-942036-64-1

261 Bode, Felix: *Early-Warning Monitoring Systems for Improved Drinking Water Resource Protection,* 2018, ISBN 978-3-942036-65-8

262 Gebler, Tobias: *Statistische Auswertung von simulierten Talsperrenüberwachungsdaten zur Identifikation von Schadensprozessen an Gewichtsstaumauern,* 2018, ISBN 978-3-942036-66-5

263 Harten, Matthias von: *Analyse des Zuppinger-Wasserrades – Hydraulische Optimierungen unter Berücksichtigung ökologischer Aspekte,* 2018, ISBN 978-3-942036-67-2

264 Yan, Jieru: *Nonlinear estimation of short time precipitation using weather radar and surface observations,* 2018, ISBN 978-3-942036-68-9

265 Beck, Martin: *Conceptual approaches for the analysis of coupled hydraulic and geomechanical processes,* 2019, ISBN 978-3-942036-69-6

266 Haas, Jannik: *Optimal planning of hydropower and energy storage technologies for fully renewable power systems,* 2019, ISBN 978-3-942036-70-2

267 Schneider, Martin: *Nonlinear Finite Volume Schemes for Complex Flow Processes and Challenging Grids,* 2019, ISBN 978-3-942036-71-9

268 Most, Sebastian Christopher: *Analysis and Simulation of Anomalous Transport in Porous Media,* 2019, ISBN 978-3-942036-72-6

269 Buchta, Rocco: *Entwicklung eines Ziel- und Bewertungssystems zur Schaffung nachhaltiger naturnaher Strukturen in großen sandgeprägten Flüssen des norddeutschen Tieflandes,* 2019, ISBN 978-3-942036-73-3

270 Thom, Moritz: *Towards a Better Understanding of the Biostabilization Mechanisms of Sediment Beds,* 2019, ISBN 978-3-942036-74-0

271 Stolz, Daniel: *Die Nullspannungstemperatur in Gewichtsstaumauern unter Berücksichtigung der Festigkeitsentwicklung des Betons,* 2019, ISBN 978-3-942036-75-7

272 Rodriguez Pretelin, Abelardo: *Integrating transient flow conditions into groundwater well protection,* 2020, ISBN: 978-3-942036-76-4

273 Weishaupt, Kilian: *Model Concepts for Coupling Free Flow with Porous Medium Flow at the Pore-Network Scale: From Single-Phase Flow to Compositional Non-Isothermal Two-Phase Flow,* 2020, ISBN: 978-3-942036-77-1

274 Koch, Timo: *Mixed-dimension models for flow and transport processes in porous media with embedded tubular network systems,* 2020, ISBN: 978-3-942036-78-8

275 Gläser, Dennis: *Discrete fracture modeling of multi-phase flow and deformation in fractured poroelastic media,* 2020, ISBN: 978-3-942036-79-5

276 Seitz, Lydia: *Development of new methods to apply a multi-parameter approach – A first step towards the determination of colmation,* 2020, ISBN: 978-3-942036-80-1

277 Ebrahim Bakhshipour, Amin: *Optimizing hybrid decentralized systems for sustainable urban drainage infrastructures planning,* 2021, ISBN: 978-3-942036-81-8

278 Seitz, Gabriele: *Modeling Fixed-Bed Reactors for Thermochemical Heat Storage with the Reaction System $CaO/Ca(OH)_2$,* 2021, ISBN: 978-3-942036-82-5

279 Emmert, Simon: *Developing and Calibrating a Numerical Model for Microbially Enhanced Coal-Bed Methane Production,* 2021, ISBN: 978-3-942036-83-2

280 Heck, Katharina Klara: Modelling and analysis of multicomponent transport at the interface between free- and porous-medium flow - influenced by radiation and roughness, 2021, ISBN: 978-3-942036-84-9

281 Ackermann, Sina: *A multi-scale approach for drop/porous-medium interaction*, 2021, ISBN: 978-3-942036-85-6

282 Beckers, Felix: *Investigations on Functional Relationships between Cohesive Sediment Erosion and Sediment Characteristics*, 2021, ISBN: 978-3-942036-86-3

283 Schlabing, Dirk: *Generating Weather for Climate Impact Assessment on Lakes*, 2021, ISBN: 978-3-942036-87-0

284 Becker, Beatrix: *Efficient multiscale multiphysics models accounting for reversible flow at various subsurface energy storage sites*, 2021, ISBN: 978-3-942036-88-7

285 Reuschen, Sebastian: *Bayesian Inversion and Model Selection of Heterogeneities in Geo-statistical Subsurface Modeling*, 2021, ISBN: 978-3-942036-89-4

286 Michalkowski, Cynthia: *Modeling water transport at the interface between porous GDL and gas distributor of a PEM fuel cell cathode*, 2022, ISBN: 978-3-942036-90-0

287 Koca, Kaan: *Advanced experimental methods for investigating flow-biofilm-sediment interactions*, 2022, ISBN: 978-3-942036-91-7

288 Modiri, Ehsan: *Clustering simultaneous occurrences of extreme floods in the Neckar catchment*, 2022, ISBN: 978-3-942036-92-4

289 Mayar, Mohammad Assem: *High-resolution spatio-temporal measurements of the colmation phenomenon under laboratory conditions*, 2022, ISBN: 978-3-942036-93-1

290 Schäfer Rodrigues Silva, Aline: *Quantifying and Visualizing Model Similarities for Multi-Model Methods*, 2022, ISBN: 978-3-942036-94-8

291 Moreno Leiva, Simón: *Optimal planning of water and renewable energy systems for copper production processes with sector coupling and demand flexibility*, 2022, ISBN 978-3-942036-95-5

292 Schönau, Steffen: *Modellierung von Bodenerosion und Sedimentaustrag bei Hochwasserereignissen am Beispiel des Einzugsgebiets der Rems*, 2022, ISBN 978-3-942036-96-2

293 Glatz, Kumiko: *Upscaling of Nanoparticle Transport in Porous Media,* 2022, ISBN 978-3-942036-97-9

294 Pavía Santolamazza, Daniela: *Event-based flood estimation using a random forest algorithm for the regionalization in small catchments*, 2022, ISBN 978-3-942036-98-6

295 Haun, Stefan: *Advanced Methods for a Sustainable Sediment Management of Reservoirs*, 2022, ISBN 978-3-942036-99-3

296 Herma, Felix: *Data Processing and Model Choice for Flood Prediction*, 2022, ISBN 978-3-910293-00-7

297 Weinhardt, Felix: *Porosity and permeability alterations in processes of biomineralization in porous media - microfluidic investigations and their interpretation*, 2022, ISBN 978-3-910293-01-4

298 Sadid, Najibullah: *Bedload Transport Estimation in Mountainous Intermittent Rivers and Streams*, 2023, ISBN 978-3-910293-02-1

299 Mohammadi, Farid: *A Surrogate-Assisted Bayesian Framework for Uncertainty-Aware Validation Benchmarks*, 2023, ISBN 978-3-910293-03-8

300 Praditia, Timothy: *Physics-informed Neural Networks for Learning Dynamic, Distributed and Uncertain Systems*, 2023, ISBN 978-3-910293-04-5

301 Gyawali, Dhiraj Raj: *Development and parameter estimation of conceptual snow-melt models using MODIS snow-cover distribution*, 2023, ISBN 978-3-910293-05-2

302 Görtz, Jan: *Coupled modeling approach for physico-chemical processes during the deterioration of cement-based structures*, 2023, ISBN 978-3-910293-06-9

303 Veyskarami, Maziar: *Coupled free-flow–porous media flow processes including drop formation*, 2023, ISBN 978-3-910293-07-6

304 El Hachem, Abbas: *Spatial Extent of Precipitation Extremes in Hydrology*, 2023, ISBN 978-3-910293-08-3

305   Banerjee, Ishani: *Stochastic Model Comparison and Refinement Strategies for Gas Migration in the Subsurface*, 2023, ISBN 978-3-910293-09-0

Die Mitteilungshefte ab der Nr. 134 (Jg. 2005) stehen als pdf-Datei über die Homepage des Instituts: www.iws.uni-stuttgart.de zur Verfügung.